Mathematical Modeling of AA Amyloidosis: Coupling SAA-HDL Binding Dynamics with Path-Dependent Renal Aging

Andrey V. Kuznetsov

Department of Mechanical and Aerospace Engineering, North Carolina State University,

Raleigh, NC 27695-7910, USA; e-mail: avkuznet@ncsu.edu

Abstract

AA amyloidosis is a severe complication of chronic inflammatory diseases characterized by fibrillar protein deposition in the kidneys, leading to progressive organ failure. This study presents a mathematical model coupling SAA-HDL binding dynamics with renal amyloid aggregation kinetics to elucidate disease pathogenesis. Under normal conditions, Serum Amyloid A (SAA) circulates bound to high-density lipoprotein (HDL), which acts as a molecular chaperone preventing misfolding. However, during chronic inflammation, SAA production exceeds HDL binding capacity, resulting in free SAA that undergoes renal filtration. The model calculates free SAA concentration from reversible binding equilibrium and incorporates renal filtration, mesangial accumulation, and conversion to amyloid fibrils through primary nucleation and autocatalytic growth mechanisms. A central contribution of this work is quantifying accumulated nephrotoxicity arising from AA oligomers, which inflict cumulative cytotoxic damage to mesangial and tubular cells over time. Because oligomers are continuously generated during ongoing aggregation, their toxic burden integrates across the entire duration of the disease. Combined nephrotoxicity, encompassing both oligomer-mediated cellular injury and fibril-driven mechanical disruption of renal architecture, therefore reflects not merely the current disease state but the full inflammatory trajectory of the patient. This cumulative damage defines renal biological age, a measure of functional deterioration whose portion attributable to accumulated nephrotoxicity is irreversible. Renal biological age is also path-dependent: two patients with identical present-day SAA levels may carry different renal damage burdens depending on the duration, timing, and severity of their prior inflammatory episodes. Sensitivity analysis reveals that HDL concentration and SAA cleavage rate are critical determinants of amyloid burden.

Keywords: biomarkers of nephrotoxic injury; biomarker of aging; chronic inflammation; oligomer cytotoxicity; Finke−Watzky model

Abbreviations

HDL high-density lipoprotein

F-W Finke-Watzky

SAA Serum Amyloid A

1. Introduction

Systemic Amyloid A (AA) amyloidosis is a severe, often fatal complication of chronic inflammatory conditions including rheumatoid arthritis, familial Mediterranean fever, and chronic infections [1]. The disease involves extracellular deposition of insoluble fibrillar aggregates in major organs, predominantly the kidneys, where accumulation leads to progressive organ failure [2,3]. Despite chronic inflammation affecting many patients, clinically significant AA amyloidosis develops in only a minority of patients [4]. Although the clinical course of renal amyloidosis is well-characterized, the molecular thresholds triggering the transition from controlled inflammation to uncontrolled amyloid deposition remain unclear.

The amyloid deposits originate from Serum Amyloid A (SAA), an acute-phase apolipoprotein synthesized by the liver. Under normal physiological conditions and mild inflammation, SAA circulates bound to high-density lipoprotein (HDL) particles with high affinity [5-7]. Structural studies reveal that HDL binding protects SAA from misfolding by sequestering the amyloidogenic N-terminal region against the lipoprotein surface [5]. Thus, HDL serves as a molecular chaperone, maintaining SAA in a soluble, non-aggregating state.

This protective mechanism, however, has finite capacity. Biophysical studies show that SAA binds to HDL through a rigid hydrophobic interface, creating a saturable interaction with strict stoichiometric limits on SAA occupancy per HDL particle [5]. When severe or prolonged inflammation drives SAA production beyond the HDL binding capacity, saturation occurs, and excess SAA remains free in plasma without lipid protection [6]. These lipid-poor SAA species are no longer protected from misfolding.

While the large HDL-SAA complex cannot pass through the glomerular filtration barrier and remains in the bloodstream, free SAA (~12 kDa) is small enough for renal filtration [8]. Once in the renal mesangium and proximal tubules, unbound SAA becomes locally concentrated and undergoes proteolytic cleavage, creating conditions that thermodynamically favor AA protein aggregation [8,9].

Despite these mechanistic insights, predicting amyloidosis development in individual patients remains difficult. Serum SAA levels correlate poorly with amyloid burden; many patients with chronically elevated SAA never develop disease, while others progress rapidly. This suggests a critical threshold at which the capacity of the protective HDL reservoir is exceeded and autocatalytic fibril growth becomes self-sustaining [10].

Building upon previously developed models of transthyretin and AL amyloidosis [11,12], this work develops a novel mathematical model that couples SAA-HDL binding dynamics with amyloid aggregation kinetics. The model calculates the concentration of free, filterable SAA from HDL binding

capacity and dissociation constant (K_d) determined from assuming reversible binding equilibrium between free SAA monomers (S_{free}) and available binding sites on HDL particles [13]. The computed free SAA concentration serves as a parameter in a system of differential equations governing renal filtration, mesangial accumulation, and conversion to fibrillar aggregates through primary nucleation, autocatalytic conversion, and oligomer deposition into fibrils [14]. The model quantifies how HDL saturation triggers pathological amyloid accumulation, providing a framework for therapeutic target identification.

2. Materials and models

2.1. Governing equations

2.1.1. Equations characterizing SAA–HDL association

In the model, the interaction between SAA and HDL is treated as a saturable binding event. While HDL particles can accommodate several SAA monomers under acute inflammatory conditions [5,15], the present model assumes that during chronic inflammation each HDL particle binds a single SAA molecule. A reversible binding equilibrium is assumed between free SAA monomers (S_{free}) and available binding sites on HDL particles (H_{free}):

$$S_{free} + H_{free} \underset{k_{off}}{\overset{k_{on}}{\rightleftharpoons}} SH \tag{1}$$

where *SH* represents the SAA-HDL complex.

The equilibrium dissociation constant for SH is determined as:

$$K_d = \frac{[S]_{free}[H]_{free}}{[SH]} \tag{2}$$

The total SAA concentration (HDL-bound plus free) is then given by:

$$[S]_{tot} = [S]_{free} + [SH] \tag{3}$$

and the total concentration of binding sites for SAA on HDL particles, comprising both occupied and available sites, is calculated as:

$$[H]_{tot} = [H]_{free} + [SH] \tag{4}$$

Substituting Eq. (4) into Eq. (2) yields the following expression for the equilibrium dissociation constant:

$$K_d = \frac{[S]_{free}\left([H]_{tot} - [SH]\right)}{[SH]} \tag{5}$$

Solving Eq. (5) for the concentration of the SAA-HDL complex yields:

$$[SH] = \frac{[S]_{free}[H]_{tot}}{K_d + [S]_{free}} \tag{6}$$

Substituting the expression for $[SH]$ from Eq. (3) into Eq. (6) results in:

$$[S]_{tot} - [S]_{free} = \frac{[S]_{free}[H]_{tot}}{K_d + [S]_{free}} \tag{7}$$

Solving for $[S]_{free}$ yields a quadratic equation:

$$[S]_{free}^2 + [S]_{free}\left(K_d + [H]_{tot} - [S]_{tot}\right) - K_d[S]_{tot} = 0 \tag{8}$$

Since concentration must be positive, the positive root is selected:

$$[S]_{free} = \frac{-\left(K_d + [H]_{tot} - [S]_{tot}\right) + \sqrt{\left(K_d + [H]_{tot} - [S]_{tot}\right)^2 + 4K_d[S]_{tot}}}{2} \tag{9}$$

The fraction of free SAA can then be calculated as:

$$\omega_S = \frac{[S]_{free}}{[S]_{tot}} \tag{10}$$

Similarly, the fraction of unbound HDL can be calculated as:

$$\omega_H = \frac{[H]_{free}}{[H]_{tot}} \tag{11}$$

where

$$[H]_{free} = [H]_{tot} - [S]_{tot} + [S]_{free} \tag{12}$$

Substituting $[S]_{free}$ from Eq. (10) and $[SH]$ from Eq. (3) into Eq. (5) yields the following expression for the equilibrium dissociation constant:

$$K_d = \frac{\omega_S \left([H]_{tot} - [S]_{tot} + \omega_S [S]_{tot} \right)}{1 - \omega_S} \tag{13}$$

2.1.2. Development of conservation equations describing SAA deposition in the kidneys and AA amyloid fibril formation

The SAA-HDL complex is too large to pass into the renal mesangium and is retained in the blood. Free SAA monomers, however, are readily filtered by the kidney where they are internalized by mesangial and proximal tubular cells [16]. Within the acidic environment of the lysosome (pH 3.5–4.5), these unbound monomers evade complete degradation and instead form cytotoxic oligomers [17]. Subsequent proteolytic cleavage sheds the C-terminus, generating the highly amyloidogenic AA fragment [8], which nucleates in the supersaturated renal interstitium to form the insoluble fibrils characteristic of the disease.

Upon renal uptake, internalized SAA is processed in endo-lysosomal compartments by cathepsins. Cathepsin B, acting primarily as a carboxypeptidase, trims the SAA C-terminus to generate N-terminal AA-like fragments, while cathepsin D and other lysosomal proteases promote more complete degradation. Limited C-terminal proteolysis destabilizes the SAA structure, exposes the amyloidogenic N-terminal region, and promotes formation of AA-type aggregates that accumulate in tissues [18]. This cleavage process is simulated by the following equation:

$$S_{kidney} \xrightarrow{k_{cl}} A \tag{14}$$

The mathematical model comprises conservation equations for SAA monomers entering the kidneys from blood plasma, AA monomers derived from the lysosomal cleavage of SAA precursors, free AA oligomers, and AA oligomers deposited into fibrils (Fig. 1). A lumped capacitance formulation is employed, assuming spatial homogeneity of all AA species within the kidneys (a simplifying assumption that neglects regional variations in renal AA processing). Time serves as the sole independent variable and corresponds to calendar age. Dependent variables are defined in Table 1, and model parameters are summarized in Table 2.

Formulating the conservation of SAA monomers entering the kidneys from the blood plasma, and normalizing by $V_{kidneys}$, yields the following equation:

$$\frac{d[S]_{kidney}}{dt} = h_S \frac{A_{kidneys}}{V_{kidneys}}\left([S]_{free} - [S]_{kidney}\right) - k_{cl}[S]_{kidney} - [S]_{kidney}\frac{\ln(2)}{T_{1/2,S}} \tag{15}$$

In Eq. (15), the first term on the right-hand side represents the retention rate of filtered SAA monomers, where $h_S A_{kidneys}\left([S]_{free} - [S]_{kidney}\right)$ denotes the total rate of renal deposition of monomers. The second term represents the loss of SAA monomers deposited in the kidneys through their cleavage into N-terminal AA fragments susceptible to aggregation (see Eq. (14)). The third term accounts for the clearance of SAA monomers by proteolytic enzymes within the lysosomes of proximal tubular cells [19].

The numerical solution demonstrates that $[S]_{kidney}$ rapidly attains a constant steady-state value that is maintained for most of the disease course (Fig. S1), validating the use of the steady-state approximation. Applying steady-state conditions to Eq. (15) yields:

$$[S]_{kidney,ss} = \frac{A_{kidneys} h_S [S]_{free} T_{1/2,S}}{A_{kidneys} h_S T_{1/2,S} + k_{cl} T_{1/2,S} V_{kidneys} + V_{kidneys}\ln(2)} \tag{16}$$

The cleavage of SAA (see Eq. (14)) releases the N-terminal AA fragment (AA protein), which rapidly self-associates into oligomers and eventually forms insoluble amyloid fibrils. Soluble prefibrillar AA oligomers act as pathogenic intermediates that bridge elevated SAA levels to tissue AA fibril deposition [17]. To simulate the oligomerization of the AA protein, the Finke–Watzky (F–W) model was employed. This minimal two-step model, which captures both nucleation and autocatalytic growth, has been extensively utilized to characterize aggregation dynamics in various amyloidogenic proteins [20-22]. Within this framework, the first pseudo-elementary step corresponds to the primary nucleation of AA oligomers. The second step represents secondary autocatalytic conversion, where pre-existing oligomers act as templates to accelerate the recruitment and conversion of free AA monomers [23].

The first pseudo-elementary step describes primary nucleation of AA protein oligomers:

$$A \xrightarrow{k_1} B \tag{17}$$

In the F-W model, oligomers are treated as activated monomers capable of catalyzing further aggregation. The model does not distinguish between the physical properties (size or mass) of monomers and oligomers. The second pseudo-elementary step represents the autocatalytic conversion of monomeric AA protein into oligomeric forms:

$$A + B \xrightarrow{k_2} 2B \tag{18}$$

$$\frac{d[A]}{dt} = k_{cl}[S]_{kidney} - k_1[A] - k_2[A][B] - [A]\frac{\ln(2)}{T_{1/2,A}} \tag{19}$$

In Eq. (19), the first term on the right-hand side represents the generation of AA fragments (monomers) via the cleavage of SAA (as defined in Eq. (14)). The second and third terms account for the depletion of AA monomers due to their conversion into oligomers through nucleation and autocatalytic processes, respectively. Finally, the fourth term describes the degradation of AA monomers by proteases.

The formation of AA fibrils in the kidneys from oligomers is modeled analogously to colloidal suspension coagulation [24]. In this model, free misfolded AA oligomers (*B*) have a half-deposition time $\theta_{1/2,B}$, representing the time required for half of the free oligomers to be incorporated into AA fibrils. Applying the principle of conservation of the number of free AA oligomers within the kidneys, and normalizing the resulting equation by $V_{kidneys}$, yields:

$$\frac{d[B]}{dt} = k_1[A] + k_2[A][B] - [B]\frac{\ln(2)}{T_{1/2,B}} - [B]\frac{\ln(2)}{\theta_{1/2,B}} \tag{20}$$

The first two terms on the right-hand side of Eq. (20) represent the generation of free AA oligomers from AA monomers through nucleation and autocatalytic processes, respectively. These terms are analogous to the second and third terms in Eq. (19) but with opposite signs. The third term accounts for the clearance of oligomers due to their finite half-life. The fourth term represents the loss of free oligomers through their incorporation into fibrils.

As with $[S]_{kidney}$, the concentrations of AA monomers and free oligomers ($[A]$ and $[B]$) rapidly attain steady-state values that are maintained for most of the disease course (Figs. S2 and S3). This justifies applying the steady-state approximation, under which Eqs. (19) and (20) become:

$$k_{cl}[S]_{kidney} - k_1[A] - k_2[A][B] - [A]\frac{\ln(2)}{T_{1/2,A}} = 0 \tag{21}$$

$$k_1[A] + k_2[A][B] - [B]\frac{\ln(2)}{T_{1/2,B}} - [B]\frac{\ln(2)}{\theta_{1/2,B}} = 0 \tag{22}$$

The summation of Eqs. (21) and (22) yields:

$$k_{cl}[S]_{kidney} - [A]\frac{\ln(2)}{T_{1/2,A}} - [B]\frac{\ln(2)}{T_{1/2,B}} - [B]\frac{\ln(2)}{\theta_{1/2,B}} = 0 \tag{23}$$

Solving Eq. (23) for $[A]$ yields:

$$[A]_{ss} = T_{1/2,A}\left(-\frac{[B](T_{1/2,B}+\theta_{1/2,B})}{T_{1/2,B}\theta_{1/2,B}} + \frac{k_{cl}[S]_{kidney}}{\ln(2)}\right) \tag{24}$$

Substituting Eq. (24) into Eq. (22) and solving for $[B]$, while selecting the positive root of the quadratic equation, yields:

$$[B]_{ss} = \frac{1}{k_2 T_{1/2,A}\ln(4)(T_{1/2,B}+\theta_{1/2,B})}\Bigg(T_{1/2,B}\theta_{1/2,B}$$

$$\times\Bigg[\frac{k_2 k_{cl} S_{kidney} T_{1/2,A}\ln(4)(T_{1/2,B}+\theta_{1/2,B})(k_1 T_{1/2,A}-\ln(2))}{T_{1/2,B}\theta_{1/2,B}} + \frac{\ln^2(2)(T_{1/2,B}+\theta_{1/2,B})^2(k_1 T_{1/2,A}+\ln(2))^2}{T_{1/2,B}^2\theta_{1/2,B}^2}$$

$$+k_2^2 k_{cl}^2 S_{kidney}^2 T_{1/2,A}^2\Bigg]^{1/2} - k_1 T_{1/2,A}\ln(2)(T_{1/2,B}+\theta_{1/2,B}) + k_2 k_{cl} S_{kidney} T_{1/2,A} T_{1/2,B}\theta_{1/2,B} - \ln^2(2)(T_{1/2,B}+\theta_{1/2,B})\Bigg) \tag{25}$$

Applying the conservation principle to AA oligomers sequestered into fibrillar structures within the kidneys and normalizing by $V_{kidneys}$ yields the following governing equation:

$$\frac{d[I]}{dt} = [B]\frac{\ln(2)}{\theta_{1/2,B}} - [I]\frac{\ln(2)}{T_{1/2,I}} \tag{26}$$

where $[I]$ is the concentration of deposited oligomers.

In Eq. (26), the first term on the right-hand side corresponds to the fourth term in Eq. (20) with opposite sign, representing deposition into fibrils. The second term accounts for the clearance of deposited AA oligomers from fibrils based on their half-life.

Since $[B](t)$ rapidly attains its steady-state value $[B]_{ss}$, as confirmed by the numerical solution in Fig. S3, solving Eq. (26) subject to boundary condition (30d) yields:

$$[I] = \frac{\left(1-\exp\left(-\frac{t\ln(2)}{T_{1/2,I}}\right)\right)[B]_{ss}T_{1/2,I}}{\theta_{1/2,B}} \tag{27}$$

Eq. (27) shows that as time approaches infinity, the fibril concentration approaches a steady-state value:

$$[I]_{ss} = \frac{[B]_{ss} T_{1/2,I}}{\theta_{1/2,B}} \tag{28}$$

The steady-state fibril burden given by Eq. (28) is determined by the balance between two competing processes: degradation of AA amyloid fibrils in the kidneys and their continuous formation. It should be noted that AA amyloid fibrils are highly stable structures with long half-lives; a substantial reduction in fibril burden would require the future development of therapies capable of actively clearing these deposits. The time required for the fibril concentration to reach 90% of its steady-state value can be derived from Eq. (27) as:

$$t_{ss} = -T_{1/2,I} \frac{\ln(0.1)}{\ln(2)} = 3.32 T_{1/2,I} \tag{29}$$

In the limit of $T_{1/2,I} \to \infty$, Eq. (26) reduces to:

$$\frac{d[I]}{dt} = [B] \frac{\ln(2)}{\theta_{1/2,B}} \tag{30}$$

Under the assumption that the steady-state value $[B]_{ss}$ is achieved rapidly, application of boundary condition (32d) to Eq. (30) gives:

$$[I] = [B]_{ss} \frac{\ln(2)}{\theta_{1/2,B}} t \tag{31}$$

Eq. (31) reflects unbounded growth of $[I]$, consistent with the assumption that fibril degradation is negligible.

Eqs. (15), (19), (20), and (26) are solved subject to the following initial conditions:

At $t = 0$: $\quad [S]_{kindey} = 0, \quad [A] = 0, \quad [B] = 0, \quad [I] = 0$ (32a,b,c,d)

The simulation spans a period of years, which is consistent with the clinical timescale of renal AA fibril deposition [25]. Because the system's long-term behavior is independent of transient starting conditions over this duration, all AA species in Eq. (32) are initialized at zero.

The numerical solution methodology is documented in Section S1 of the Supplemental Materials.

Table 1. Model dependent variables.

Symbol	Definition	Unit
$[A]$	Molar concentration of AA fragments (monomers) in kidneys	μM
$[B]$	Molar concentration of free (not deposited in fibrils) AA oligomers in kidneys	μM
$[I]$	Molar concentration of AA oligomers deposited into AA amyloid fibrils in kidneys	μM
$[S]_{free}$	Molar concentration of free (unbound) SAA in blood plasma	μM
$[S]_{kidney}$	Molar concentration of SAA in kidneys	μM
$[H]_{free}$	Molar concentration of free (available) binding sites on HDL	μM
$[SH]$	Molar concentration of bound SAA (SAA-HDL complex)	μM

Table 2. Model parameters and their estimated values.

Symbol	Definition	Unit	Value or range	Reference or estimation method	Value(s) used in computations
a_{21}	Factor that converts from $\frac{\text{mol}}{\mu\text{m}^3}$ to μM	$\frac{\mu\text{M}\ \mu\text{m}^3}{\text{mol}}$	10^{21}		10^{21}
$A_{kidneys}$	Total surface area of the capillaries within the glomeruli in both kidneys	m^2	0.6	[26]	0.6 [a]

c	Coefficient in Eq. (49)	μM^{-1}			0.334
h_S	Mass transfer coefficient describing the rate at which free SAA in blood plasma deposits in kidneys	m s^{-1}			5.55×10^{-7} [b]
$[H]_{tot}$	Molar concentration of the number of all binding sites (occupied and available) for SAA on HDL particles	μM	30	[27]	30
k_1	Rate constant describing the first pseudoelementary (nucleation) step in the F-W model of AA oligomer formation	s^{-1}			10^{-8}, 10^{-6}, 10^{-4} [c]
k_2	Rate constant describing the second pseudoelementary (autocatalytic growth) step in the F-W model of AA oligomer formation	μM^{-1} s^{-1}			10^{-8}, 10^{-6}, 10^{-4} [d]
k_{cl}	Rate of cleavage of SAA monomers resulting in production of AA monomers	s^{-1}	9.65×10^{-5} [e]		9.65×10^{-5}

K_d	Equilibrium dissociation constant characterizing the affinity of SAA to HDL	μM	3.7 - 18 [f]	[28]	1.1789
MW_{AA}	Molecular weight of N-terminal SAA fragments (termed AA)	g mol^{-1}	1.14×10^4 - 1.25×10^4 [g]	[29]	1.20×10^4
N_A	Avogadro's number	mol^{-1}	6.022×10^{23}		6.022×10^{23}
$[S]_{tot}$	Molar concentration of total (HDL-bound and free) SAA under chronic inflammation	μM	2.5-8.3 [h]	[30]	8
$t_{AA,onset}$	Median age at diagnosis of AA amyloidosis	s	1.58×10^9 [i]	[31]	1.58×10^9
$t_{AA,f}$	Average survival time after diagnosis among patients with AA amyloidosis without treatment of underlying inflammatory disease	s	1.26×10^8 2.52×10^8 [j]	[9,25]	1.89×10^8
$T_{1/2,A}$	Half-life of AA monomers in kidneys	s		[32]	3.6×10^3, 10^{14} (to simulate the case of $T_{1/2,A}\to\infty$) [k]

$T_{1/2,B}$	Half-life of AA oligomers in kidneys	s		[17]	1.73×10^{5}, 10^{14} (to simulate the case of $T_{1/2,B}\to\infty$) [l]
$T_{1/2,I}$	Half-life of AA amyloid fibrils in kidneys	s		[9]	3.16×10^{7}, 10^{14} (to simulate the case of $T_{1/2,I}\to\infty$) [m]
$T_{1/2,S}$	Half-life of free SAA monomers deposited in kidneys	s		[32]	3.6×10^{3}, 10^{14} (to simulate the case of $T_{1/2,S}\to\infty$) [n]
$V_{kidneys}$	Total volume of two kidneys	m^3	4.04×10^{-4} [o]	[33]	4.04×10^{-4}
$\theta_{1/2,B}$	Half-deposition time of free (not yet deposited) AA oligomers into AA fibrils	s		[34]	8.64×10^{4} [p]
$\Xi_{comb,crit}$	Lethal threshold of combined renal damage	μM s			8×10^{11}
$\rho_{fibrils}$	Density of AA amyloid fibrils	$g/\mu m^3$	1.35×10^{-12} [q]	[35]	1.35×10^{-12}
ϖ	Weighting factor in Eq. (47)	μM s			1.40×10^{10}
ω_S	Fraction of lipid-free SAA under chronic inflammatory conditions		0.05-0.1	[6,30]	0.05

[a] 6,000 cm² = 0.6 m².

[b] The rate at which free SAA moves from the glomerular capillary blood into the renal tissue (mesangium) can be estimated as:

$$j = h_S \left([S]_{free} - [S]_{kindey} \right) \tag{33}$$

Also, in the kidney, flux is defined by the Glomerular Filtration Rate (*GFR*) and the sieving coefficient, $\hat{S}$:

$$j = \frac{GFR \times \hat{S} \times [S]_{free}}{A_{kidneys}} \tag{34}$$

By equating the two flux definitions and assuming that $[S]_{free} \gg [S]_{kindey}$, the mass transfer coefficient is estimated as:

$$h_S \approx \frac{GFR \times \hat{S}}{A_{kidneys}} \tag{35}$$

GFR can be estimated to be 2.08×10^{-6} m³/s (125 mL/min) for an average-sized man [36]. The sieving coefficient of SAA can be estimated as follows. SAA (12 kDa) is larger than inulin ($\hat{S} = 1$) but much smaller than albumin ($\hat{S} < 0.01$). It is similar to β_2-microglobulin ($\hat{S} \approx 0.7$), but its hydrophobic nature and tendency to oligomerize might lower its effective sieving. $\hat{S}$ for SSA is assumed to be 0.16. Since $A_{kidneys} \approx 0.6$ m², the value of h_S is estimated as:

$$h_S \approx \frac{\left(2.08 \times 10^{-6}\ \mathrm{m^3/s}\right)\left(0.16\right)}{0.6\,\mathrm{m^2}} = 5.55 \times 10^{-7}\ \mathrm{m/s} \tag{36}$$

[c] In the absence of published kinetic parameters specific for AA protein aggregation within the F-W model framework, three representative values for the nucleation rate constant, k_1: 10^{-8}, 10^{-6}, 10^{-4} s⁻¹, were selected. These values were guided by the range of nucleation rates reported for various protein systems in ref. [20], as summarized in Table S1 of ref. [37].

[d] In the absence of published kinetic parameters specific for AA protein aggregation within the F-W model framework, three representative values for the kinetic constant describing autocatalytic growth, k_2:

10^{-8}, 10^{-6}, 10^{-4} μM^{-1} s^{-1}, were selected. These values were guided by the range of autocatalytic growth rates reported for various protein systems in ref. [20], as summarized in Table S1 of ref. [37].

[e] The rate of degradation of SAA protein deposited in kidneys is estimated as:

$$k_{S,deg} = \frac{\ln(2)}{T_{1/2,S}} = 1.93 \times 10^{-4} \text{ s} \tag{37}$$

If it is assumed that under pathological conditions roughly 30–50% of the internalized SAA protein is processed into AA fragments before being fully degraded, the following estimate of the cleavage rate of SAA monomers is obtained:

$$k_{cl} \approx 0.5 k_{S,deg} = 9.65 \times 10^{-5} \text{ s} \tag{38}$$

[f] Substituting the values of $[H]_{tot}$, $[S]_{tot}$, and ω_S from Table 2 into Eq. (13) yields a K_d of 1.1789. This result is of the same order of magnitude as the experimental values reported in ref. [28], who found that the equilibrium dissociation constants for SAA1.1, SAA1.3, and SAA1.5 binding to HDL are 1.4×10^{-5} M, 1.8×10^{-5} M, and 3.7×10^{-6} M, respectively.

[g] 11.4–12.5 kDa [29].

[h] 30-100 μg/mL [30].

[i] 50 years [31].

[j] 4–8 years [9].

[k] Since the monomeric AA fragment itself is a small, disordered peptide, it is subject to the same lysosomal degradation pathways as full-length SAA. Therefore, the half-life of soluble AA monomers in kidneys is also assumed to be 60 min.

[l] Unlike SAA monomers which are rapidly catabolized, AA oligomers formed within the acidic lysosomal environment exhibit more resistance to proteolysis [17]. This is supported by the fact that oligomers persist long enough to disrupt membranes or deposit into fibrils. Since the half-deposition time of AA oligomers into fibrils is assumed to be 24 h, the half-life of AA oligomers is assumed to be 48 h.

[m] AA amyloid fibrils in the kidney are highly stable structures with a long half-life, but they exist in a state of dynamic turnover; significant clearance of these renal deposits can occur over a period of months to years (typically with a lag of >1 year) only if the serum SAA concentration is sustained at low levels

(typically < 0.83 μM (10 mg/L)) [9]. Here the half-life of AA fibrils in kidneys is assumed to be equal to 1 year.

[n] Upon filtration and endocytosis by renal cells, low-molecular-weight proteins are trafficked to lysosomes where they are normally subjected to rapid proteolysis, with a typical half-life of 60 min or less [32]. Based on this, the half-life of SAA monomers in kidneys is assumed to be 60 min.

[o] Value for men.

[p] Ref. [34] found that amyloid-β plaques form extraordinarily quickly, over 24 h. This means that the half-deposition time of amyloid-β oligomers into fibrils must be relatively small, on the order of 24 h. The slow growth of amyloid-β plaques is then explained by the slow production of amyloid-β monomers [38]. Assuming that the same applies to AA plaques, the half-deposition time of AA oligomers into plaques is assumed to be 24 h.

[q] The average density of proteins, independent of their specific type, is commonly approximated as 1.35 g/cm³ [35].

2.2. Calculating the volume occupied by AA fibrils in the kidneys

Renal AA fibril volume growth is determined by the total number of AA oligomers incorporated into the fibrils over time *t*, $N_{mon\ in\ fibrils}(t)$. Since the F-W model assumes equivalent molecular weights for monomeric and oligomeric species (Eq. (17)), the count of deposited monomers serves as a direct measure of fibril volume. Adapting the approach from ref. [39] yields:

$$N_{mon\ in\ fibrils}(t) = \frac{[I](t)}{a_{21}} V_{kidneys} N_A \tag{39}$$

where N_A represents Avogadro's constant.

Alternatively, the number of deposited oligomers can be computed using the volume-based expression from ref. [39]:

$$N_{mon\ in\ fibrils}(t) = \frac{V_{fibrils}(t)\rho_{fibrils}}{MW_{AA}} N_A \tag{40}$$

In this context, MW_{AA} represents the molecular weight of an AA monomer, $\rho_{fibrils}$ is the density of the fibrils, and $V_{fibrils}(t)$ denotes the time-dependent volume of renal AA amyloid deposits.

By equating the right-hand sides of Eqs. (39) and (40) and solving for the fraction of the baseline kidney volume occupied by fibrils, the following is obtained:

$$\frac{V_{fibrils}(t)}{V_{kidneys}} = \frac{[I](t)}{a_{21}} \frac{MW_{AA}}{\rho_{fibrils}} \tag{41}$$

Substituting analytical solution (27) into Eq. (41) yields:

$$\frac{V_{fibrils}(t)}{V_{kidneys}} = \frac{MW_{AA}}{a_{21}\rho_{fibrils}} \frac{\left(1-\exp\left(-\frac{t\ln(2)}{T_{1/2,I}}\right)\right)[B]_{ss} T_{1/2,I}}{\theta_{1/2,B}} \tag{42}$$

This implies that as time approaches infinity, the fraction of baseline kidney volume occupied by fibrils approaches the following steady-state value:

$$\frac{V_{fibrils,ss}}{V_{kidneys}} = \frac{MW_{AA}}{a_{21}\rho_{fibrils}} \frac{[B]_{ss} T_{1/2,I}}{\theta_{1/2,B}} \tag{43}$$

Employing analytical solution (31) (valid for $T_{1/2,I} \to \infty$) in Eq. (41) gives:

$$\frac{V_{fibrils}(t)}{V_{kidneys}} = \frac{MW_{AA}}{a_{21}\rho_{fibrils}} [B]_{ss} \frac{\ln(2)}{\theta_{1/2,B}} t \tag{44}$$

Note that in this case fibrillar volume continues to increase without bound due to the absence of fibril degradation in this scenario.

The total volume of two kidneys at time *t* is given by $V_{fibrils}(t) + V_{kidneys}$.

Despite extensive histopathological characterization of AA amyloidosis, the terminal fibril burden in end-stage renal disease has not been systematically quantified in literature. One autopsy study found 7-11% kidney replacement by AA deposits in advanced disease, but the patient died of pancreatitis, not renal failure [40]. A maximum renal amyloid fraction of 15% at end-stage AA amyloidosis is assumed, as higher burdens would be likely incompatible with the sustained glomerular filtration.

2.3. Accumulated AA oligomer nephrotoxicity, combined nephrotoxic and fibrillar effects, and a proposed biomarker for kidney biological age

Persistently elevated circulating SAA is associated with higher whole-body AA amyloid load and worse clinical outcome [9].

AA amyloidosis pathogenesis is increasingly attributed to stable, protease-resistant SAA oligomers formed at lysosomal pH (3.5–4.5). Unlike soluble SAA or mature fibrils, these pH-stabilized intermediates possess a potent ability to bind and permeabilize lipid membranes. Within the renal environment, SAA internalization likely triggers this oligomerization, leading to lysosomal and plasma membrane disruption. Consequently, kidney damage in AA amyloidosis may be driven not only by the physical accumulation of insoluble fibrils, but also by the membrane-lytic activity of these toxic oligomers [17].

The criterion for characterizing nephrotoxicity follows approaches previously developed to quantify accumulated neurotoxicity from Aβ oligomers in Alzheimer's disease [41] and α-synuclein oligomers in Parkinson's disease [42], as well as accumulated cardiotoxicity in TTR amyloidosis [11] and AL amyloidosis [12].

Accumulated nephrotoxicity is defined as:

$$\Xi(t) = \int_0^t [B](\hat{t})\, d\hat{t} \tag{45}$$

Substituting analytical solution (25) into Eq. (45) yields:

$$\Xi(t) = [B]_{ss}\, t \tag{46}$$

The model assumes that nephrotoxic injury in AA amyloidosis arises from two mechanisms: accumulated cytotoxicity of AA oligomers and aggregation of insoluble fibrils. The combined extent of nephrotoxic damage is quantified by the following parameter:

$$\Xi_{comb}(t) = \Xi(t) + \varpi \frac{V_{fibrils}(t)}{V_{kidneys}} \tag{47}$$

The weighting factor ϖ is estimated based on the assumption that nephrotoxicity from AA oligomers and physical damage from fibril deposition each account for approximately half of the total renal injury in AA amyloidosis. Under conditions of impaired protein degradation with $[H]_{tot} = 15$ μM, the maximum accumulated oligomer toxicity is 2.08×10^9 μM·s (Fig. 6b). Under the same conditions, fibrillar amyloid occupies 14.9% of the total kidney volume (Fig. 7b). Setting the weighting factor such that these two factors contribute equally to Ξ_{comb} yields:

$$\varpi = \frac{2.08 \times 10^9}{0.149} = 1.40 \times 10^{10} \text{ μM s} \tag{48}$$

Ref. [43] proposed aging biomarkers based on aggregation kinetics of intrinsically disordered proteins (IDPs) including Aβ, tau, α-synuclein, and TDP-43. The present study extends this framework to AA amyloidosis, with important distinctions: aggregation occurs primarily in kidneys rather than brain tissue, and SAA must undergo proteolytic cleavage to generate aggregation-competent AA fragments. Biological age of the kidney is therefore defined as:

$$\text{biological age} = \text{calendar age} + c\Xi_{comb}(t) = t_{AA,onset} + t + c\Xi_{comb}(t) \tag{49}$$

Simulations with parameters $h_S = 5.55\times10^{-7}$, $k_1 = 10^{-4}$ s^{-1}, $k_2 = 10^{-4}$ μM^{-1} s^{-1}, $k_{cl} = 9.65\times10^{-5}$ s^{-1}, $T_{1/2,B} = 10^{20}$ s, $T_{1/2,S} = 10^{20}$ s, $T_{1/2,A} = 10^{20}$ s, $T_{1/2,I} = 10^{20}$ s, $\theta_{1/2,B} = 8.64\times10^{4}$ s, $K_d = 1.1789$ μM, $S_{tot} = 8$ μM, and Table 2 values yielded accumulated toxicity of $\Xi_{comb}(t_{AA,f}) = 4.16\times10^{9}$ μM·s. For a clinical scenario with disease onset at age 50, progression over 6 years, and terminal kidney failure (biological age = 100 years) at age 56, parameter c in Eq. (49) becomes:

$$c = \frac{(100-50)-6}{4.16\times10^{9}}(365\times24\times3600) = 0.334 \text{ μM}^{-1} \tag{50}$$

2.4. Sensitivity Analysis of Renal Biological Age

The sensitivity of renal biological age to model parameters was assessed using local sensitivity coefficients, defined as first-order partial derivatives of biological age with respect to individual parameters [44-47]. For example, the sensitivity of the combined damage criterion to the total number of SAA binding sites on HDL particles in plasma, $[H]_{tot}$, was computed via finite differences:

$$\frac{\partial \text{biological age}}{\partial [H]_{tot}} \approx \left.\frac{\text{biological age}\left([H]_{tot} + \Delta[H]_{tot}\right) - \text{biological age}\left([H]_{tot}\right)}{\Delta[H]_{tot}}\right|_{\text{other parmeters kept constant}} \tag{51}$$

where $\Delta[H]_{tot} = 10^{-3}[H]_{tot}$ denotes the step size for numerical differentiation. Multiple step sizes were tested to confirm that sensitivity coefficients were independent of step size selection.

Dimensionless relative sensitivity coefficients were additionally computed to enable direct comparison across parameters differing in units and magnitude [45,47]:

$$S_{[H]_{tot}}^{\text{biological age}} = \frac{[H]_{tot}}{\text{biological age}} \frac{\partial \text{biological age}}{\partial [H]_{tot}} = \frac{\partial \text{biological age} / \text{biological age}}{\partial [H]_{tot} / [H]_{tot}} \tag{52}$$

The dimensionless coefficient $S_{[H]_{tot}}^{\text{biological age}}$ represents the fractional change in biological age per unit fractional change in $[H]_{tot}$, such that a value of $S_{[H]_{tot}}^{\text{biological age}} = 1$ indicates that a 1% increase in $[H]_{tot}$ produces a 1% increase in biological age.

Table 3. Dimensionless sensitivity of biological age to model parameters evaluated at 6 years post-disease onset. Simulations employed the following baseline values: $k_1 = 10^{-4}$ s^{-1}, $k_2 = 10^{-4}$ μM^{-1} s^{-1}, $k_{cl} = 9.65 \times 10^{-5}$ s^{-1}, $K_d = 1.1789$ μM, $h_S = 5.55 \times 10^{-7}$ m s^{-1}, $H_{tot} = 30$ μM, $S_{tot} = 8$ μM, and $\theta_{1/2,B} = 8.64 \times 10^4$ s, with remaining parameters taken from Table 2.

Parameter	Sensitivity for the case of functional protein clearance	Sensitivity for the case of impaired protein degradation pathways
Parameters to which biological age exhibits high sensitivity		
$[H]_{tot}$	-0.0907	-0.294
k_{cl}	0.0663	0.210
Parameters to which biological age exhibits moderate sensitivity		
h_S	0.0188	0.0246
$\theta_{1/2,B}$	0.0381	0.118
K_d	0.0678	0.220
S_{tot}	0.0957	0.310
Parameters to which biological age exhibits low sensitivity		

k_1	0.0145	1.80×10^{-7}
k_2	0.0187	9.18×10^{-7}

3. Results

In human studies, HDL cholesterol usually falls by about 2-fold during strong inflammatory acute-phase responses, while in chronic inflammatory diseases HDL is more often reduced by roughly 1.3–1.5-fold compared with healthy controls [48].

A small equilibrium dissociation constant (K_d) indicates strong binding between SAA and HDL, whereas a large K_d corresponds to relatively weak binding. Fig. 1 illustrates these effects. For the baseline (large) K_d value (1.1789 μM), representing weak binding, the fraction of lipid-free SAA, ω_S , decreases monotonically as the total HDL concentration increases (Fig. 1a). Conversely, the fraction of unbound HDL, ω_H , rises with increasing total HDL concentration (Fig. 1b).

In contrast, for a very small K_d of 10^{-10} μM (tight binding), the fraction of lipid-free SAA decreases linearly until the HDL concentration reaches a threshold of 8 μM . This threshold corresponds to the SAA concentration of 8 μM used in the simulation. Once the HDL concentration exceeds 8 μM , the free SAA fraction remains at zero, as all SAA molecules are sequestered by HDL (Fig. 1a).

Figures S1–S3 demonstrate that the molar concentrations of SAA, AA monomers, and free AA oligomers in the kidneys ($[S]_{kidney}$, $[A]$, and $[B]$, respectively) rapidly attain constant steady-state values. This validates the steady-state approximation underlying the analytical solutions given by Eqs. (16), (24), and (25). Furthermore, all three concentrations increase with decreasing HDL levels, in agreement with published evidence showing that inflammatory depletion of HDL reduces available SAA binding capacity, thereby enabling liver-derived SAA to saturate HDL particles and generate an excess of free, lipid-poor SAA in the bloodstream [6,49]. Lipid-poor SAA promotes renal inflammation and can participate in amyloid formation [50].

The molar concentration of AA oligomers incorporated into amyloid fibrils in the kidneys, $[I]$, increases over time. For physiologically relevant AA species half-lives, fibril accumulation slows progressively over time and converges to the steady-state burden predicted by Eq. (28) (Fig. S4a). By contrast, when fibril degradation is absent (infinite half-life scenario), fibril burden increases linearly and indefinitely

(Fig. S4b). A reduction in plasma HDL concentration leads to greater fibril accumulation in the kidneys. The fraction of kidney volume occupied by fibrils displays similar behavior, asymptotically approaching a steady-state value in Fig. S5a. Reduced plasma HDL concentration likewise drives increased fibril accumulation within the renal parenchyma (Fig. S5a,b).

Accumulated AA oligomer nephrotoxicity increases linearly with time under both finite and infinite half-life scenarios of AA species (Fig. S6a,b). This linear increase is a direct consequence of the definition of accumulated nephrotoxicity as the time integral of free oligomer concentration $[B]$ (Eq. (45)): since $[B]$ rapidly attains and maintains a constant steady-state value for most of the disease course (Fig. S3), its time integral increases linearly. Furthermore, reduced plasma HDL concentration leads to greater accumulated nephrotoxicity (Fig. S6a,b).

The combined nephrotoxic injury in AA amyloidosis, Ξ_{comb}, which accounts for two mechanisms of renal damage: accumulated cytotoxicity of AA oligomers and aggregation of insoluble fibrils, increases with time. This increase is slowing down with time for the case of biologically relevant values of half-lives of AA species (Fig. 2a) and remains linear for the case in infinitely long half-lives (no AA species degradation) (Fig. 2b). The combined nephrotoxic injury increases if plasma HDL concentration is reduced.

The combined nephrotoxic damage criterion Ξ_{comb} is inherently irreversible. Even if a treatment capable of clearing all fibrillar deposits, such as fibril-specific monoclonal antibodies [51], were developed and administered at 6 years post-onset, it would not reset Ξ_{comb} to zero. This irreversibility arises because Ξ_{comb} comprises two contributions: fibril burden, which is amenable to therapeutic clearance, and accumulated oligomer cytotoxicity, which integrates continuously over time (Eq. (45)) and cannot be reversed. Fibril-clearing therapy would therefore reduce Ξ_{comb} but not restore it to zero (black starred line, Fig. 3).

The combined nephrotoxic injury is also path-dependent rather than state-dependent. In a hypothetical scenario where $[B]$ increases linearly throughout disease progression (blue diamond line, Fig. S7), Ξ_{comb} attains a lower value at 6 years than predicted by the model, where $[B]$ maintains a constant steady-state value for most of the disease course (red square line, Fig. S7). This occurs despite both scenarios producing identical values of $[B]$ and $\frac{V_{fibrils}(t)}{V_{kidneys}}$ at $t = 6$ years, demonstrating that the history of oligomer exposure, not merely its current level, determines the extent of nephrotoxic damage.

Renal biological age at various HDL concentrations (Fig. 4) exhibits behavior analogous to that of Ξ_{comb} in Fig. 2. This similarity follows directly from the assumed linear proportionality between biological age and Ξ_{comb} (Eq. (49)). Biological age increases more rapidly when impaired protein degradation pathways are assumed (Fig. 4b) and rises with decreasing total HDL concentration.

The sensitivity of biological age to total HDL concentration is negative (Fig. 5), indicating that biological age decreases with increasing HDL concentration, consistent with the trends observed in Fig. 4. The magnitude of the dimensionless sensitivity decreases as HDL concentration increases.

Increasing the SAA cleavage rate constant k_{cl} decreases renal SAA monomer concentration (Fig. S8) while increasing AA monomer and free oligomer concentrations (Figs. S9, S10). A notable counterintuitive result emerges when comparing half-life scenarios: although oligomer concentrations are approximately twice as high under infinite half-lives (Fig. S10b) as under physiologically relevant conditions (Fig. S10a), AA monomer concentrations are paradoxically lower (Fig. S9b vs. S9a). This is explained by accelerated autocatalytic conversion of monomers to oligomers driven by the elevated oligomer concentration (Eq. (18)).

The concentration of AA oligomers incorporated into fibrillar deposits in the kidneys (Fig. S11), the fractional kidney volume occupied by fibrils (Fig. S12), and accumulated nephrotoxicity (Fig. S13) all increase with the SAA cleavage rate constant. For physiologically relevant half-lives, $[I]$ and fibril volume fraction $\frac{V_{fibrils}}{V_{kidneys}}$ increase at a decelerating rate, whereas infinite half-lives produce linear growth (Figs. S11, S12). In contrast, accumulated nephrotoxicity increases linearly with time under both finite and infinite half-life scenarios (Fig. S13). This linear behavior follows directly from the definition of accumulated nephrotoxicity as the time integral of $[B]$ (Eq. (45)): since $[B]$ attains and maintains a constant steady-state value for most of the disease course (Fig. S10), its integral increases linearly with time.

Combined renal damage from accumulated AA oligomer cytotoxicity and insoluble fibril burden increases with the SAA cleavage rate constant (Fig. 14), with renal biological age exhibiting the same trend (Fig. 6). For the largest cleavage rate constant considered, $k_{cl} = 9.65 \times 10^{-4}$ s^{-1}, terminal kidney failure, defined as biological age reaching 100 years, is predicted after approximately 3.5 years of disease progression under the infinite AA species half-life scenario (Fig. 6b).

The sensitivity of biological age to the SAA cleavage rate constant is positive (Fig. 7), indicating that biological age increases with increasing k_{cl}. The magnitude of the dimensionless sensitivity increases with the cleavage rate constant.

Renal biological age increases with the mass transfer coefficient h_S characterizing free SAA transport from plasma into the kidneys (Fig. S15). Consistent with this trend, the sensitivity of biological age to h_S is positive (Fig. S16). Notably, for physiologically relevant half-lives, the dimensionless sensitivity coefficient exhibits non-monotonic behavior with respect to h_S: it initially increases and subsequently decreases with increasing h_S (Fig. S16a).

Renal biological age increases with the half-deposition time $\theta_{1/2,B}$ characterizing incorporation of free AA oligomers into fibrillar deposits (Fig. S17). Consistent with this trend, the sensitivity of biological age to $\theta_{1/2,B}$ is positive (Fig. S18). Under physiologically relevant half-life conditions, the dimensionless sensitivity magnitude exhibits non-monotonic behavior with respect to $\theta_{1/2,B}$: it initially increases and subsequently decreases with increasing $\theta_{1/2,B}$ (Fig. S18a).

Renal biological age increases with the equilibrium dissociation constant K_d characterizing SAA-HDL binding affinity (Fig. S19). This behavior reflects the inverse relationship between K_d and binding affinity: a small K_d corresponds to tight SAA-HDL association, reducing the concentration of free SAA available for renal filtration and deposition. Consistent with this trend, the sensitivity of biological age to K_d is positive (Fig. S20), with the sensitivity magnitude increasing monotonically with K_d.

Renal biological age increases with total SAA concentration (HDL-bound and free combined) (Fig. S21). For a given equilibrium dissociation constant K_d, higher total SAA concentration yields a proportionally larger free SAA pool available for renal filtration and deposition. Consistent with this trend, the sensitivity of biological age to total SAA concentration is positive, with its magnitude increasing monotonically with total SAA concentration (Fig. S22).

Under physiologically relevant half-life conditions of AA species, renal biological age increases with the first pseudo-elementary (nucleation) rate constant k_1 of the F-W model, with this dependence becoming pronounced at larger values of k_1 (Fig. S23a). Under infinite half-life conditions, biological age exhibits negligible dependence on k_1 (Fig. S23b). The sensitivity of biological age to k_1 is positive under

physiologically relevant conditions, increasing in magnitude with k_1 (Fig. S24a). Under infinite half-life conditions, the dimensionless sensitivity is negligibly small, on the order of 10^{-6} (Fig. S24b).

The dependence of renal biological age on the second pseudo-elementary (autocatalytic growth) rate constant k_2 of the F-W model is analogous to that of k_1. Under functional protein clearance conditions, biological age increases with k_2, particularly at larger values of k_2 (Fig. S25a). When protein clearance is impaired, however, the dependence of biological age on k_2 becomes negligible (Fig. S25b). The sensitivity of biological age to k_2 is positive but small for both scenarios (Fig. S26), with the dimensionless sensitivity becoming of order 10^{-5} under impaired protein degradation (Fig. S26b).

Table 3 classifies model parameters into three groups according to the sensitivity of biological age to each parameter. Biological age is most sensitive to the total number of SAA binding sites on HDL particles, $[H]_{tot}$, and the proteolytic SAA cleavage rate constant, k_{cl}. Moderate sensitivity is observed with respect to the mass transfer coefficient h_S, half-deposition time $\theta_{1/2,B}$, dissociation constant K_d, and total SAA concentration S_{tot}. Biological age exhibits low sensitivity to the F-W nucleation and autocatalytic growth rate constants k_1 and k_2.

4. Discussion, limitations of the model, and future directions

The model reveals that AA amyloidosis progression is governed by the dynamic equilibrium between circulating SAA and the protective buffering capacity of HDL. Within the bloodstream, HDL functions as a chaperone-like carrier for SAA, binding its N-terminal lipid-binding surface to sequester amyloidogenic segments and curtail SAA's tendency to misfold and promote inflammation [52].

While sufficient HDL concentration maintains circulating SAA in a sequestered, non-pathogenic state, chronic inflammation disrupts this protective equilibrium by simultaneously promoting SAA overproduction and reducing HDL levels [48]. The model demonstrates that this dual perturbation diminishes available HDL binding sites, allowing circulating SAA to overwhelm the buffering capacity of HDL and generate a pathogenic pool of free, lipid-poor SAA [6,49], the species that are ultimately responsible for accelerating renal biological aging through fibril deposition and oligomer-mediated inflammation [50].

The model further predicts that higher total SAA concentrations proportionally expand this free SAA pool, accelerating renal filtration and biological aging. This finding is consistent with the cornerstone of

current AA amyloidosis therapy: aggressive suppression of the underlying inflammatory disease using anti-inflammatory and immunosuppressive agents to reduce cytokine-driven SAA synthesis. Clinical evidence consistently demonstrates that sustained SAA reduction or normalization, through biologic agents, disease-modifying drugs, or targeted antimicrobial therapy, stabilizes tissue AA deposits and preserves organ function [53].

A central and clinically significant finding of this study is that the combined nephrotoxic damage criterion is both irreversible and path-dependent. Irreversibility arises from the dual nature of the criterion: while the physical burden of insoluble fibrillar deposits can be reduced by therapeutic clearance, accumulated oligomer cytotoxicity integrates continuously over time and cannot be undone. The model therefore predicts that even complete clearance of fibrillar deposits by late-stage therapy, such as fibril-specific monoclonal antibodies [51] administered at six years post-onset, would reduce but not reset the kidney's biological age.

This irreversible accumulation of damage reflects the path-dependent nature of nephrotoxic injury: the trajectory of oligomer exposure, not merely its final value, determines disease severity. For instance, a scenario in which oligomer concentration increases linearly to a given level produces different cumulative damage than one in which the same concentration is maintained as a steady-state throughout the disease course. By integrating both the visible fibril burden and the cumulative history of oligomeric toxicity, the proposed criterion captures disease severity more comprehensively than conventional histological assessment. Critically, path-dependence implies that early therapeutic intervention is paramount: each year of delayed treatment irreversibly advances biological age, rendering late-stage fibril clearance increasingly insufficient for restoring renal function.

Finally, sensitivity analysis reveals that renal biological aging is most strongly influenced by the protective capacity of the HDL buffering system and the rate of upstream lysosomal SAA processing, not by downstream aggregation kinetics. This finding indicates that AA amyloidosis is fundamentally supply-limited: disease progression is driven primarily by the availability of free SAA and AA fragments rather than by the intrinsic kinetics of amyloid fibril assembly.

The model has limitations related to several simplifying assumptions. The SAA-HDL binding model assumes a one-to-one stoichiometry, whereas HDL particles can accommodate multiple SAA monomers in vivo; future models should incorporate multi-site binding. The aggregation kinetics is described by the two-step Finke-Watzky mechanism, a minimal model that does not distinguish between oligomers of different sizes, which may differ in their nephrotoxic potency. The model further treats kidneys as spatially homogeneous compartments, neglecting their spatial heterogeneity. Finally, extending the

framework to model the effects of therapeutic interventions on the trajectory of renal biological age would provide clinically actionable predictions and could ultimately support personalized treatment planning for patients at risk of AA amyloidosis.

Author Contribution Statement

AVK is the sole author of this paper.

Funding Data

National Science Foundation (Grant No. DMS-2451660; Funder ID: 10.13039/100000146).

Alexander von Humboldt Foundation through the Humboldt Research Award (Funder ID: 10.13039/100005156).

Conflict of Interest

The author declares no competing interests.

Data Availability Statement

This article has no additional data.

References

1. Lachmann HJ, Hawkins PN. Systemic amyloidosis. *Current opinion in pharmacology* 2006; **6**(2):214–220. doi:10.1016/j.coph.2005.10.005.

2. Lachmann HJ, Goodman HJB, Gilbertson JA, et al. Natural history and outcome in systemic AA amyloidosis. *The New England journal of medicine* 2007; **356**(23):2361–2371. doi:10.1056/NEJMoa070265.

3. Westermark GT, Westermark P. Serum amyloid A and protein AA: molecular mechanisms of a transmissible amyloidosis. *FEBS letters* 2009; **583**(16):2685–2690. doi:10.1016/j.febslet.2009.04.026.

4. Kluve-Beckerman B, Smith JT, Ivancic C, Benson MD. Post-translational modification of amyloid a protein in patients with AA amyloidosis. *Amyloid* 2022; **29**(1):50–57. doi:10.1080/13506129.2021.1997985.

5. Frame NM, Gursky O. Structure of serum amyloid A suggests a mechanism for selective lipoprotein binding and functions: SAA as a hub in macromolecular interaction networks. *FEBS letters* 2016; **590**(6):866–879. doi:10.1002/1873-3468.12116.

6. Webb NR. High-Density Lipoproteins and Serum Amyloid A (SAA). *Current atherosclerosis reports* 2021; **23**(2):7. doi:10.1007/s11883-020-00901-4.

7. Ji A, Wang X, Noffsinger VP, et al. Serum amyloid A is not incorporated into HDL during HDL biogenesis. *Journal of lipid research* 2020; **61**(3):328–337. doi:10.1194/jlr.RA119000329.

8. Röcken C, Shakespeare A. Pathology, diagnosis and pathogenesis of AA amyloidosis. *Virchows Archiv : an international journal of pathology* 2002; **440**(2):111–122. doi:10.1007/s00428-001-0582-9.

9. Gillmore JD, Lovat LB, Persey MR, Pepys MB, Hawkins PN. Amyloid load and clinical outcome in AA amyloidosis in relation to circulating concentration of serum amyloid A protein. *Lancet (London, England)* 2001; **358**(9275):24–29. doi:10.1016/S0140-6736(00)05252-1.

10. Knowles TPJ, Waudby CA, Devlin GL, et al. An Analytical Solution to the Kinetics of Breakable Filament Assembly. *Science* 2009; **326**(5959):1533–1537. doi:10.1126/science.1178250.

11. Kuznetsov AV. Does Human Transthyretin Aggregate in Blood Plasma or in Cardiac Tissue? A Mathematical Modeling Study. *bioRxiv* 2025:2025.07.29.667417. doi:10.1101/2025.07.29.667417.

12. Kuznetsov AV. Mathematical Modeling of Light Chain Aggregation and Cardiac Damage in AL Amyloidosis. *bioRxiv* 2026:2025.10.30.685705. doi:10.1101/2025.10.30.685705.

13. Artl A, Marsche G, Lestavel S, Sattler W, Malle E. Role of Serum Amyloid A During Metabolism of Acute-Phase HDL by Macrophages. *Arteriosclerosis, Thrombosis, and Vascular Biology* 2000; **20**(3):763–772. doi:10.1161/01.ATV.20.3.763.

14. Cohen SIA, Linse S, Luheshi LM, et al. Proliferation of amyloid-β42 aggregates occurs through a secondary nucleation mechanism. *Proceedings of the National Academy of Sciences of the United States of America* 2013; **110**(24):9758–9763. doi:10.1073/pnas.1218402110.

15. Thomas MJ, Sorci-Thomas MG. SAA: a link between cholesterol efflux capacity and inflammation? *Journal of lipid research* 2015; **56**(8):1383–1385. doi:10.1194/jlr.C061366.

16. Kon V, Yang H-C, Smith LE, Vickers KC, Linton MF. High-Density Lipoproteins in Kidney Disease. *International journal of molecular sciences* 2021; **22**(15). doi:10.3390/ijms22158201.

17. Jayaraman S, Gantz DL, Haupt C, Gursky O. Serum amyloid A forms stable oligomers that disrupt vesicles at lysosomal pH and contribute to the pathogenesis of reactive amyloidosis. *Proceedings of the National Academy of Sciences* 2017; **114**(32):E6507–E6515. doi:10.1073/pnas.1707120114.

18. Lu J, Yu Y, Zhu I, Cheng Y, Sun PD. Structural mechanism of serum amyloid A-mediated inflammatory amyloidosis. *Proceedings of the National Academy of Sciences* 2014; **111**(14):5189–5194. doi:10.1073/pnas.1322357111.

19. Miura K, Takahashi Y, Shirasawa H. Immunohistochemical detection of serum amyloid A protein in the liver and the kidney after casein injection. *Laboratory investigation; a journal of technical methods and pathology* 1985; **53**(4):453–463.

20. Morris AM, Watzky MA, Agar JN, Finke RG. Fitting neurological protein aggregation kinetic data via a 2-step, Minimal/"Ockham's Razor" model: The Finke-Watzky mechanism of nucleation followed by autocatalytic surface growth. *Biochemistry* 2008; **47**(8):2413–2427. doi:10.1021/bi701899y.

21. Iashchishyn IA, Sulskis D, Ngoc MN, Smirnovas V, Morozova-Roche LA. Finke-Watzky Two-Step Nucleation-Autocatalysis Model of S100A9 Amyloid Formation: Protein Misfolding as "Nucleation" Event. *ACS chemical neuroscience* 2017; **8**:2152–2158. doi:10.1021/acschemneuro.7b00251.

22. Finke RG, Watzky MA, Whitehead CB. Response to "Particle Size Is a Primary Determinant for Sigmoidal Kinetics of Nanoparticle Formation: A 'Disproof' of the Finke–Watzky (F-W) Nanoparticle Nucleation and Growth Mechanism." *Chemistry of Materials* 2020; **32**(8):3657–3672. doi:10.1021/acs.chemmater.0c00780.

23. Aragonès Pedrola J, Dekker FA, Garfagnini T, et al. FibrilPaint to determine the length of Tau amyloids in fluids. *Proceedings of the National Academy of Sciences* 2025; **122**(44):e2502847122. doi:10.1073/pnas.2502847122.

24. Boltachev GS, Ivanov MG. Effect of nanoparticle concentration on coagulation rate of colloidal suspensions. *Heliyon* 2020; **6**(2):e03295. doi:10.1016/j.heliyon.2020.e03295.

25. Ahbap E, Kara E, Sahutoglu T, et al. Outcome of 121 patients with renal amyloid a amyloidosis. *Journal of research in medical sciences : the official journal of Isfahan University of Medical Sciences* 2014; **19**(7):644–649.

26. Bohle A, Aeikens B, Eenboom A, et al. Human glomerular structure under normal conditions and in isolated glomerular disease. *Renal Hemodynamics: Cellular and Molecular Determinants* 1998; **54**:S186–S188. doi:10.1046/j.1523-1755.1998.06742.x.

27. Hutchins PM, Ronsein GE, Monette JS, et al. Quantification of HDL particle concentration by calibrated ion mobility analysis. *Clinical chemistry* 2014; **60**(11):1393–1401. doi:10.1373/clinchem.2014.228114.

28. Yamada T, Sato J, Okuda Y. Differential affinity of serum amyloid A1 isotypes for high-density lipoprotein. *Amyloid* 2009; **16**(4):196–200. doi:10.3109/13506120903421546.

29. Güleç GU, Turgut YB, Turgut M. Acute Phase Proteins. In: Rezaei N, ed. *Encyclopedia of Infection and Immunity*. Oxford: Elsevier; 2022:206–214.

30. Wilson PG, Thompson JC, Shridas P, et al. Serum Amyloid A Is an Exchangeable Apolipoprotein. *Arteriosclerosis, thrombosis, and vascular biology* 2018; **38**(8):1890–1900. doi:10.1161/ATVBAHA.118.310979.

31. Mirioglu S, Uludag O, Hurdogan O, et al. AA Amyloidosis: A Contemporary View. *Current rheumatology reports* 2024; **26**(7):248–259. doi:10.1007/s11926-024-01147-8.

32. Carson JM, Okamura K, Wakashin H, et al. Podocytes degrade endocytosed albumin primarily in lysosomes. *PloS one* 2014; **9**(6):e99771. doi:10.1371/journal.pone.0099771.

33. Cheong B, Muthupillai R, Rubin MF, Flamm SD. Normal values for renal length and volume as measured by magnetic resonance imaging. *Clinical journal of the American Society of Nephrology : CJASN* 2007; **2**(1):38–45. doi:10.2215/CJN.00930306.

34. Meyer-Luehmann M, Spires-Jones TL, Prada C, et al. Rapid appearance and local toxicity of amyloid-beta plaques in a mouse model of Alzheimer's disease. *Nature* 2008; **451**:720–724. doi:10.1038/nature06616.

35. Cavicchi RE, King J, Ripple DC. Measurement of Average Aggregate Density by Sedimentation and Brownian Motion Analysis. *Journal of pharmaceutical sciences* 2018; **107**(5):1304–1312. doi:10.1016/j.xphs.2018.01.013.

36. Hall JE. *Guyton and Hall Textbook of Medical Physiology*. 13th ed. Philadelphia, PA: Elsevier; 2016.

37. Kuznetsov AV. Modeling the growth of cytosolic TDP-43 inclusion bodies and accumulated neurotoxicity of misfolded oligomers in neurons. *bioRxiv* 2025:2023.11.28.569118. doi:10.1101/2023.11.28.569118.

38. Kuznetsov AV. Numerical and analytical simulation of the growth of amyloid-β plaques. *ASME Journal of Biomedical Engineering* 2024; **146**:061004. doi:10.1115/1.4064969.

39. Watzky MA, Finney EE, Finke RG. Transition-Metal Nanocluster Size vs Formation Time and the Catalytically Effective Nucleus Number: A Mechanism-Based Treatment. *Journal of the American Chemical Society* 2008; **130**(36):11959–11969. doi:10.1021/ja8017412.

40. Kuroda T, Tanabe N, Sato H, et al. Distribution of amyloid deposits in the kidneys of a patient with reactive amyloidosis associated with rheumatoid arthritis. *BMC research notes* 2013; **6**:231. doi:10.1186/1756-0500-6-231.

41. Kuznetsov AV. A criterion characterizing accumulated neurotoxicity of Aβ oligomers in Alzheimer's disease. *Proceedings of the Royal Society A* 2025; **481**:20240652. doi:10.1098/rspa.2024.0652.

42. Kuznetsov AV. Criterion for assessing accumulated neurotoxicity of alpha-synuclein oligomers in Parkinson's disease. *International Journal for Numerical Methods in Biomedical Engineering* 2025; **41**:e70027. doi:doi.org/10.1002/cnm.70027.

43. Dormann D, Lemke EA. Adding intrinsically disordered proteins to biological ageing clocks. *Nature Cell Biology* 2024; **26**(6):851–858. doi:10.1038/s41556-024-01423-w.

44. Beck JV, Arnold KJ. *Parameter Estimation in Science and Engineering*. New York: Wiley; 1977.

45. Zadeh KS, Montas HJ. A class of exact solutions for biomacromolecule diffusion-reaction in live cells. *Journal of theoretical biology* 2010; **264**(3):914–933. doi:10.1016/j.jtbi.2010.03.028.

46. Zi Z. Sensitivity analysis approaches applied to systems biology models. *Iet Systems Biology* 2011; **5**(6):336–346. doi:10.1049/iet-syb.2011.0015.

47. Kuznetsov IA, Kuznetsov AV. Investigating sensitivity coefficients characterizing the response of a model of tau protein transport in an axon to model parameters. *Computer methods in biomechanics and biomedical engineering* 2019; **22**(1):71–83. doi:10.1080/10255842.2018.1534233.

48. Jahangiri A, de Beer MC, Noffsinger V, et al. HDL remodeling during the acute phase response. *Arteriosclerosis, thrombosis, and vascular biology* 2009; **29**(2):261–267. doi:10.1161/ATVBAHA.108.178681.

49. Schuchardt M, Prüfer N, Tu Y, et al. Dysfunctional high-density lipoprotein activates toll-like receptors via serum amyloid A in vascular smooth muscle cells. *Scientific Reports* 2019; **9**(1):3421. doi:10.1038/s41598-019-39846-3.

50. Simons JP, Al-Shawi R, Ellmerich S, et al. Pathogenetic mechanisms of amyloid A amyloidosis. *Proceedings of the National Academy of Sciences of the United States of America* 2013; **110**(40):16115–16120. doi:10.1073/pnas.1306621110.

51. Thorne J, Clark D, Geldenhuys L, More K, Vinson A, Tennankore K. Serum Amyloid A Protein-Associated Kidney Disease: Presentation, Diagnosis, and Management. *Kidney medicine* 2022; **4**(8):100504. doi:10.1016/j.xkme.2022.100504.

52. Zhu S, Wang Y, Chen W, et al. High-Density Lipoprotein (HDL) Counter-Regulates Serum Amyloid A (SAA)-Induced sPLA2-IIE and sPLA2-V Expression in Macrophages. *PloS one* 2016; **11**(11):e0167468. doi:10.1371/journal.pone.0167468.

53. Real de Asúa D, Costa R, Galván JM, Filigheddu MT, Trujillo D, Cadiñanos J. Systemic AA amyloidosis: epidemiology, diagnosis, and management. *Clinical epidemiology* 2014; **6**:369–377. doi:10.2147/CLEP.S39981.

Figure captions

Fig. 1. (a) Fraction of lipid-free SAA, ω_S. (b) Fraction of HDL particles that are not bound to SAA, ω_H. The cases of baseline value of equilibrium dissociation constant, $K_d = 1.1789\ \mu\text{M}$, and a very small value of equilibrium dissociation constant, $K_d = 10^{-10}\ \mu\text{M}$.

Fig. 2. Combined renal damage from accumulated AA oligomer cytotoxicity and insoluble fibril burden as a function of time. (a) Biologically relevant half-lives $T_{1/2,A}$, $T_{1/2,B}$, $T_{1/2,I}$, and $T_{1/2,S}$, representing functional protein degradation machinery. (b) Infinite half-lives $T_{1/2,A}$, $T_{1/2,B}$, $T_{1/2,I}$, and $T_{1/2,S}$, representing complete impairment of protein degradation. Each panel shows results for three values of the total number of SAA binding sites on HDL particles in plasma. Baseline parameters: $k_1 = 10^{-4}$ s^{-1}, $k_2 = 10^{-4}$ μM^{-1} s^{-1}, $k_{cl} = 9.65\times10^{-5}$ s^{-1}, $K_d = 1.1789\ \mu\text{M}$, $h_S = 5.55\times10^{-7}$ m s^{-1}, $S_{tot} = 8\ \mu\text{M}$, and $\theta_{1/2,B} = 8.64\times10^{4}$ s; remaining parameters as listed in Table 2.

Fig. 3. Combined renal damage from accumulated AA oligomer cytotoxicity and insoluble fibril burden as a function of time. Three scenarios are compared: the model prediction, in which $[B]$ rapidly attains a constant steady-state value early in the disease course; a modified scenario following model predictions for $[B]$ but with instantaneous removal of all fibrillar deposits at 6 years post-onset; and a hypothetical scenario in which $[B]$ increases linearly throughout disease progression (see Fig. S7). (a) Biologically relevant half-lives $T_{1/2,A}$, $T_{1/2,B}$, $T_{1/2,I}$, and $T_{1/2,S}$, representing functional protein degradation machinery. (b) Infinite half-lives $T_{1/2,A}$, $T_{1/2,B}$, $T_{1/2,I}$, and $T_{1/2,S}$, representing complete impairment of protein degradation. Baseline parameters: $k_1 = 10^{-4}$ s^{-1}, $k_2 = 10^{-4}$ μM^{-1} s^{-1}, $k_{cl} = 9.65\times10^{-5}$ s^{-1}, $K_d = 1.1789\ \mu\text{M}$, $h_S = 5.55\times10^{-7}$ m s^{-1}, $H_{tot} = 30\ \mu\text{M}$, $S_{tot} = 8\ \mu\text{M}$, and $\theta_{1/2,B} = 8.64\times10^{4}$ s; remaining parameters as listed in Table 2.

Fig. 4. Biological age of the kidney as a function of time. (a) Biologically relevant half-lives $T_{1/2,A}$, $T_{1/2,B}$, $T_{1/2,I}$, and $T_{1/2,S}$, representing functional protein degradation machinery. (b) Infinite half-lives $T_{1/2,A}$, $T_{1/2,B}$, $T_{1/2,I}$, and $T_{1/2,S}$, representing complete impairment of protein degradation. Each panel shows results for three values of the total number of SAA binding sites on HDL particles in plasma. Baseline parameters:

$k_1 = 10^{-4}$ s^{-1}, $k_2 = 10^{-4}$ μM^{-1} s^{-1}, $k_{cl} = 9.65 \times 10^{-5}$ s^{-1}, $K_d = 1.1789$ μM, $h_S = 5.55 \times 10^{-7}$ m s^{-1}, $S_{tot} = 8$ μM, and $\theta_{1/2,B} = 8.64 \times 10^4$ s; remaining parameters as listed in Table 2.

Fig. 5. Dimensionless sensitivity of renal biological age to the total number of SAA binding sites on HDL particles in plasma, as a function of time. (a) Biologically relevant half-lives $T_{1/2,A}$, $T_{1/2,B}$, $T_{1/2,I}$, and $T_{1/2,S}$, representing functional protein degradation machinery. (b) Infinite half-lives $T_{1/2,A}$, $T_{1/2,B}$, $T_{1/2,I}$, and $T_{1/2,S}$, representing complete impairment of protein degradation. Each panel shows results for three values of the total number of SAA binding sites on HDL particles in plasma. Baseline parameters: $k_1 = 10^{-4}$ s^{-1}, $k_2 = 10^{-4}$ μM^{-1} s^{-1}, $k_{cl} = 9.65 \times 10^{-5}$ s^{-1}, $K_d = 1.1789$ μM, $h_S = 5.55 \times 10^{-7}$ m s^{-1}, $S_{tot} = 8$ μM, and $\theta_{1/2,B} = 8.64 \times 10^4$ s; remaining parameters as listed in Table 2.

Fig. 6. Biological age of the kidney as a function of time. (a) Biologically relevant half-lives $T_{1/2,A}$, $T_{1/2,B}$, $T_{1/2,I}$, and $T_{1/2,S}$, representing functional protein degradation machinery. (b) Infinite half-lives $T_{1/2,A}$, $T_{1/2,B}$, $T_{1/2,I}$, and $T_{1/2,S}$, representing complete impairment of protein degradation. Each panel shows results for three values of the rate constant for proteolytic cleavage of SAA that generates AA monomers. Baseline parameters: $k_1 = 10^{-4}$ s^{-1}, $k_2 = 10^{-4}$ μM^{-1} s^{-1}, $K_d = 1.1789$ μM, $h_S = 5.55 \times 10^{-7}$ m s^{-1}, $H_{tot} = 30$ μM, $S_{tot} = 8$ μM, and $\theta_{1/2,B} = 8.64 \times 10^4$ s.; remaining parameters as listed in Table 2.

Fig. 7. Dimensionless sensitivity of renal biological age to the rate constant for proteolytic cleavage of SAA that generates AA monomers, as a function of time. (a) Biologically relevant half-lives $T_{1/2,A}$, $T_{1/2,B}$, $T_{1/2,I}$, and $T_{1/2,S}$, representing functional protein degradation machinery. (b) Infinite half-lives $T_{1/2,A}$, $T_{1/2,B}$, $T_{1/2,I}$, and $T_{1/2,S}$, representing complete impairment of protein degradation. Each panel shows results for three values of the rate constant for proteolytic cleavage of SAA that generates AA monomers. Baseline parameters: $k_1 = 10^{-4}$ s^{-1}, $k_2 = 10^{-4}$ μM^{-1} s^{-1}, $K_d = 1.1789$ μM, $h_S = 5.55 \times 10^{-7}$ m s^{-1}, $H_{tot} = 30$ μM, $S_{tot} = 8$ μM, and $\theta_{1/2,B} = 8.64 \times 10^4$ s.; remaining parameters as listed in Table 2.

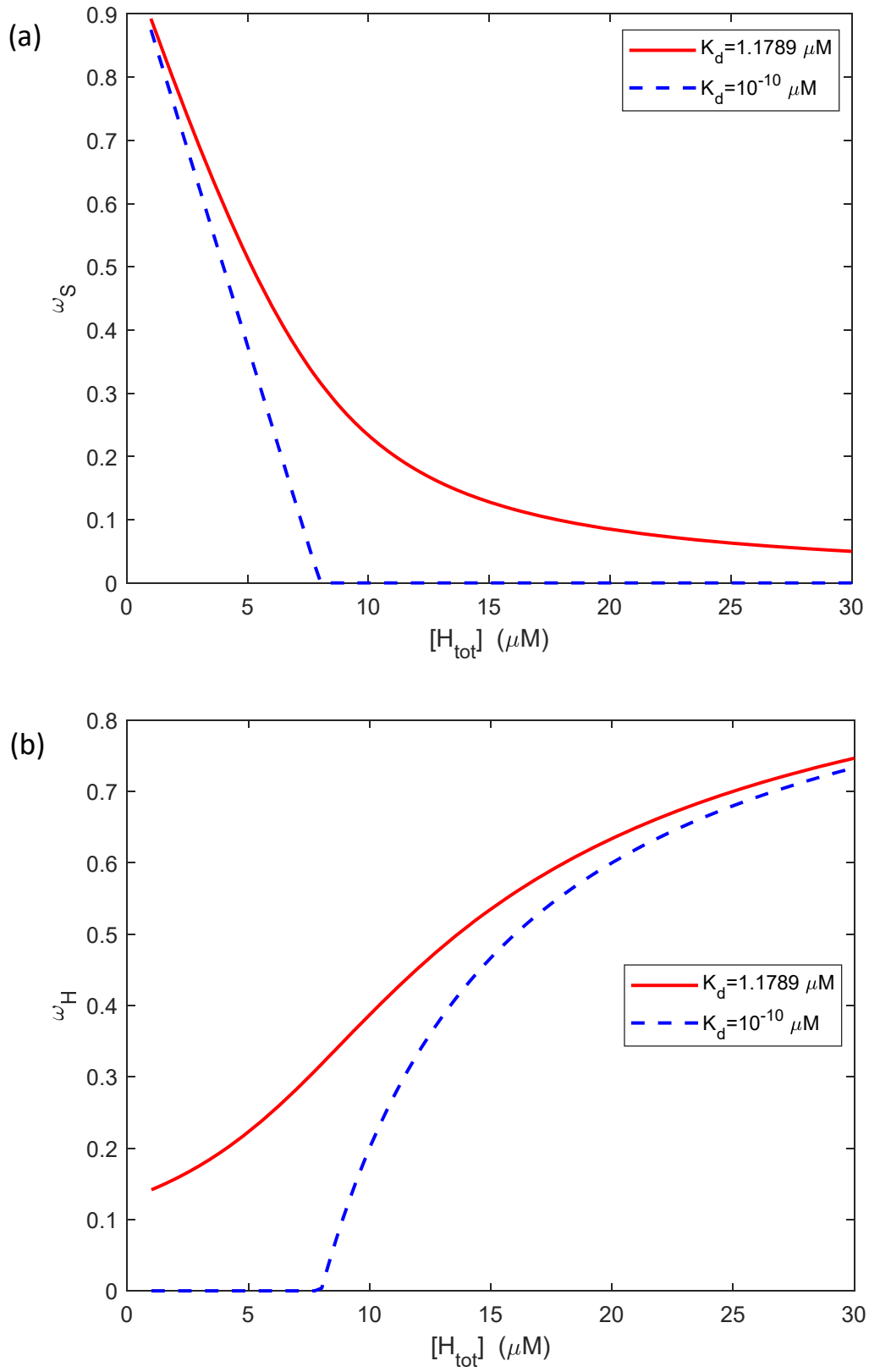
(a)
0.9
0.8
0.7
0.6
0.5
0.4
0.3
0.2
0.1
0
ω_S
0
5
10
15
20
25
30
$[H_{tot}]$ (μM)
K_d=1.1789 μM
K_d=10^{-10} μM
(b)
0.8
0.7
0.6
0.5
0.4
0.3
0.2
0.1
0
ω_H
0
5
10
15
20
25
30
$[H_{tot}]$ (μM)
K_d=1.1789 μM
K_d=10^{-10} μM

Figure 1

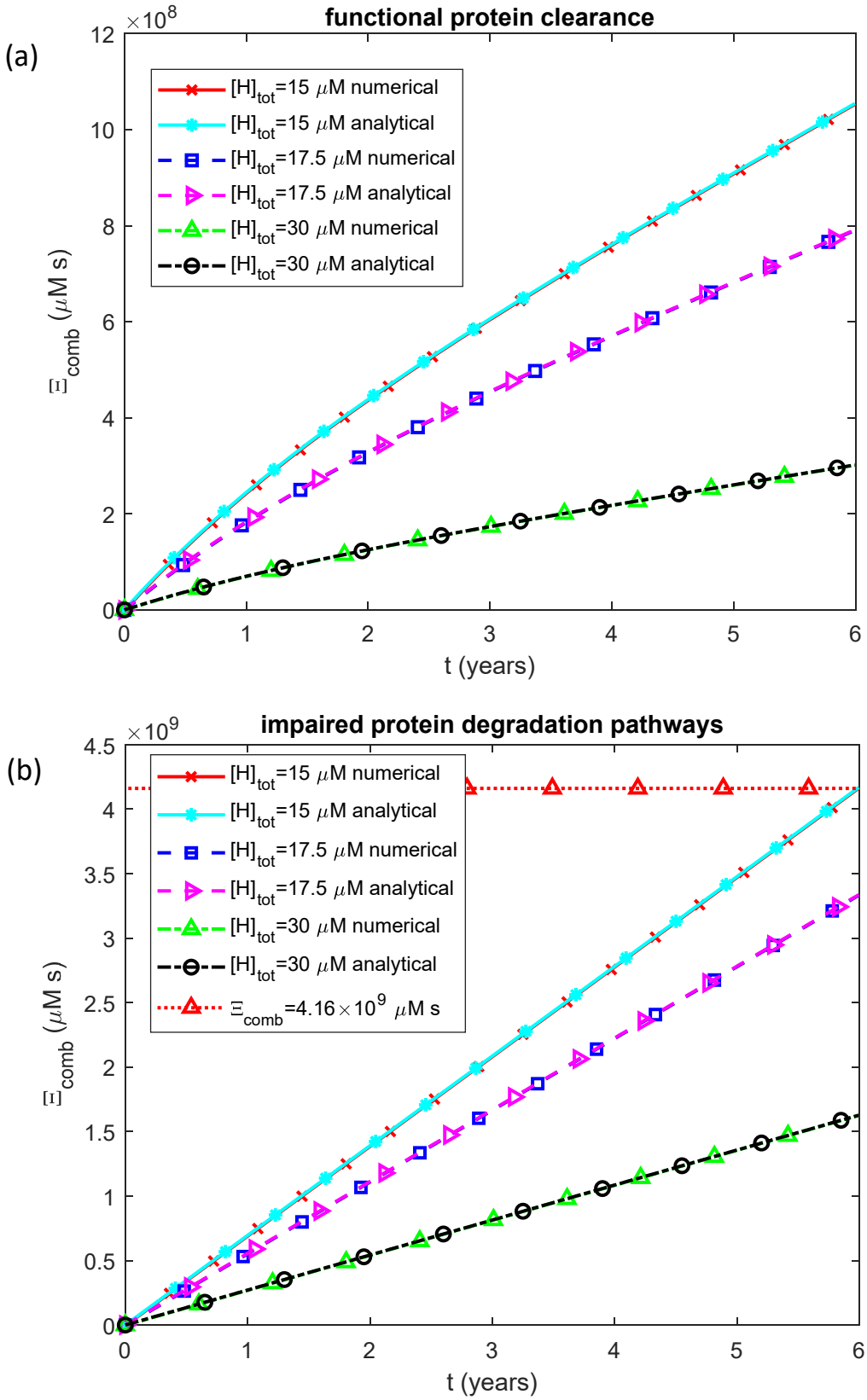
(a)
functional protein clearance
×10^8
[H]tot=15 μM numerical
[H]tot=15 μM analytical
[H]tot=17.5 μM numerical
[H]tot=17.5 μM analytical
[H]tot=30 μM numerical
[H]tot=30 μM analytical
Ξcomb (μM s)
t (years)
(b)
impaired protein degradation pathways
×10^9
Ξcomb=4.16×10^9 μM s

Figure 2

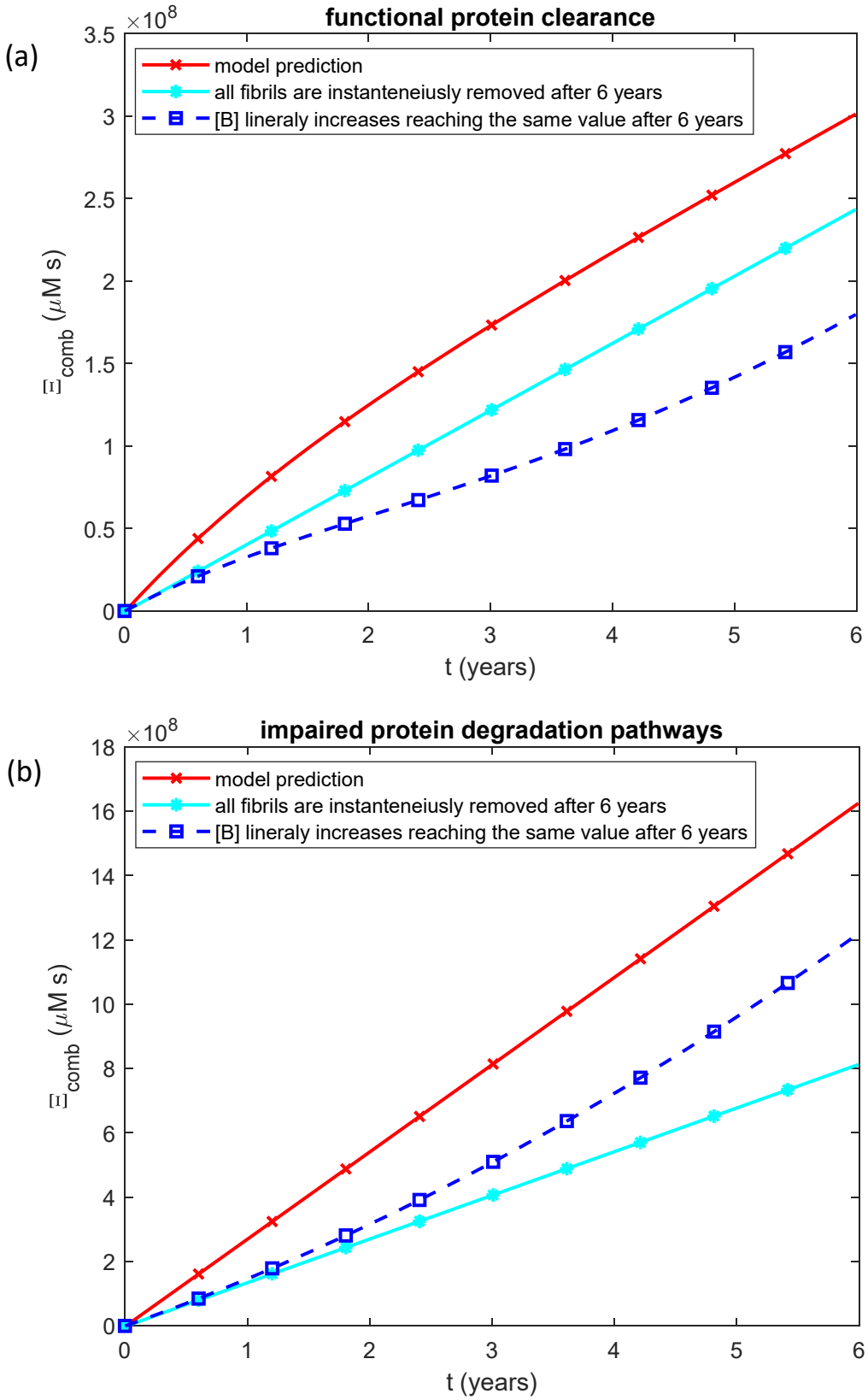
(a)
functional protein clearance
×10^8
model prediction
all fibrils are instanteneiusly removed after 6 years
[B] lineraly increases reaching the same value after 6 years
[I]comb (μM s)
t (years)
(b)
impaired protein degradation pathways
×10^8
model prediction
all fibrils are instanteneiusly removed after 6 years
[B] lineraly increases reaching the same value after 6 years
[I]comb (μM s)
t (years)

Figure 3

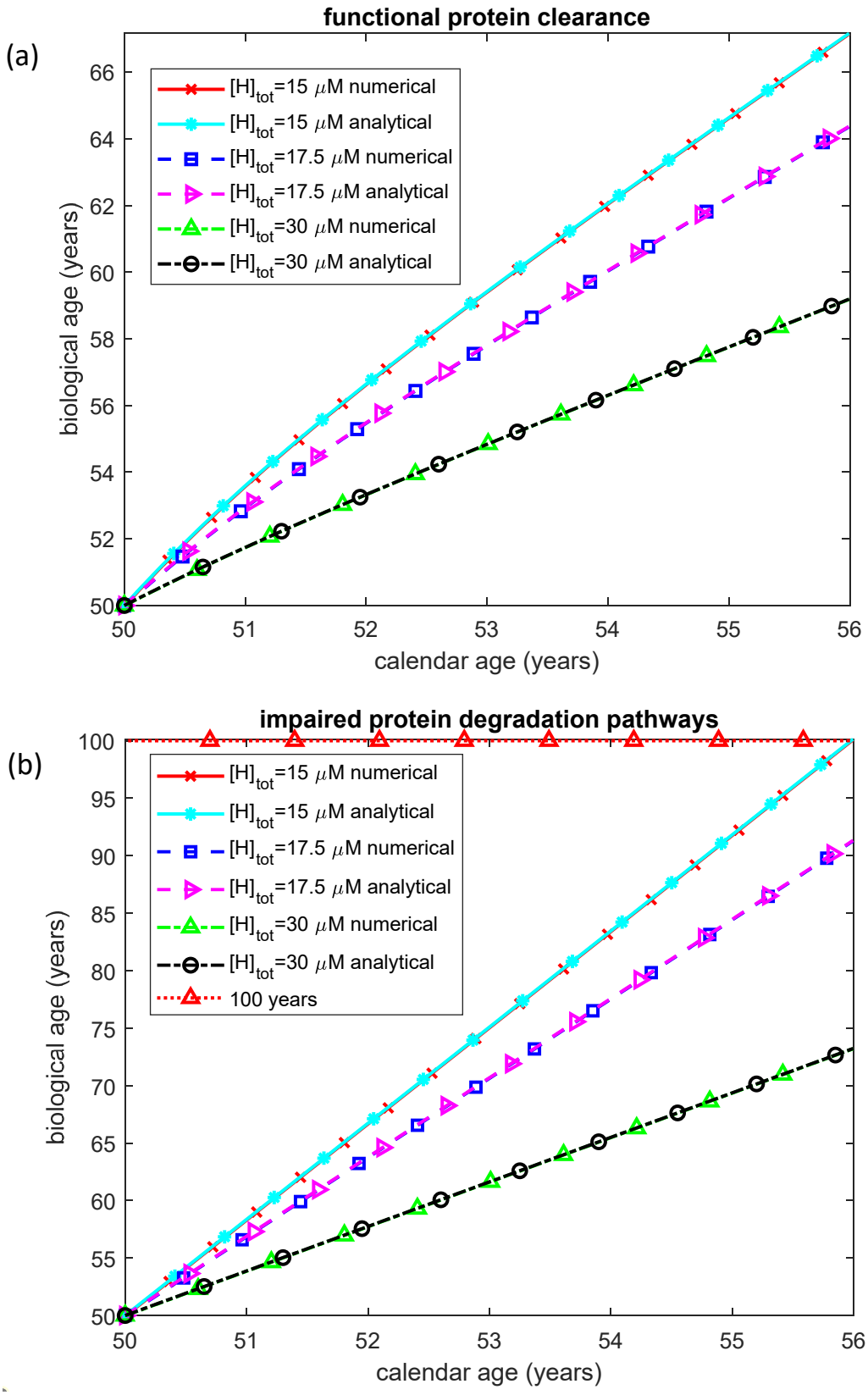
(a)
functional protein clearance
[H]tot=15 μM numerical
[H]tot=15 μM analytical
[H]tot=17.5 μM numerical
[H]tot=17.5 μM analytical
[H]tot=30 μM numerical
[H]tot=30 μM analytical
biological age (years)
calendar age (years)
(b)
impaired protein degradation pathways
[H]tot=15 μM numerical
[H]tot=15 μM analytical
[H]tot=17.5 μM numerical
[H]tot=17.5 μM analytical
[H]tot=30 μM numerical
[H]tot=30 μM analytical
100 years
biological age (years)
calendar age (years)

Figure 4

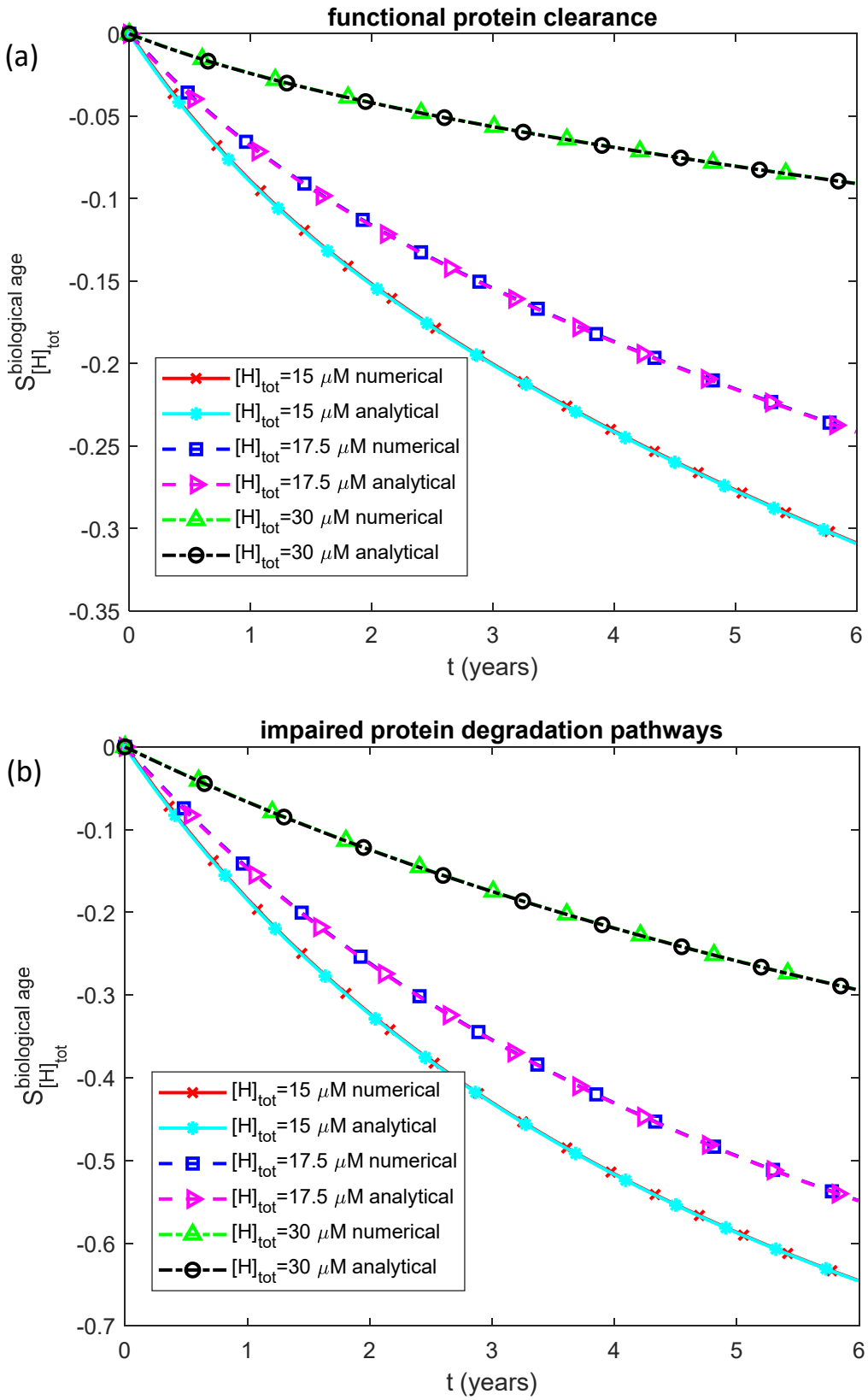
(a)
functional protein clearance
$S^{biological\ age}_{[H]_{tot}}$
t (years)
[H]tot=15 μM numerical
[H]tot=15 μM analytical
[H]tot=17.5 μM numerical
[H]tot=17.5 μM analytical
[H]tot=30 μM numerical
[H]tot=30 μM analytical
(b)
impaired protein degradation pathways
$S^{biological\ age}_{[H]_{tot}}$
t (years)
[H]tot=15 μM numerical
[H]tot=15 μM analytical
[H]tot=17.5 μM numerical
[H]tot=17.5 μM analytical
[H]tot=30 μM numerical
[H]tot=30 μM analytical

Figure 5

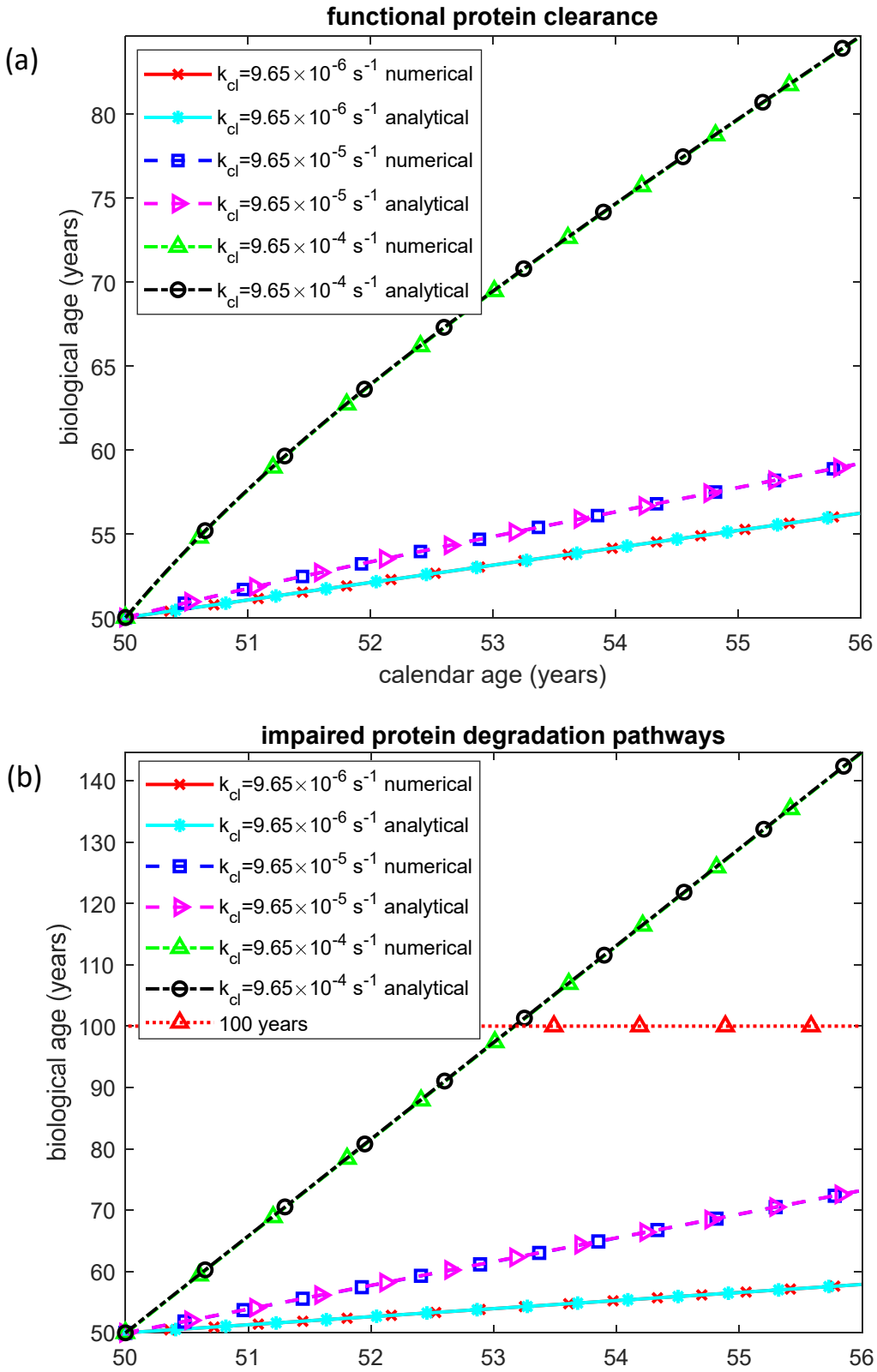
(a)
functional protein clearance
k_{cl}=9.65×10^{-6} s^{-1} numerical
k_{cl}=9.65×10^{-6} s^{-1} analytical
k_{cl}=9.65×10^{-5} s^{-1} numerical
k_{cl}=9.65×10^{-5} s^{-1} analytical
k_{cl}=9.65×10^{-4} s^{-1} numerical
k_{cl}=9.65×10^{-4} s^{-1} analytical
biological age (years)
calendar age (years)
(b)
impaired protein degradation pathways
k_{cl}=9.65×10^{-6} s^{-1} numerical
k_{cl}=9.65×10^{-6} s^{-1} analytical
k_{cl}=9.65×10^{-5} s^{-1} numerical
k_{cl}=9.65×10^{-5} s^{-1} analytical
k_{cl}=9.65×10^{-4} s^{-1} numerical
k_{cl}=9.65×10^{-4} s^{-1} analytical
100 years
biological age (years)

Figure 6

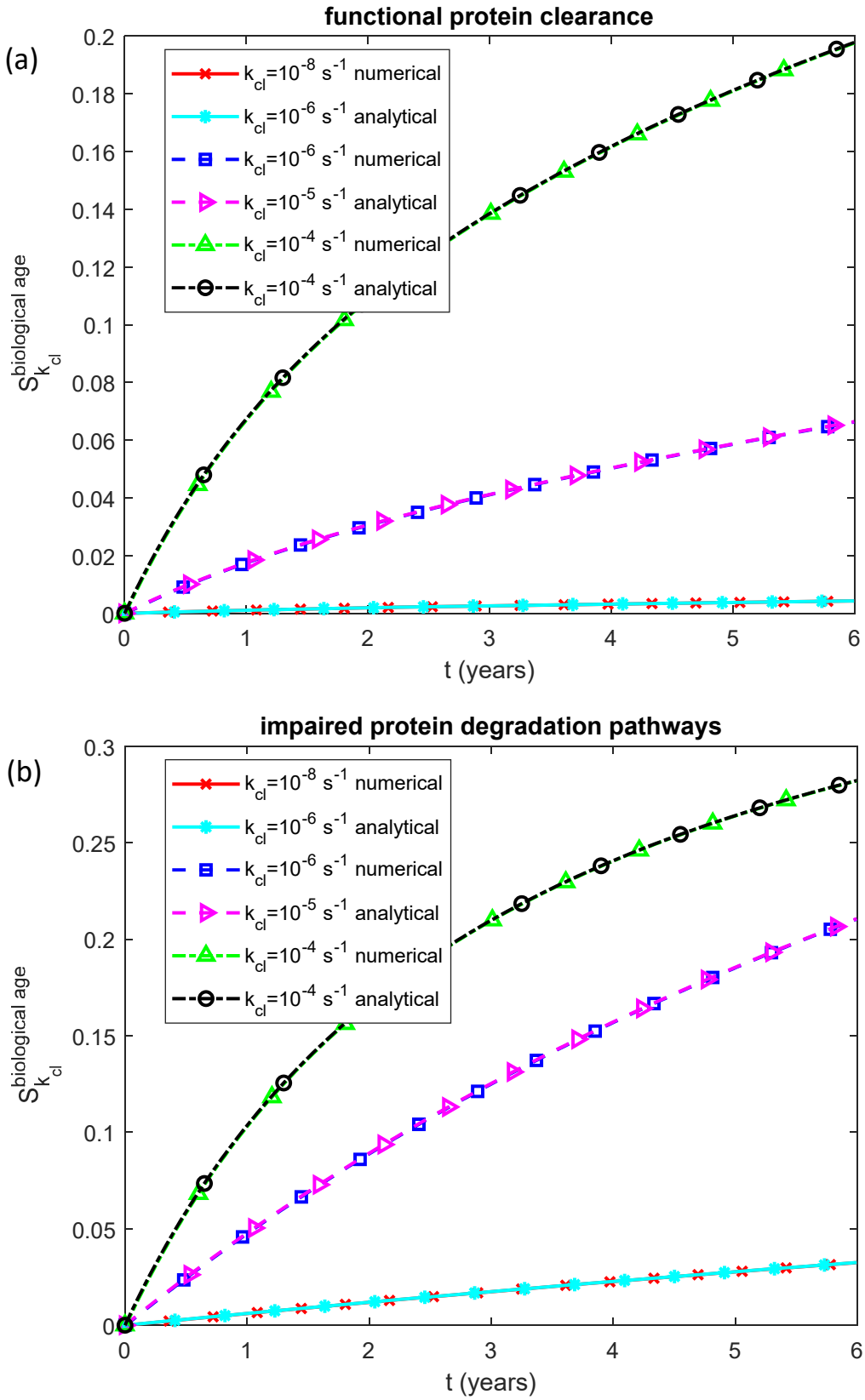
functional protein clearance
(a)
$k_{cl}=10^{-8}$ s^{-1} numerical
$k_{cl}=10^{-6}$ s^{-1} analytical
$k_{cl}=10^{-6}$ s^{-1} numerical
$k_{cl}=10^{-5}$ s^{-1} analytical
$k_{cl}=10^{-4}$ s^{-1} numerical
$k_{cl}=10^{-4}$ s^{-1} analytical
$S^{biological\ age}_{k_{cl}}$
t (years)
impaired protein degradation pathways
(b)
$k_{cl}=10^{-8}$ s^{-1} numerical
$k_{cl}=10^{-6}$ s^{-1} analytical
$k_{cl}=10^{-6}$ s^{-1} numerical
$k_{cl}=10^{-5}$ s^{-1} analytical
$k_{cl}=10^{-4}$ s^{-1} numerical
$k_{cl}=10^{-4}$ s^{-1} analytical
$S^{biological\ age}_{k_{cl}}$
t (years)

Figure 7

Mathematical Modeling of AA Amyloidosis: Coupling SAA-HDL Binding Dynamics with Path-Dependent Renal Aging

Andrey V Kuznetsov

Department of Mechanical and Aerospace Engineering, North Carolina State University,

Raleigh, NC 27695-7910, USA; e-mail: avkuznet@ncsu.edu

Supplemental Materials

S1. Numerical solution

To solve the system of ordinary differential equations (15), (19), (20), and (26) with the prescribed initial condition (32), MATLAB's ODE45 solver (R2024a, MathWorks, Natick, MA, USA) was employed. This numerical integrator implements an adaptive step-size Runge–Kutta method, making it well-suited for problems requiring both high accuracy and reasonable computational cost. The solver was configured with stringent tolerances, setting both relative and absolute error thresholds to 1e-10, to guarantee the numerical solutions met the precision requirements.

S2. Supplementary figures

(a)

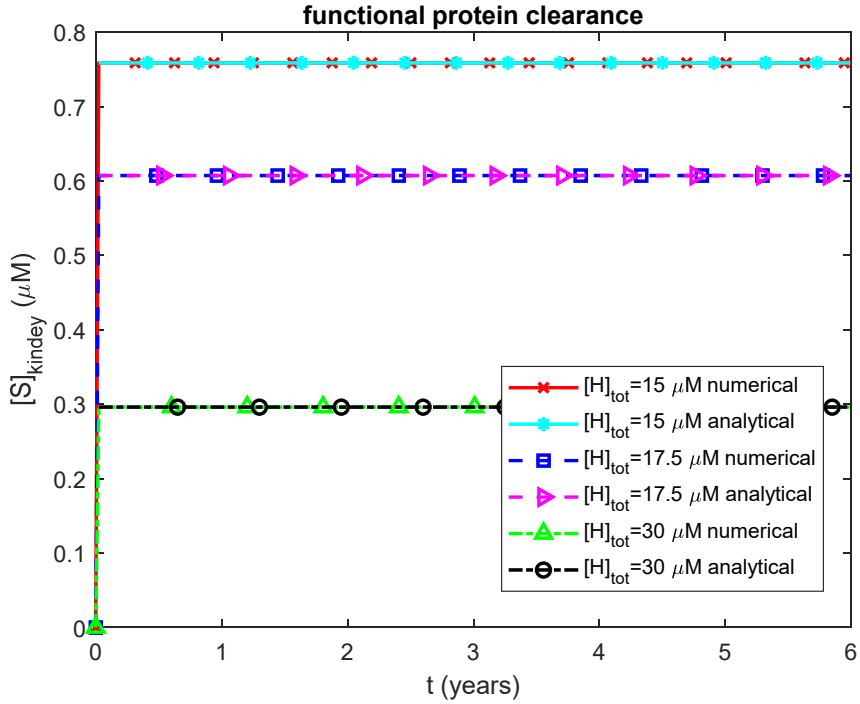

(b)

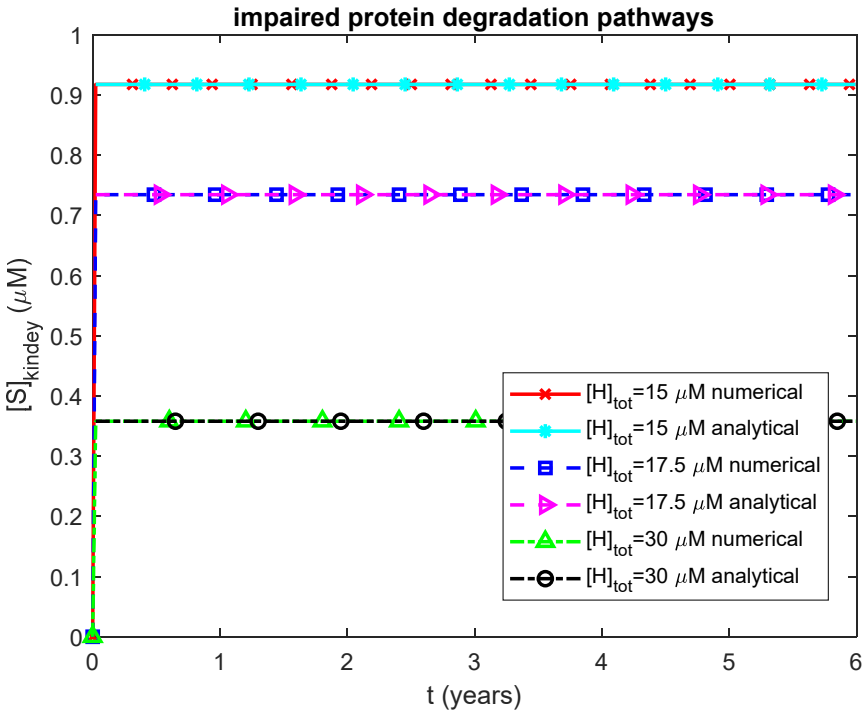

Fig. S1. Molar concentration of SAA in the kidneys as a function of time. (a) Biologically relevant half-lives $T_{1/2,A}$, $T_{1/2,B}$, $T_{1/2,I}$, and $T_{1/2,S}$, representing functional protein degradation machinery. (b) Infinite half-lives $T_{1/2,A}$, $T_{1/2,B}$, $T_{1/2,I}$, and $T_{1/2,S}$, representing complete impairment of protein degradation. Each

panel shows results for three values of the total number of SAA binding sites on HDL particles in plasma. Baseline parameters: $k_1 = 10^{-4}$ s^{-1}, $k_2 = 10^{-4}$ μM^{-1} s^{-1}, $k_{cl} = 9.65 \times 10^{-5}$ s^{-1}, $K_d = 1.1789$ μM, $h_S = 5.55 \times 10^{-7}$ m s^{-1}, $S_{tot} = 8$ μM, and $\theta_{1/2,B} = 8.64 \times 10^4$ s; remaining parameters as listed in Table 2.

(a)

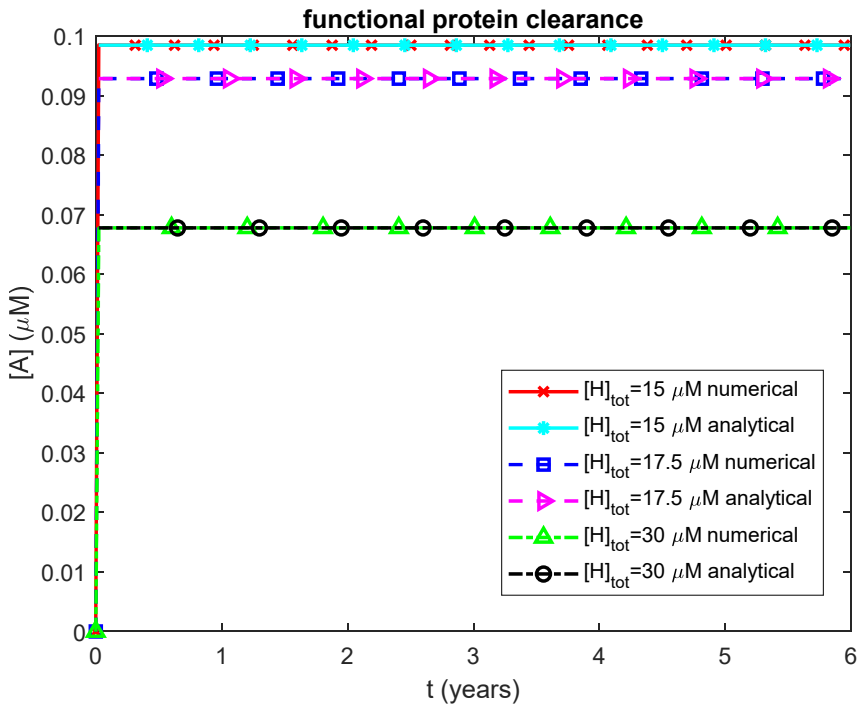

(b)

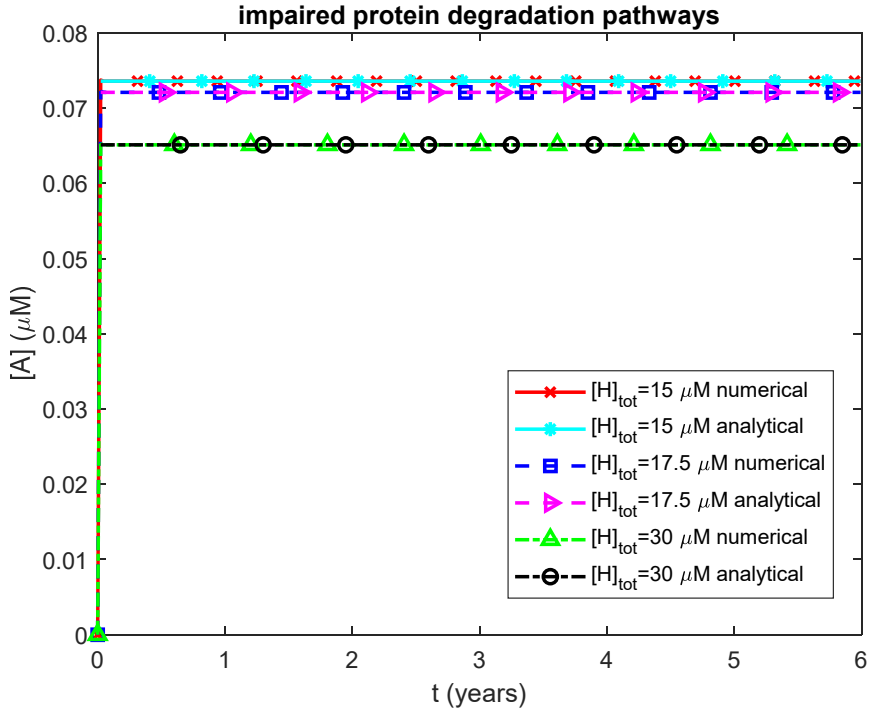

Fig. S2. Molar concentration of AA fragments (monomers) in kidneys as a function of time. (a) Biologically relevant half-lives $T_{1/2,A}$, $T_{1/2,B}$, $T_{1/2,I}$, and $T_{1/2,S}$, representing functional protein degradation machinery. (b) Infinite half-lives $T_{1/2,A}$, $T_{1/2,B}$, $T_{1/2,I}$, and $T_{1/2,S}$, representing complete impairment of protein degradation. Each panel shows results for three values of the total number of SAA binding sites on HDL particles in plasma. Baseline parameters: $k_1 = 10^{-4}$ s^{-1}, $k_2 = 10^{-4}$ μM^{-1} s^{-1}, $k_{cl} = 9.65 \times 10^{-5}$ s^{-1}, $K_d = 1.1789$ μM, $h_S = 5.55 \times 10^{-7}$ m s^{-1}, $S_{tot} = 8$ μM, and $\theta_{1/2,B} = 8.64 \times 10^4$ s; remaining parameters as listed in Table 2.

(a)

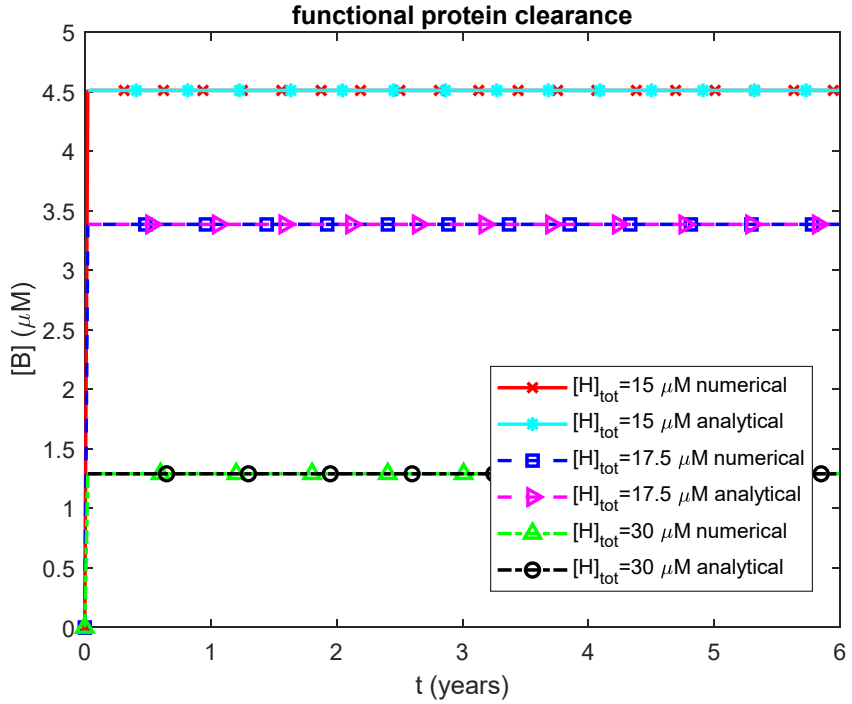

(b)

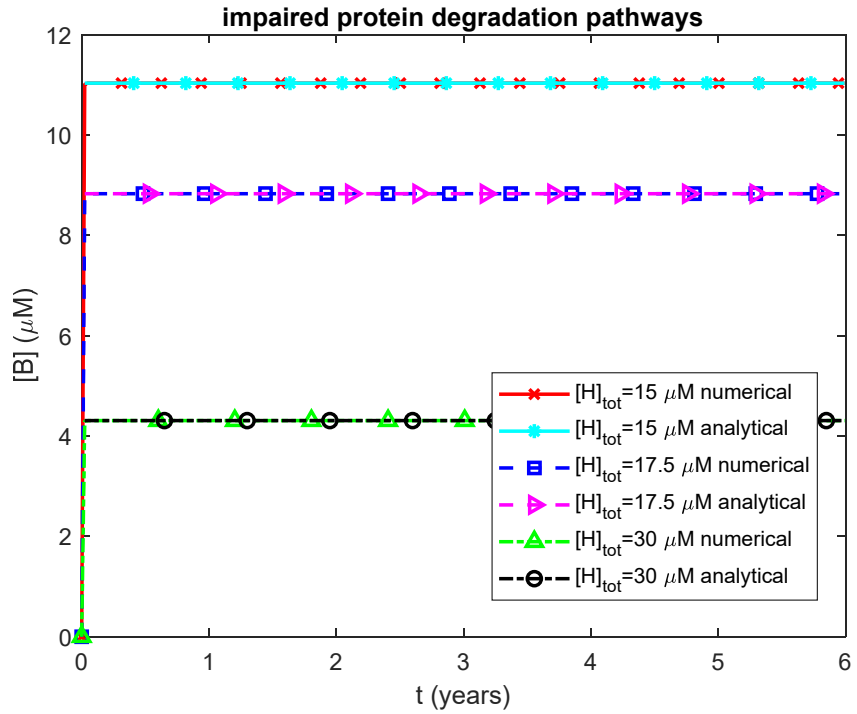

Fig. S3. Molar concentration of free (not deposited in fibrils) AA oligomers in kidneys as a function of time. (a) Biologically relevant half-lives $T_{1/2,A}$, $T_{1/2,B}$, $T_{1/2,I}$, and $T_{1/2,S}$, representing functional protein degradation machinery. (b) Infinite half-lives $T_{1/2,A}$, $T_{1/2,B}$, $T_{1/2,I}$, and $T_{1/2,S}$, representing complete

impairment of protein degradation. Each panel shows results for three values of the total number of SAA binding sites on HDL particles in plasma. Baseline parameters: $k_1 = 10^{-4}$ s^{-1}, $k_2 = 10^{-4}$ μM^{-1} s^{-1}, $k_{cl} = 9.65 \times 10^{-5}$ s^{-1}, $K_d = 1.1789$ μM, $h_S = 5.55 \times 10^{-7}$ m s^{-1}, $S_{tot} = 8$ μM, and $\theta_{1/2,B} = 8.64 \times 10^4$ s; remaining parameters as listed in Table 2.

(a)

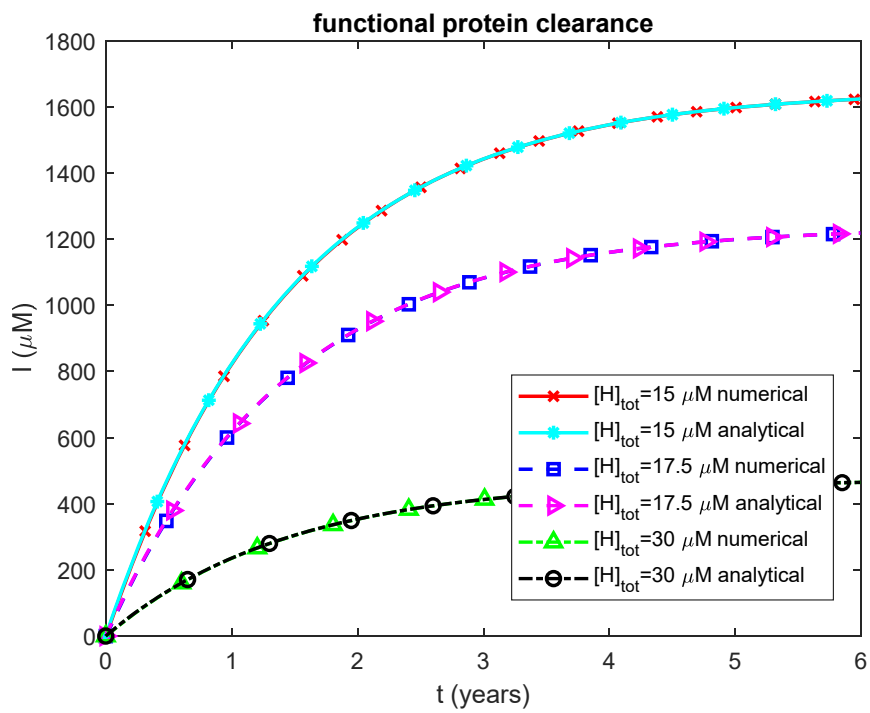

(b)

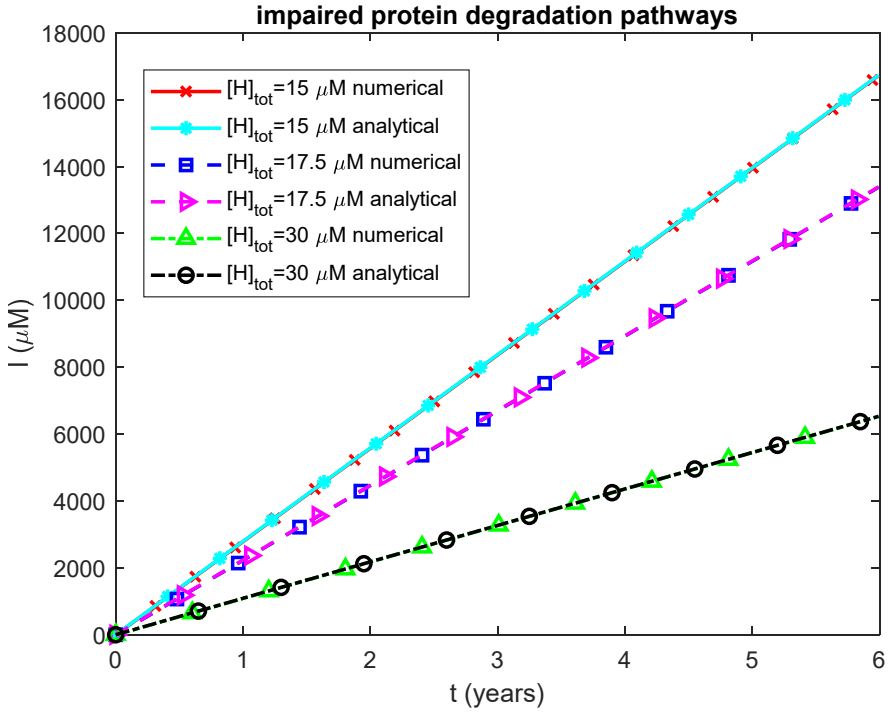

Fig. S4. Molar concentration of AA oligomers deposited into AA amyloid fibrils in kidneys as a function of time. (a) Biologically relevant half-lives $T_{1/2,A}$, $T_{1/2,B}$, $T_{1/2,I}$, and $T_{1/2,S}$, representing functional protein degradation machinery. (b) Infinite half-lives $T_{1/2,A}$, $T_{1/2,B}$, $T_{1/2,I}$, and $T_{1/2,S}$, representing complete impairment of protein degradation. Each panel shows results for three values of the total number of SAA binding sites on HDL particles in plasma. Baseline parameters: $k_1 = 10^{-4}$ s^{-1}, $k_2 = 10^{-4}$ μM^{-1} s^{-1}, $k_{cl} = 9.65\times10^{-5}$ s^{-1}, $K_d = 1.1789$ μM, $h_S = 5.55\times10^{-7}$ m s^{-1}, $S_{tot} = 8$ μM, and $\theta_{1/2,B} = 8.64\times10^{4}$ s; remaining parameters as listed in Table 2.

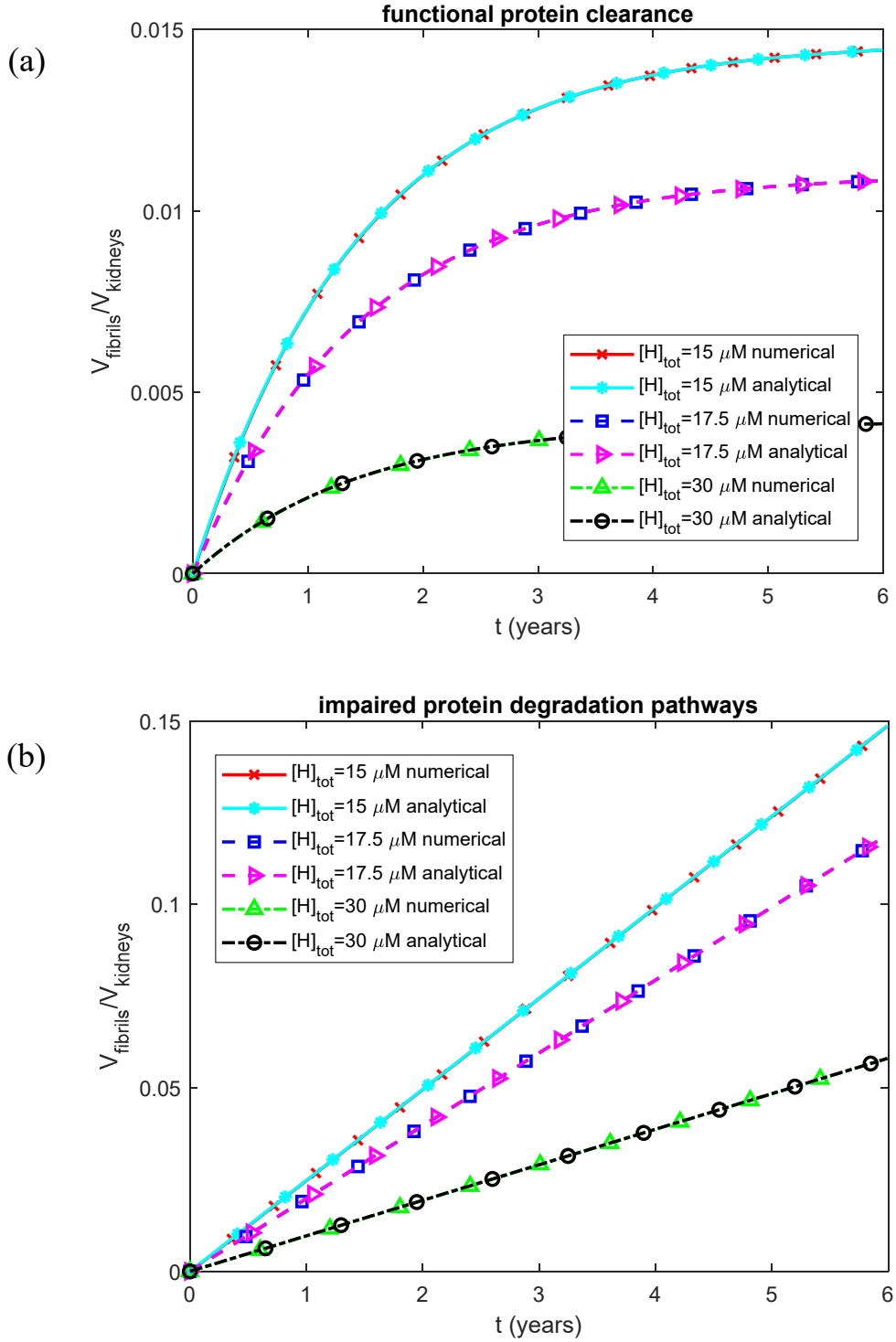

Fig. S5. Fraction of the baseline kidney volume occupied by fibrils as a function of time. (a) Biologically relevant half-lives $T_{1/2,A}$, $T_{1/2,B}$, $T_{1/2,I}$, and $T_{1/2,S}$, representing functional protein degradation machinery. (b) Infinite half-lives $T_{1/2,A}$, $T_{1/2,B}$, $T_{1/2,I}$, and $T_{1/2,S}$, representing complete impairment of protein

degradation. Each panel shows results for three values of the total number of SAA binding sites on HDL particles in plasma. Baseline parameters: $k_1 = 10^{-4}$ s^{-1}, $k_2 = 10^{-4}$ μM^{-1} s^{-1}, $k_{cl} = 9.65 \times 10^{-5}$ s^{-1}, $K_d = 1.1789$ μM, $h_S = 5.55 \times 10^{-7}$ m s^{-1}, $S_{tot} = 8$ μM, and $\theta_{1/2,B} = 8.64 \times 10^4$ s; remaining parameters as listed in Table 2.

(a)

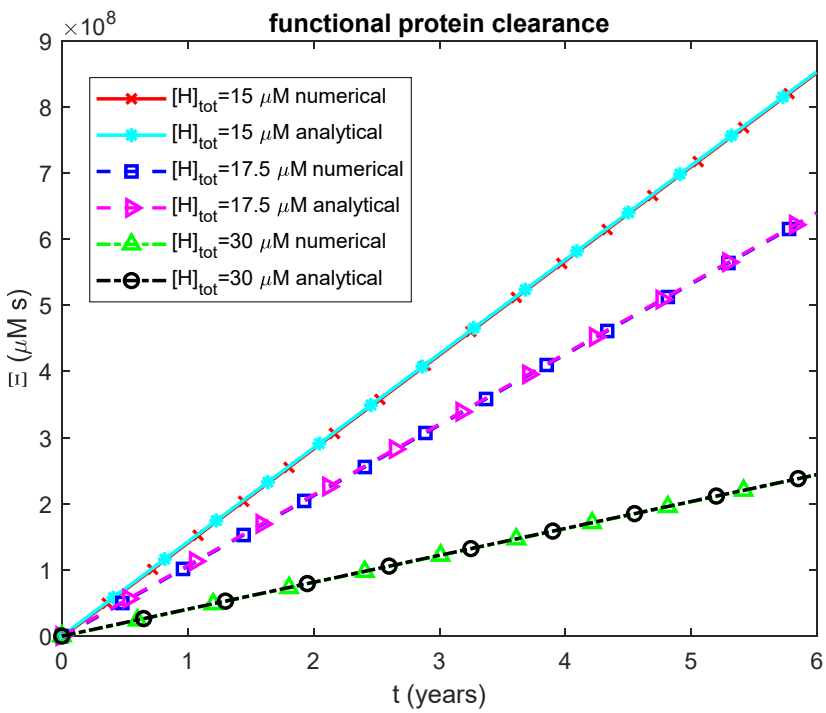

(b)

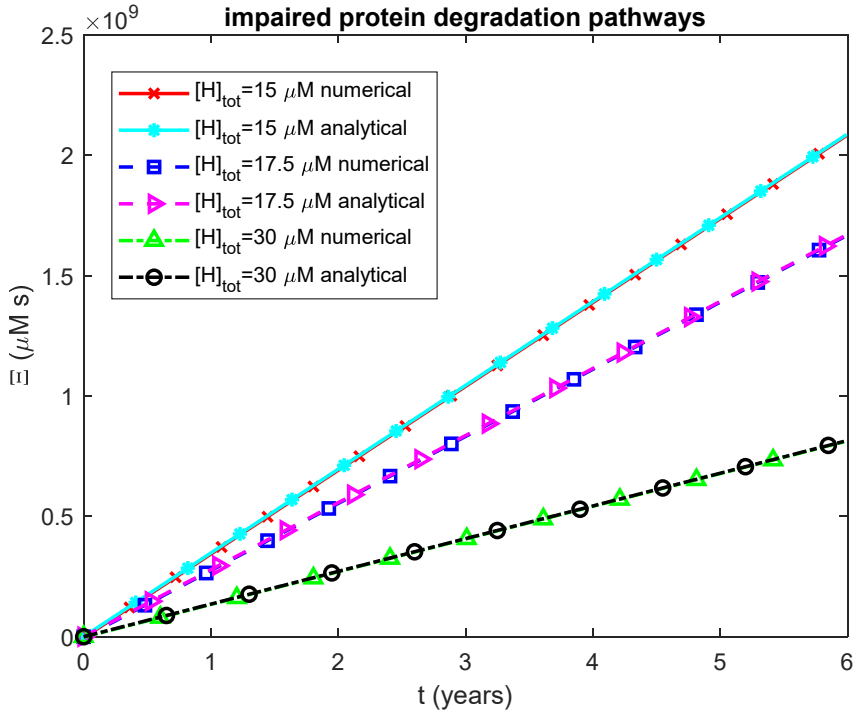

Fig. S6. Accumulated nephrotoxicity of AA oligomers as a function of time. (a) Biologically relevant half-lives $T_{1/2,A}$, $T_{1/2,B}$, $T_{1/2,I}$, and $T_{1/2,S}$, representing functional protein degradation machinery. (b) Infinite half-lives $T_{1/2,A}$, $T_{1/2,B}$, $T_{1/2,I}$, and $T_{1/2,S}$, representing complete impairment of protein degradation. Each panel shows results for three values of the total number of SAA binding sites on HDL particles in plasma. Baseline parameters: $k_1 = 10^{-4}$ s^{-1}, $k_2 = 10^{-4}$ μM^{-1} s^{-1}, $k_{cl} = 9.65\times10^{-5}$ s^{-1}, $K_d = 1.1789$ μM, $h_S = 5.55\times10^{-7}$ m s^{-1}, $S_{tot} = 8$ μM, and $\theta_{1/2,B} = 8.64\times10^{4}$ s; remaining parameters as listed in Table 2.

(a)

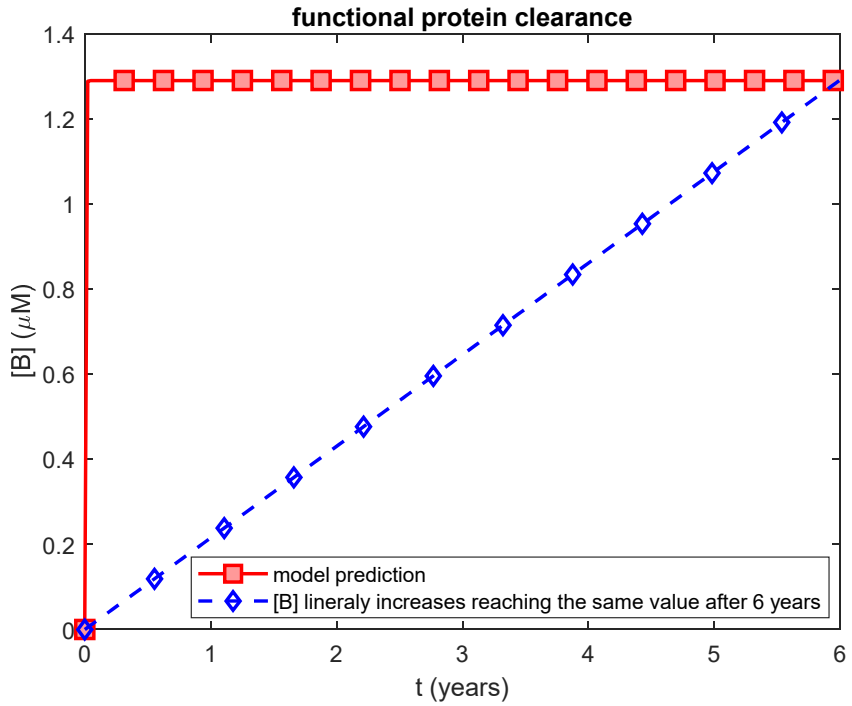

(b)

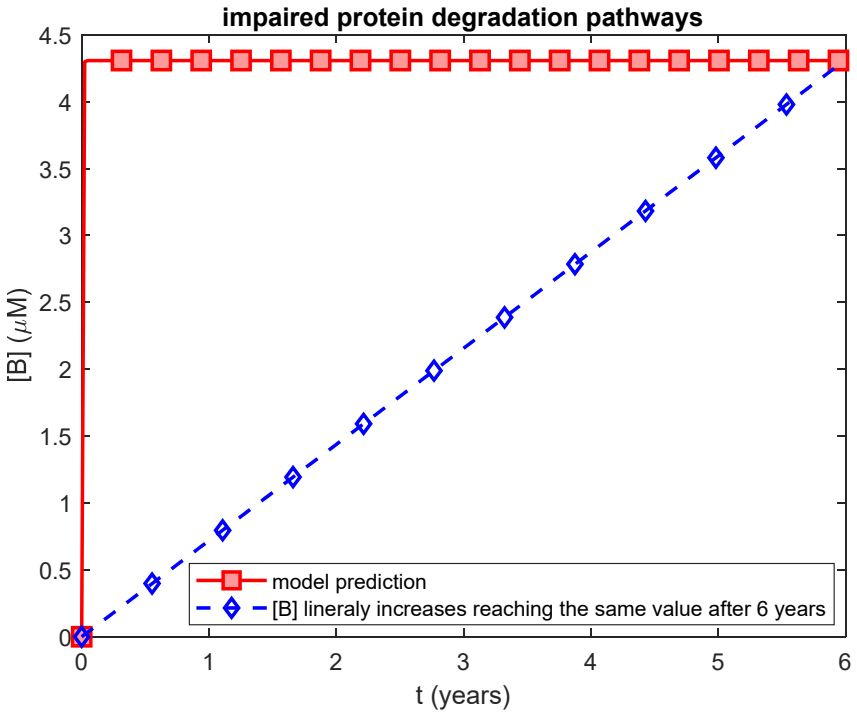

Fig. S7. Molar concentration of free (non-fibrillar) AA oligomers in the kidneys as a function of time. Two cases are compared: the model prediction, in which $[B]$ attains a constant steady-state early in the

disease course, and a hypothetical scenario in which $[B]$ increases linearly throughout disease progression. (a) Biologically relevant half-lives $T_{1/2,A}$, $T_{1/2,B}$, $T_{1/2,I}$, and $T_{1/2,S}$, representing functional protein degradation machinery. (b) Infinite half-lives $T_{1/2,A}$, $T_{1/2,B}$, $T_{1/2,I}$, and $T_{1/2,S}$, representing complete impairment of protein degradation. Baseline parameters: $k_1 = 10^{-4}$ s^{-1}, $k_2 = 10^{-4}$ μM^{-1} s^{-1}, $k_{cl} = 9.65 \times 10^{-5}$ s^{-1}, $K_d = 1.1789$ μM, $h_S = 5.55 \times 10^{-7}$ m s^{-1}, $H_{tot} = 30$ μM, $S_{tot} = 8$ μM, and $\theta_{1/2,B} = 8.64 \times 10^4$ s; remaining parameters as listed in Table 2.

(a)

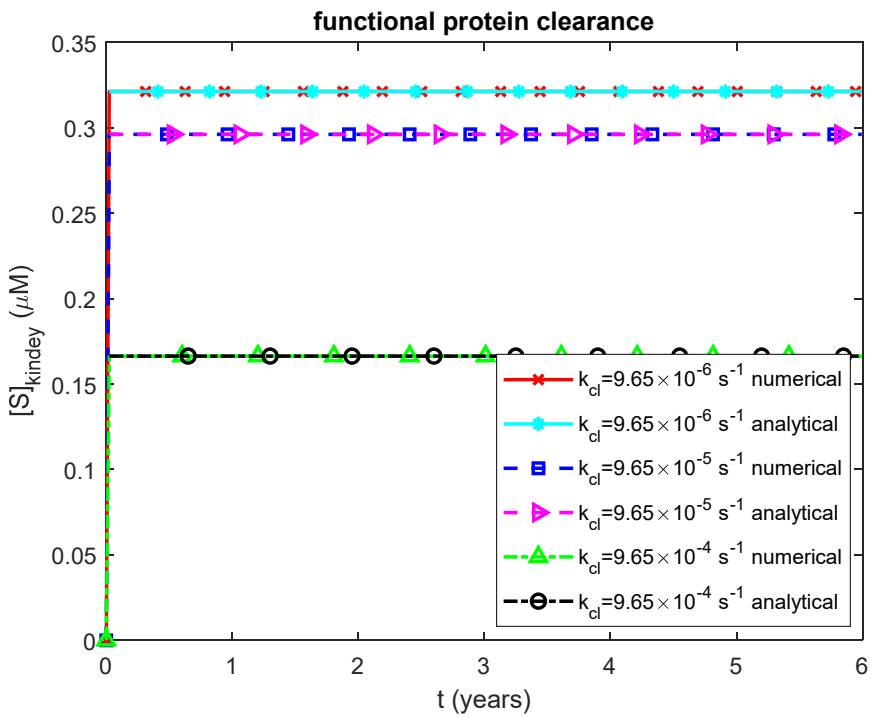

(b)

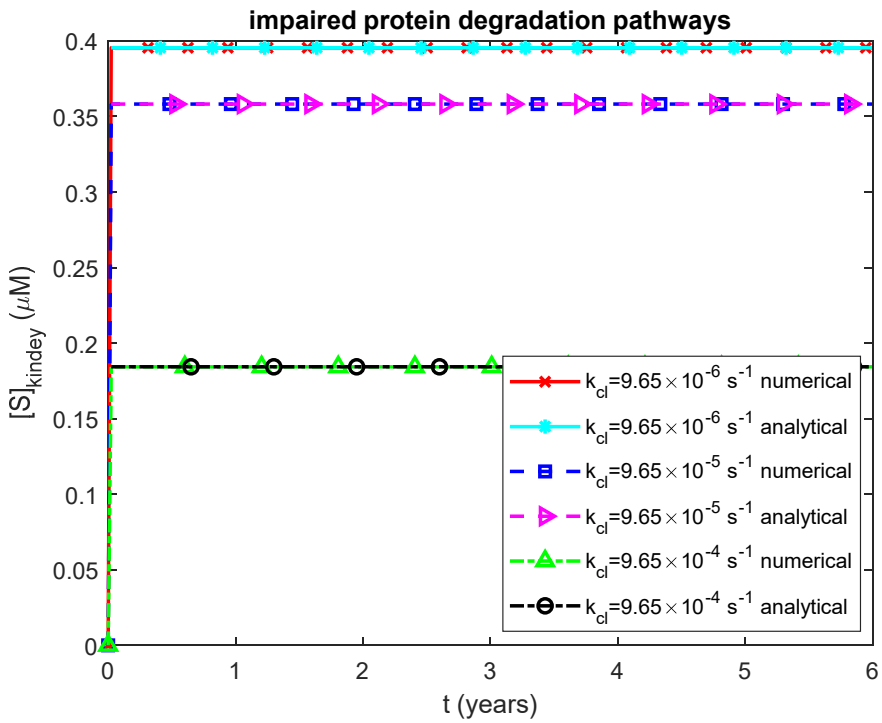

Fig. S8. Molar concentration of SAA in the kidneys as a function of time. (a) Biologically relevant half-lives $T_{1/2,A}$, $T_{1/2,B}$, $T_{1/2,I}$, and $T_{1/2,S}$, representing functional protein degradation machinery. (b) Infinite half-lives $T_{1/2,A}$, $T_{1/2,B}$, $T_{1/2,I}$, and $T_{1/2,S}$, representing complete impairment of protein degradation. Each panel shows results for three values of the rate constant for proteolytic cleavage of SAA that generates AA monomers. Baseline parameters: $k_1 = 10^{-4}$ s^{-1}, $k_2 = 10^{-4}$ μM^{-1} s^{-1}, $K_d = 1.1789$ μM, $h_S = 5.55 \times 10^{-7}$ m s^{-1}, $H_{tot} = 30$ μM, $S_{tot} = 8$ μM, and $\theta_{1/2,B} = 8.64 \times 10^4$ s; remaining parameters as listed in Table 2.

(a)

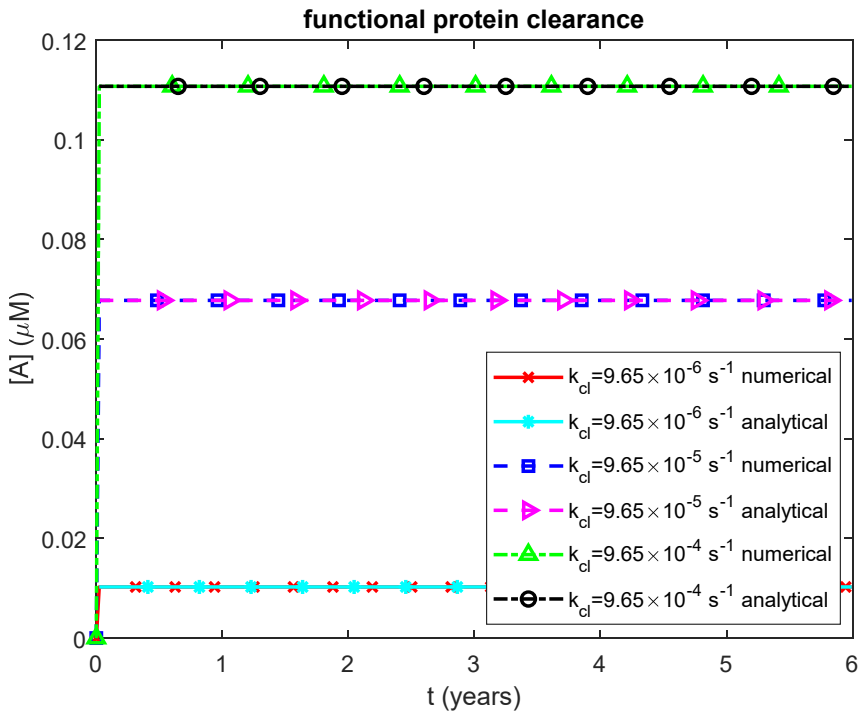

(b)

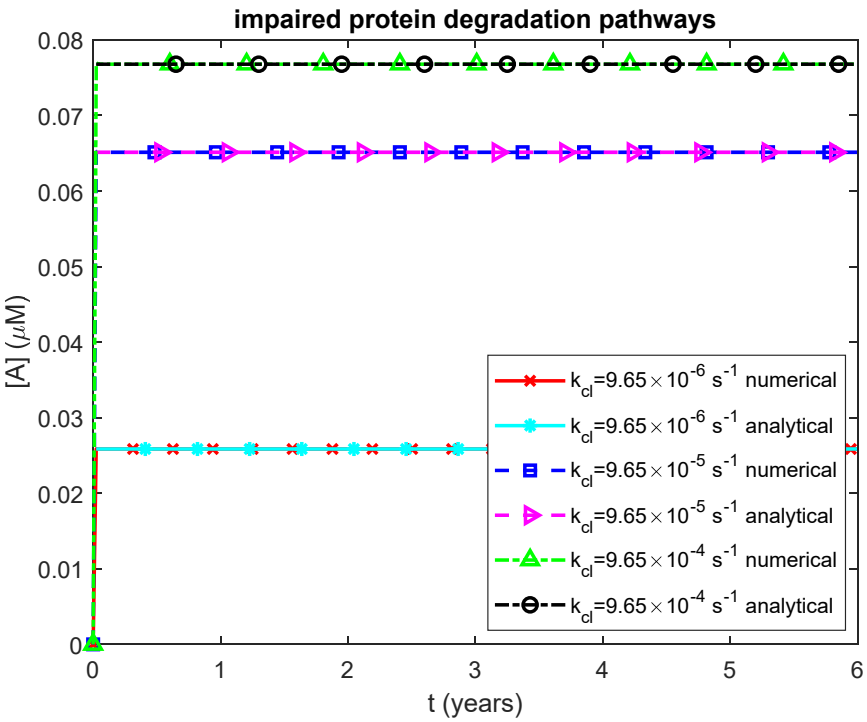

Fig. S9. Molar concentration of AA fragments (monomers) in kidneys as a function of time. (a) Biologically relevant half-lives $T_{1/2,A}$, $T_{1/2,B}$, $T_{1/2,I}$, and $T_{1/2,S}$, representing functional protein degradation machinery. (b) Infinite half-lives $T_{1/2,A}$, $T_{1/2,B}$, $T_{1/2,I}$, and $T_{1/2,S}$, representing complete impairment of

protein degradation. Each panel shows results for three values of the rate constant for proteolytic cleavage of SAA that generates AA monomers. Baseline parameters: $k_1 = 10^{-4}$ s^{-1}, $k_2 = 10^{-4}$ μM^{-1} s^{-1}, $K_d = 1.1789$ μM, $h_S = 5.55 \times 10^{-7}$ m s^{-1}, $H_{tot} = 30$ μM, $S_{tot} = 8$ μM, and $\theta_{1/2,B} = 8.64 \times 10^4$ s; remaining parameters as listed in Table 2.

(a)

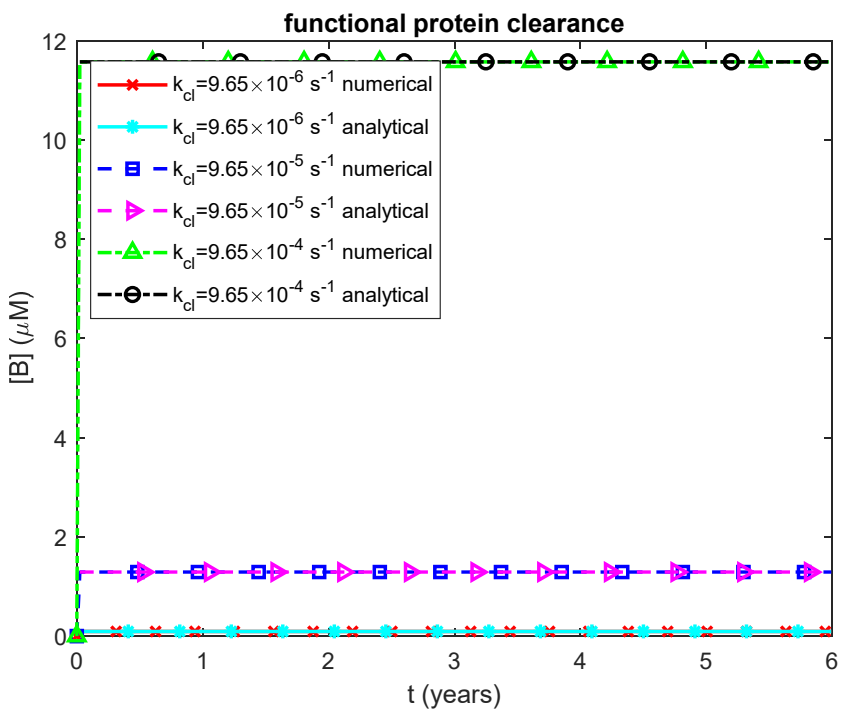

(b)

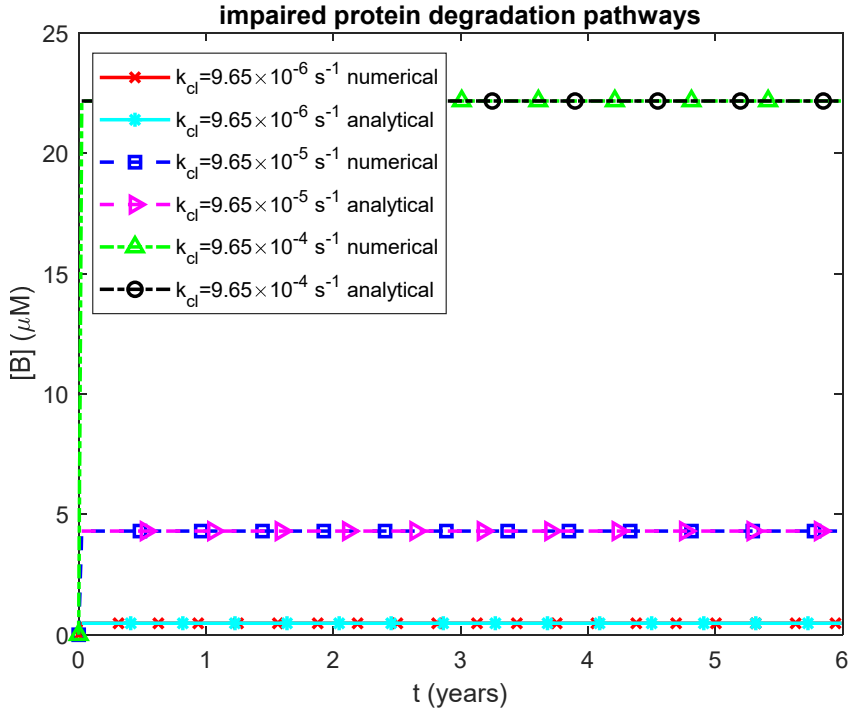

Fig. S10. Molar concentration of free (non-fibrillar) AA oligomers in the kidneys as a function of time. (a) Biologically relevant half-lives $T_{1/2,A}$, $T_{1/2,B}$, $T_{1/2,I}$, and $T_{1/2,S}$, representing functional protein degradation machinery. (b) Infinite half-lives $T_{1/2,A}$, $T_{1/2,B}$, $T_{1/2,I}$, and $T_{1/2,S}$, representing complete impairment of protein degradation. Each panel shows results for three values of the rate constant for proteolytic cleavage of SAA that generates AA monomers. Baseline parameters: $k_1 = 10^{-4}$ s^{-1}, $k_2 = 10^{-4}$ μM^{-1} s^{-1}, $K_d = 1.1789$ μM, $h_S = 5.55 \times 10^{-7}$ m s^{-1}, $H_{tot} = 30$ μM, $S_{tot} = 8$ μM, and $\theta_{1/2,B} = 8.64 \times 10^4$ s; remaining parameters as listed in Table 2.

(a)

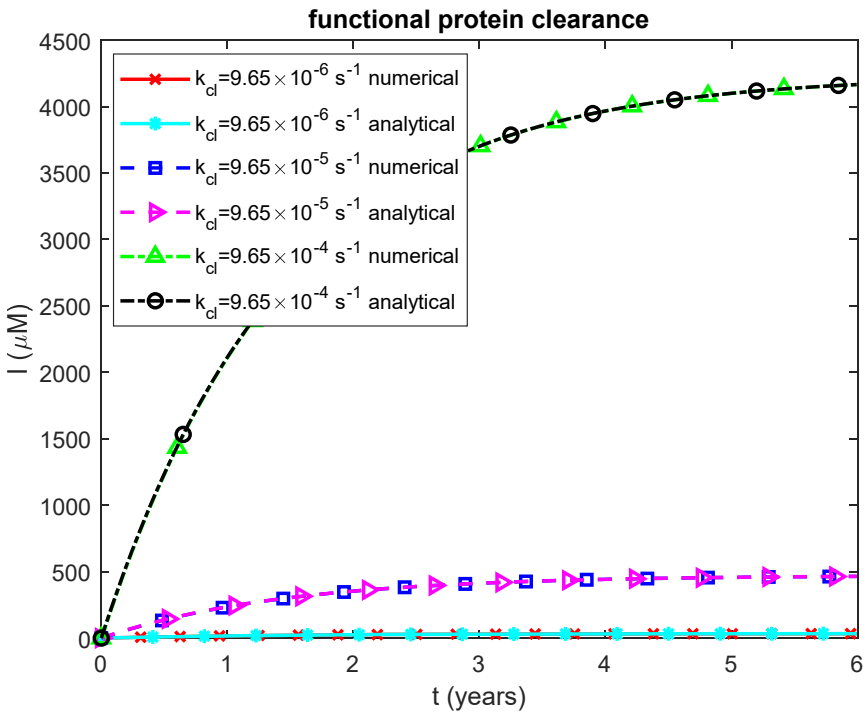

(b)

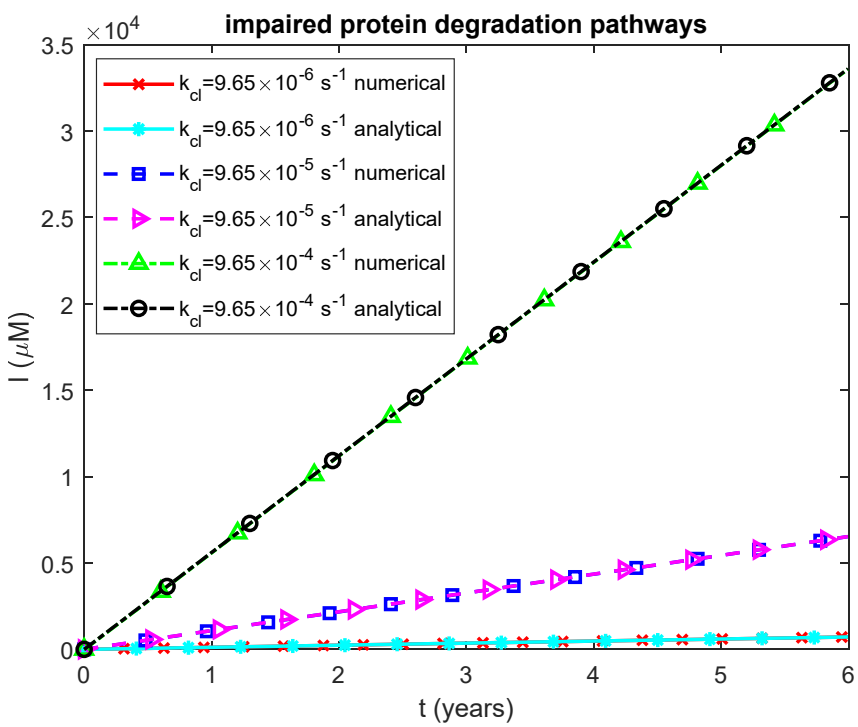

Fig. S11. Molar concentration of AA oligomers deposited into AA amyloid fibrils in kidneys as a function of time. (a) Biologically relevant half-lives $T_{1/2,A}$, $T_{1/2,B}$, $T_{1/2,I}$, and $T_{1/2,S}$, representing functional protein degradation machinery. (b) Infinite half-lives $T_{1/2,A}$, $T_{1/2,B}$, $T_{1/2,I}$, and $T_{1/2,S}$, representing complete

impairment of protein degradation. Each panel shows results for three values of the rate constant for proteolytic cleavage of SAA that generates AA monomers. Baseline parameters: $k_1 = 10^{-4}$ s^{-1}, $k_2 = 10^{-4}$ μM^{-1} s^{-1}, $K_d = 1.1789$ μM, $h_S = 5.55 \times 10^{-7}$ m s^{-1}, $H_{tot} = 30$ μM, $S_{tot} = 8$ μM, and $\theta_{1/2,B} = 8.64 \times 10^4$ s; remaining parameters as listed in Table 2.

(a)

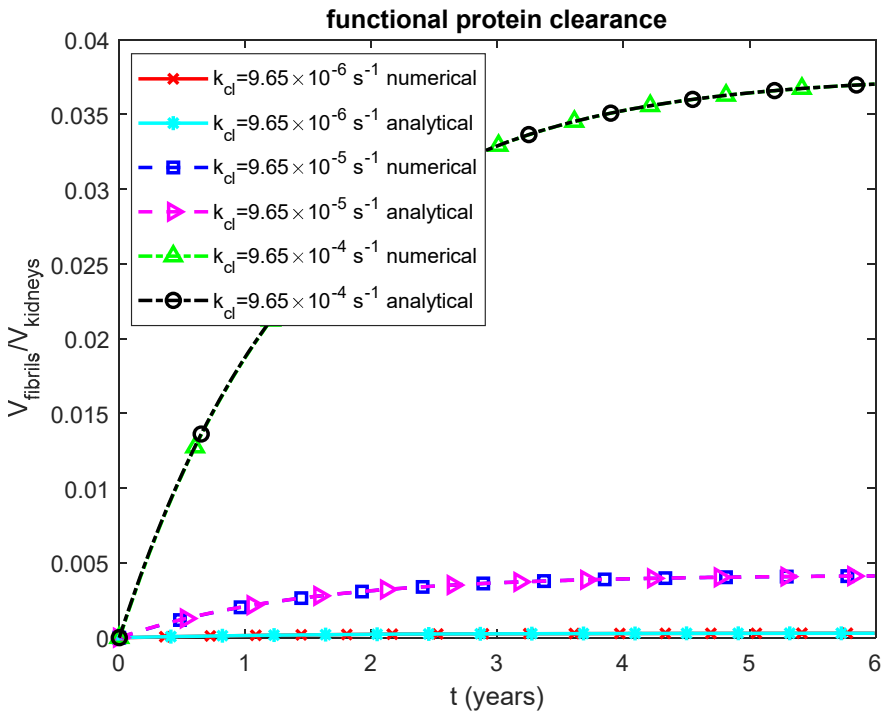

(b)

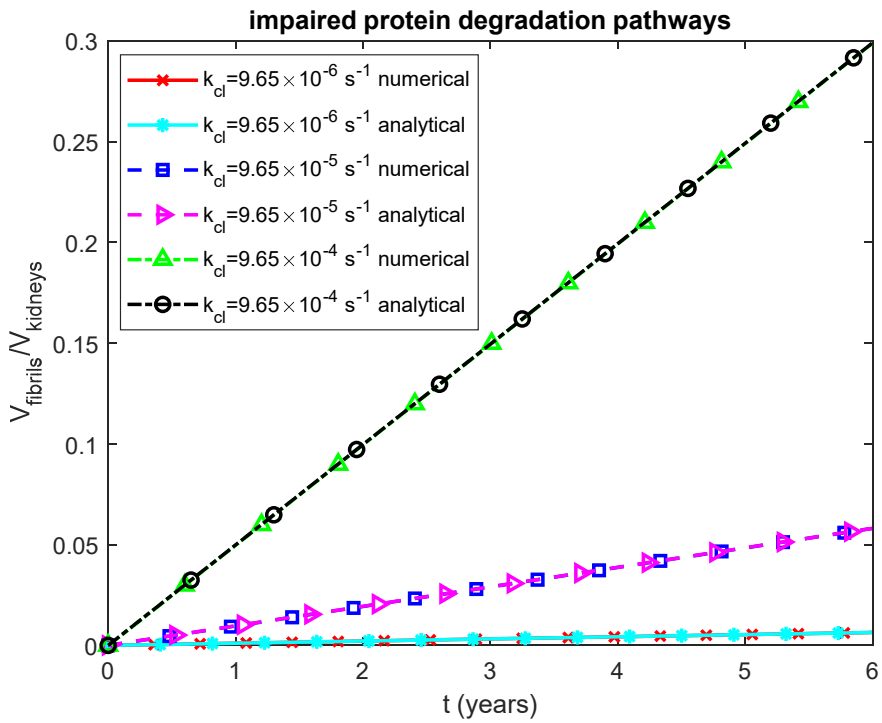

Fig. S12. Fraction of the baseline kidney volume occupied by fibrils as a function of time. (a) Biologically relevant half-lives $T_{1/2,A}$, $T_{1/2,B}$, $T_{1/2,I}$, and $T_{1/2,S}$, representing functional protein degradation machinery. (b) Infinite half-lives $T_{1/2,A}$, $T_{1/2,B}$, $T_{1/2,I}$, and $T_{1/2,S}$, representing complete impairment of protein degradation. Each panel shows results for three values of the rate constant for proteolytic cleavage of SAA that generates AA monomers. Baseline parameters: $k_1 = 10^{-4}$ s^{-1}, $k_2 = 10^{-4}$ μM^{-1} s^{-1}, $K_d = 1.1789$ μM, $h_S = 5.55 \times 10^{-7}$ m s^{-1}, $H_{tot} = 30$ μM, $S_{tot} = 8$ μM, and $\theta_{1/2,B} = 8.64 \times 10^4$ s; remaining parameters as listed in Table 2.

(a)

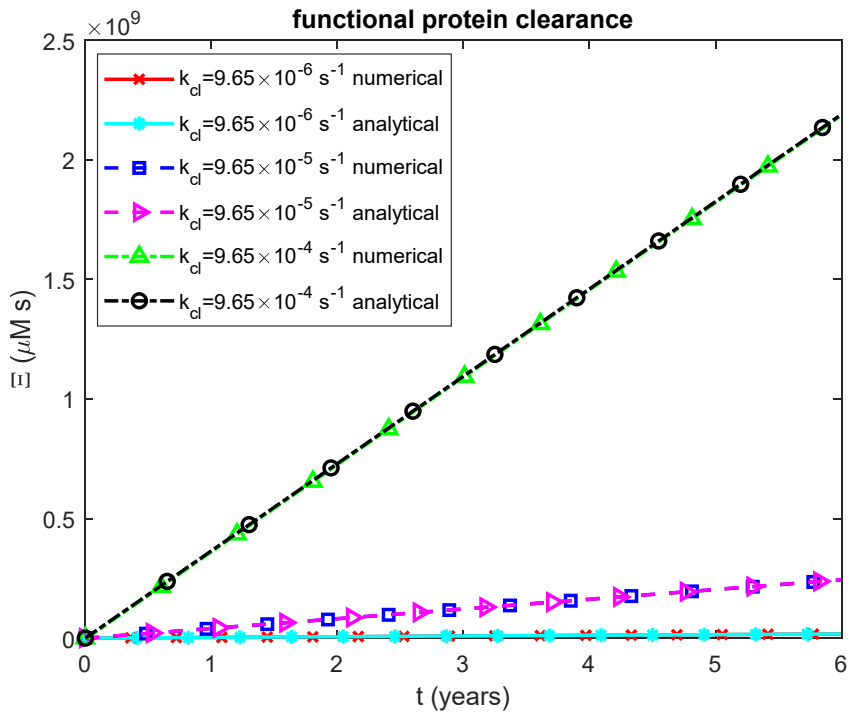

(b)

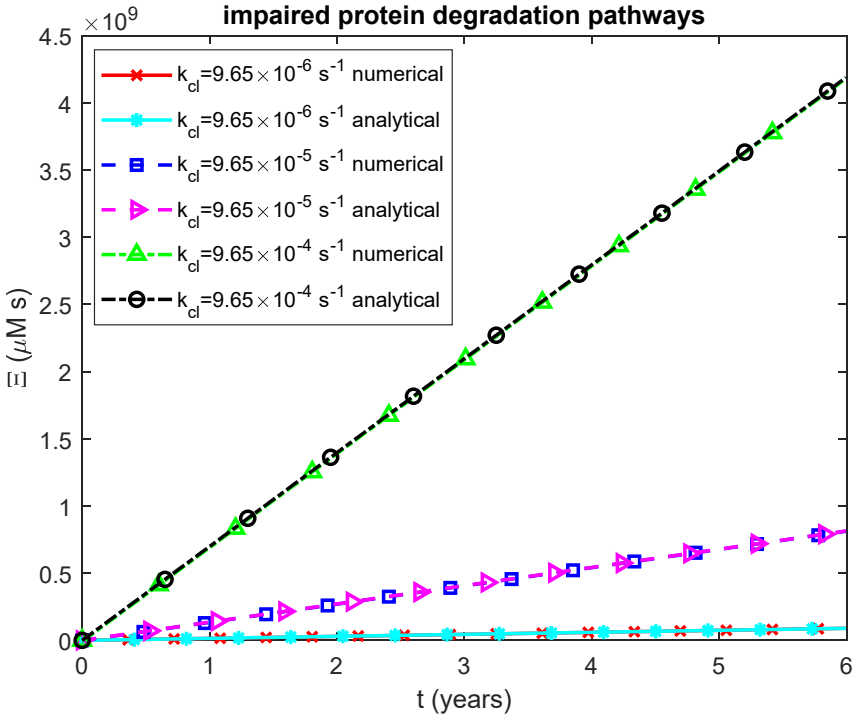

Fig. S13. Accumulated nephrotoxicity of AA oligomers as a function of time. (a) Biologically relevant half-lives $T_{1/2,A}$, $T_{1/2,B}$, $T_{1/2,I}$, and $T_{1/2,S}$, representing functional protein degradation machinery. (b) Infinite half-lives $T_{1/2,A}$, $T_{1/2,B}$, $T_{1/2,I}$, and $T_{1/2,S}$, representing complete impairment of protein degradation.

Each panel shows results for three values of the rate constant for proteolytic cleavage of SAA that generates AA monomers. Baseline parameters: $k_1 = 10^{-4}$ s^{-1}, $k_2 = 10^{-4}$ μM^{-1} s^{-1}, $K_d = 1.1789$ μM, $h_S = 5.55 \times 10^{-7}$ m s^{-1}, $H_{tot} = 30$ μM, $S_{tot} = 8$ μM, and $\theta_{1/2,B} = 8.64 \times 10^4$ s; remaining parameters as listed in Table 2.

(a)

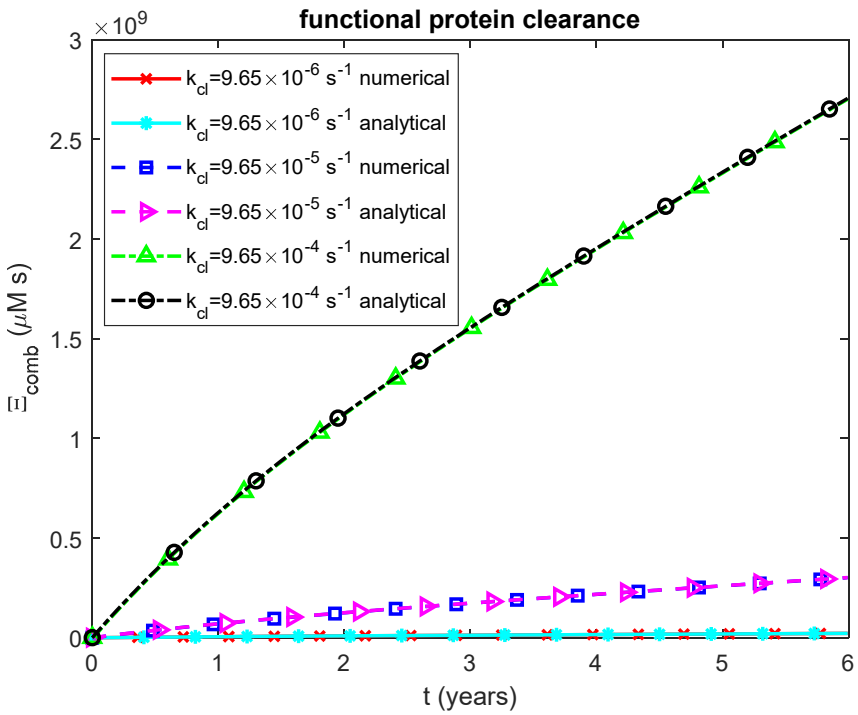

(b)

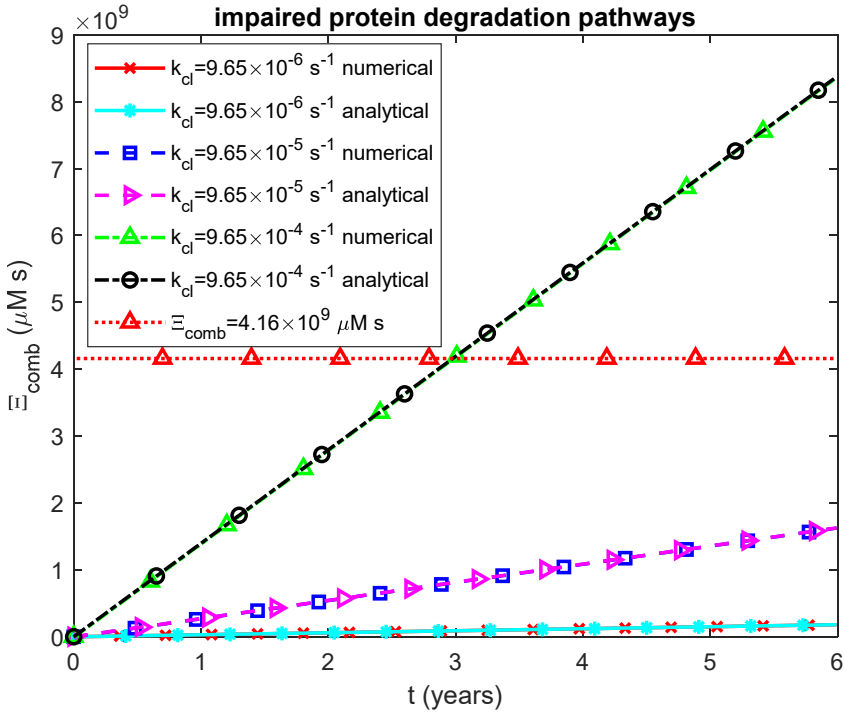

Fig. S14. Combined renal damage from accumulated AA oligomer cytotoxicity and insoluble fibril burden as a function of time. (a) Biologically relevant half-lives $T_{1/2,A}$, $T_{1/2,B}$, $T_{1/2,I}$, and $T_{1/2,S}$, representing functional protein degradation machinery. (b) Infinite half-lives $T_{1/2,A}$, $T_{1/2,B}$, $T_{1/2,I}$, and $T_{1/2,S}$, representing complete impairment of protein degradation. Each panel shows results for three values of the rate constant for proteolytic cleavage of SAA that generates AA monomers. Baseline parameters: $k_1 = 10^{-4}$ s^{-1}, $k_2 = 10^{-4}$ μM^{-1} s^{-1}, $K_d = 1.1789$ μM, $h_S = 5.55\times10^{-7}$ m s^{-1}, $H_{tot} = 30$ μM, $S_{tot} = 8$ μM, and $\theta_{1/2,B} = 8.64\times10^4$ s; remaining parameters as listed in Table 2.

(a)

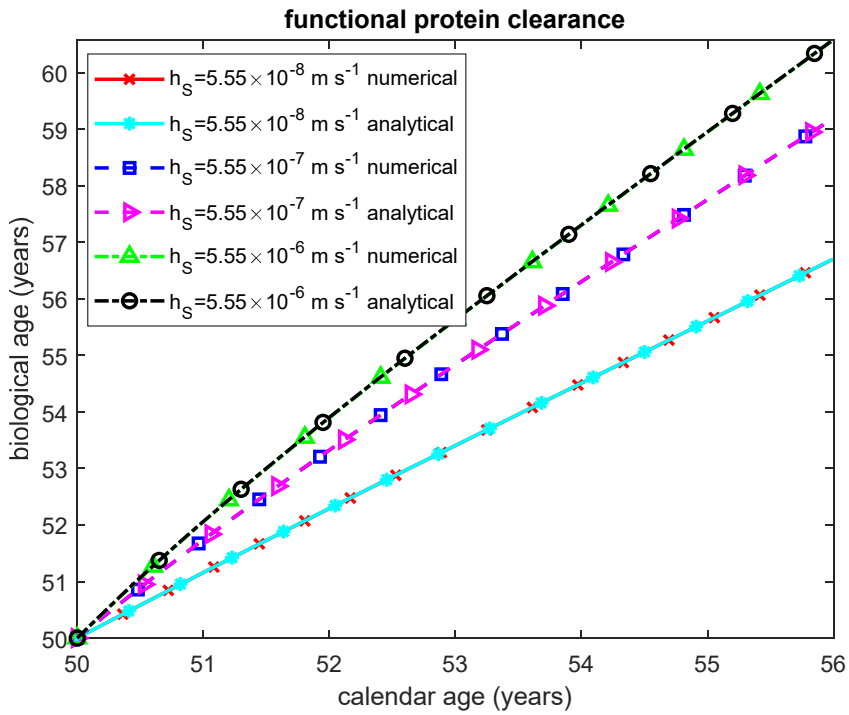

(b)

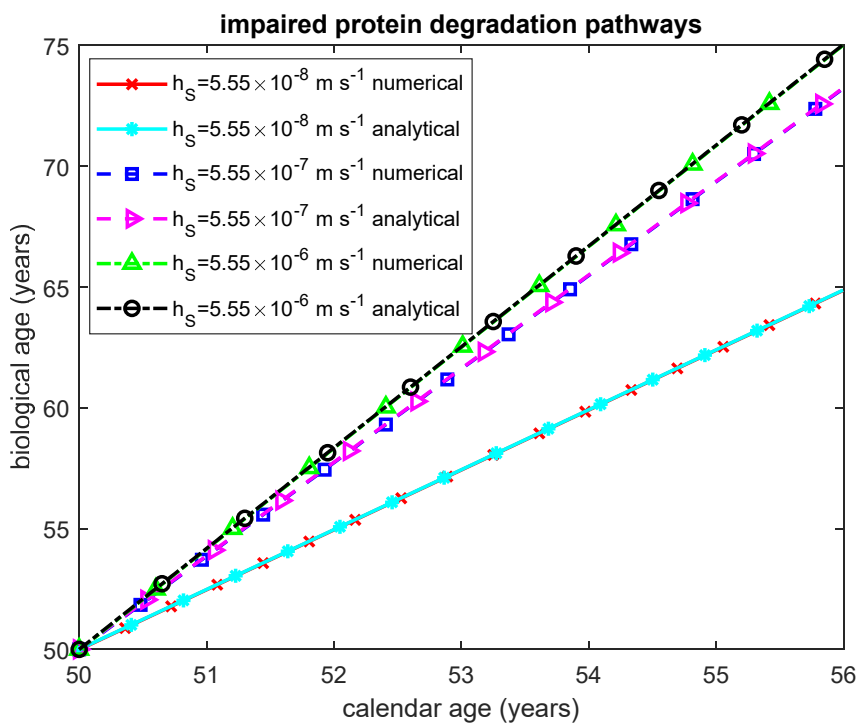

Fig. S15. Biological age of the kidney as a function of time. (a) Biologically relevant half-lives $T_{1/2,A}$, $T_{1/2,B}$, $T_{1/2,I}$, and $T_{1/2,S}$, representing functional protein degradation machinery. (b) Infinite half-lives $T_{1/2,A}$

, $T_{1/2,B}$, $T_{1/2,I}$, and $T_{1/2,S}$, representing complete impairment of protein degradation. Each panel shows results for three values of the mass transfer coefficient characterizing free SAA transport from blood plasma into the kidneys. Baseline parameters: $k_1 = 10^{-4}$ s^{-1}, $k_2 = 10^{-4}$ μM^{-1} s^{-1}, $k_{cl} = 9.65 \times 10^{-5}$ s^{-1}, $K_d = 1.1789$ μM, $H_{tot} = 30$ μM, $S_{tot} = 8$ μM, and $\theta_{1/2,B} = 8.64 \times 10^4$ s; remaining parameters as listed in Table 2.

(a)

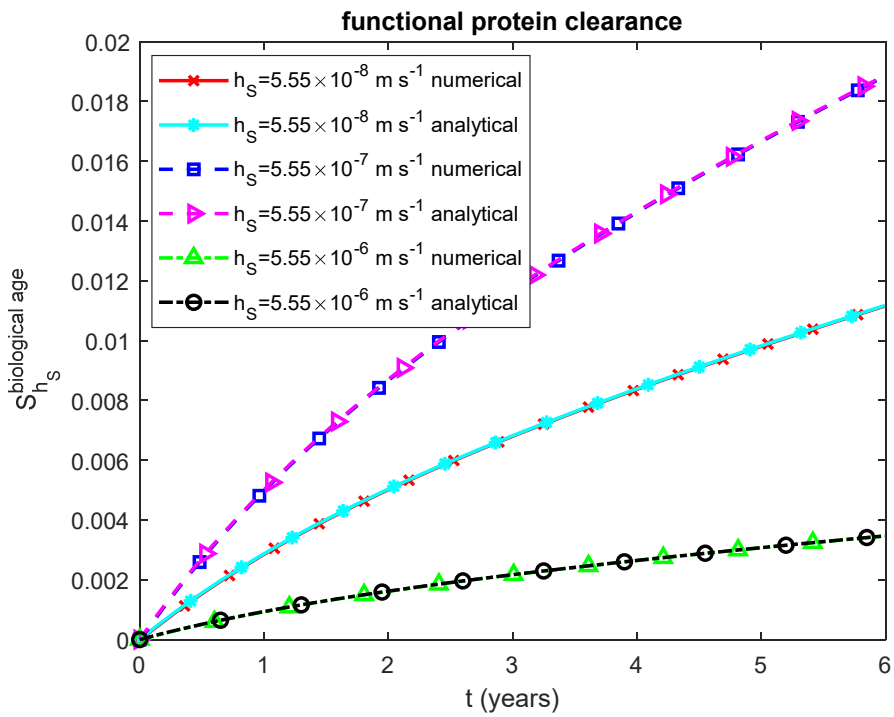

(b)

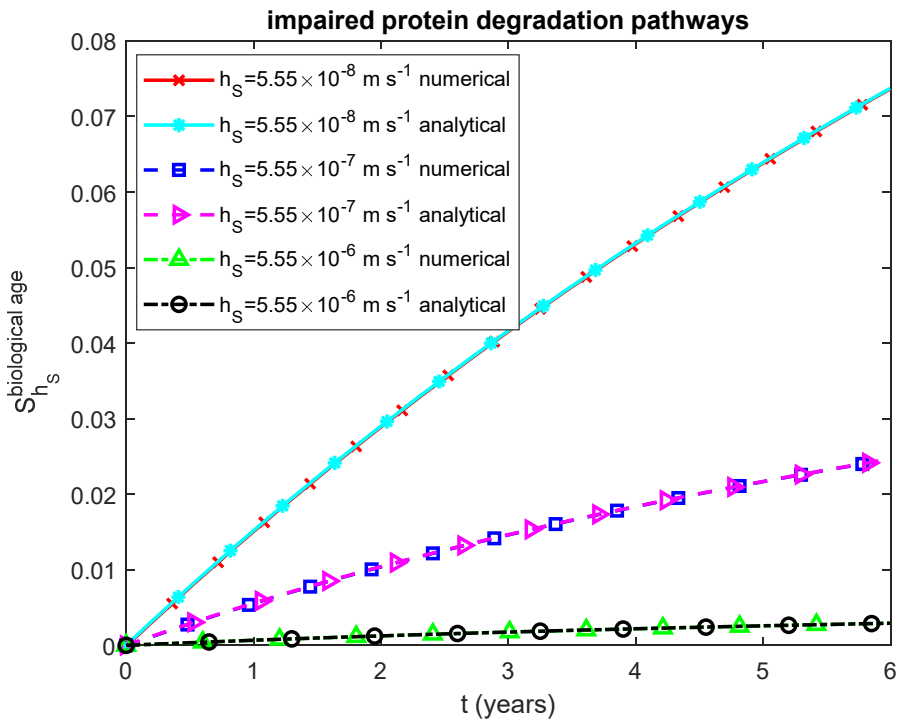

Fig. S16. Dimensionless sensitivity of renal biological age to the mass transfer coefficient for free SAA transport from blood plasma into the kidneys, as a function of time. (a) Biologically relevant half-lives $T_{1/2,A}$, $T_{1/2,B}$, $T_{1/2,I}$, and $T_{1/2,S}$, representing functional protein degradation machinery. (b) Infinite half-lives $T_{1/2,A}$, $T_{1/2,B}$, $T_{1/2,I}$, and $T_{1/2,S}$, representing complete impairment of protein degradation. Each panel shows results for three values of the mass transfer coefficient characterizing free SAA transport from blood plasma into the kidneys. Baseline parameters: $k_1 = 10^{-4}$ s^{-1}, $k_2 = 10^{-4}$ μM^{-1} s^{-1}, $k_{cl} = 9.65 \times 10^{-5}$ s^{-1}, $K_d = 1.1789$ μM, $H_{tot} = 30$ μM, $S_{tot} = 8$ μM, and $\theta_{1/2,B} = 8.64 \times 10^4$ s; remaining parameters as listed in Table 2.

(a)

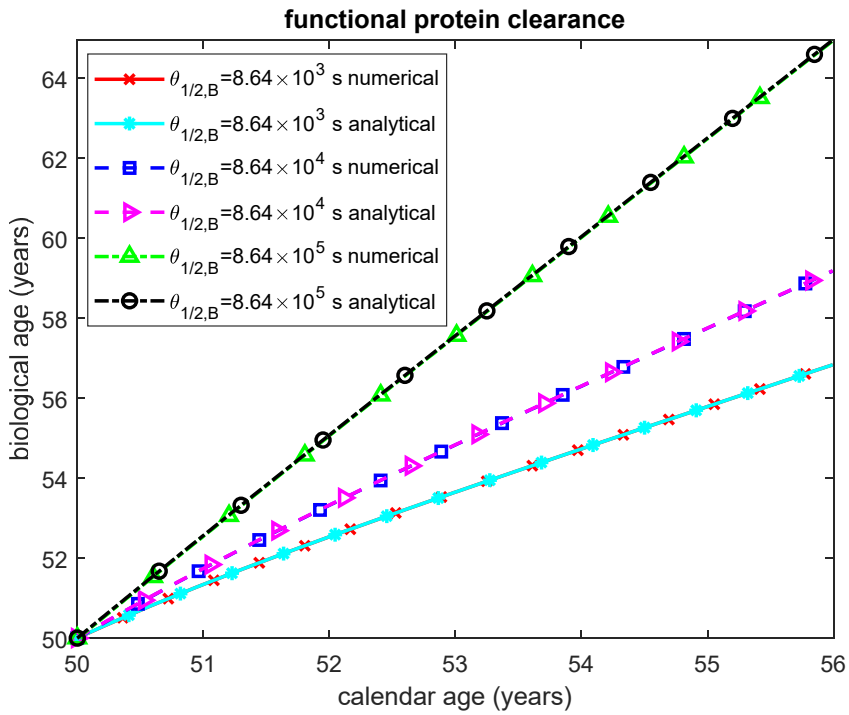

(b)

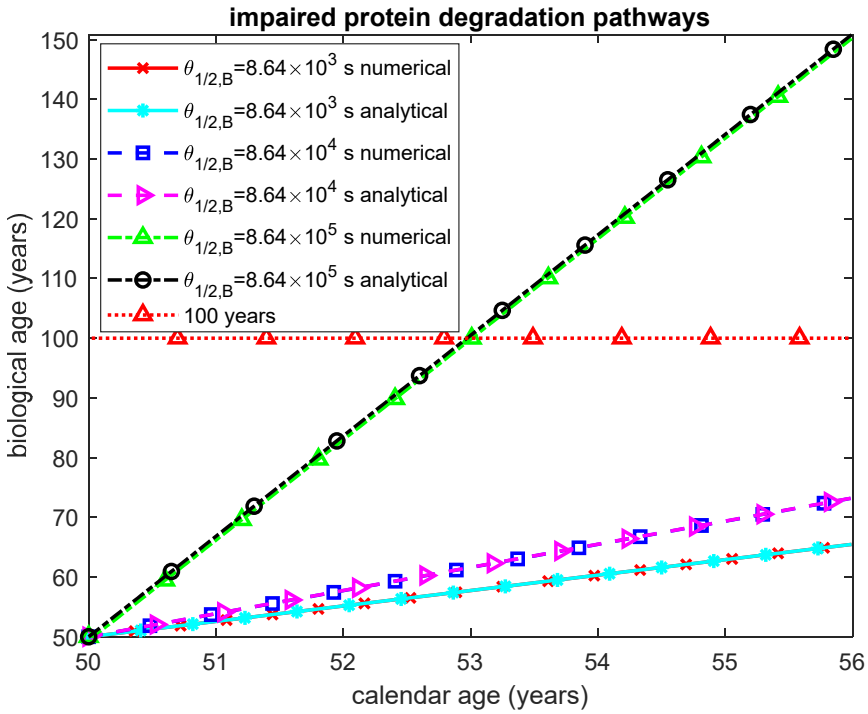

Fig. S17. Biological age of the kidney as a function of time. (a) Biologically relevant half-lives $T_{1/2,A}$, $T_{1/2,B}$, $T_{1/2,I}$, and $T_{1/2,S}$, representing functional protein degradation machinery. (b) Infinite half-lives $T_{1/2,A}$

, $T_{1/2,B}$, $T_{1/2,I}$, and $T_{1/2,S}$, representing complete impairment of protein degradation. Each panel shows results for three values of the half-deposition time characterizing the incorporation of free AA oligomers into fibrillar deposits. Baseline parameters: $k_1 = 10^{-4}$ s^{-1}, $k_2 = 10^{-4}$ μM^{-1} s^{-1}, $k_{cl} = 9.65 \times 10^{-5}$ s^{-1}, $K_d = 1.1789$ μM, $h_S = 5.55 \times 10^{-7}$ m s^{-1}, $H_{tot} = 30$ μM, and $S_{tot} = 8$ μM; remaining parameters as listed in Table 2.

(a)

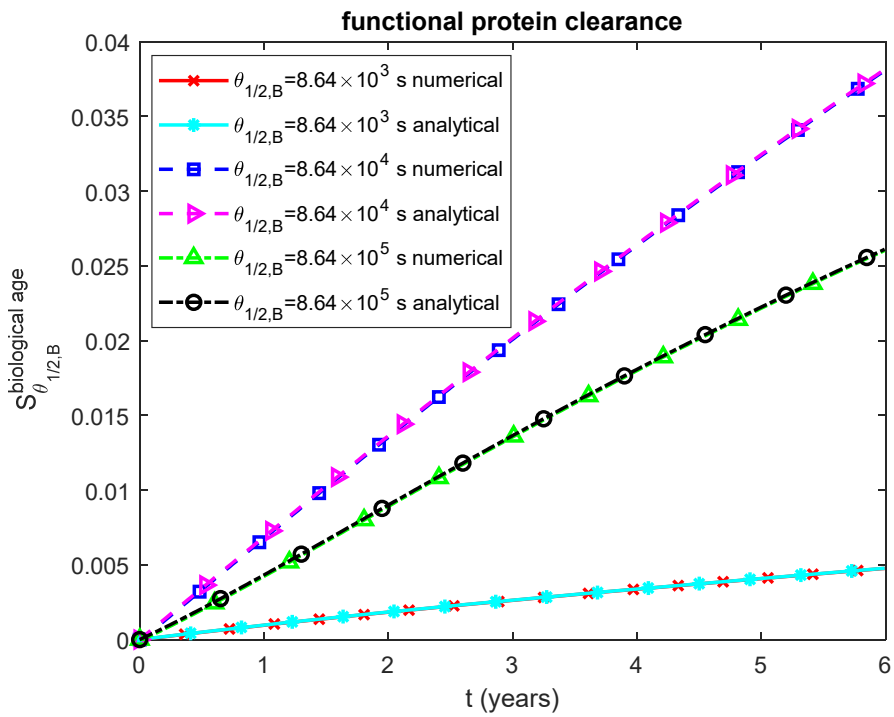

(b)

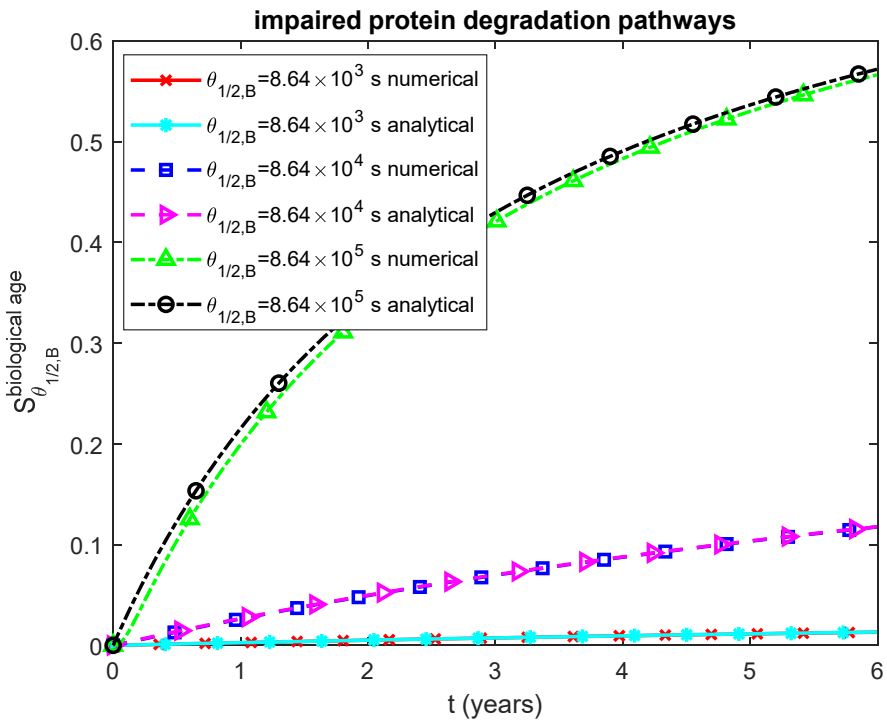

Fig. S18. Dimensionless sensitivity of renal biological age to the half-deposition time characterizing the incorporation of free AA oligomers into fibrillar deposits, as a function of time. (a) Biologically relevant half-lives $T_{1/2,A}$, $T_{1/2,B}$, $T_{1/2,I}$, and $T_{1/2,S}$, representing functional protein degradation machinery. (b) Infinite half-lives $T_{1/2,A}$, $T_{1/2,B}$, $T_{1/2,I}$, and $T_{1/2,S}$, representing complete impairment of protein degradation. Each panel shows results for three values of the half-deposition time characterizing the incorporation of free AA oligomers into fibrillar deposits. Baseline parameters: $k_1 = 10^{-4}$ s^{-1}, $k_2 = 10^{-4}$ μM^{-1} s^{-1}, $k_{cl} = 9.65\times10^{-5}$ s^{-1}, $K_d = 1.1789$ μM, $h_S = 5.55\times10^{-7}$ m s^{-1}, $H_{tot} = 30$ μM, and $S_{tot} = 8$ μM; remaining parameters as listed in Table 2.

(a)

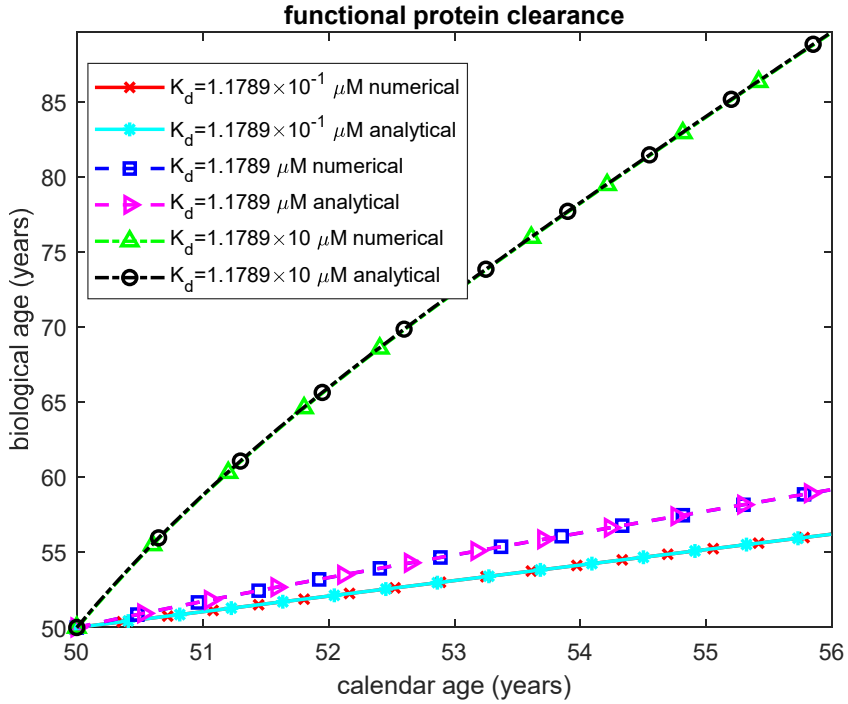

(b)

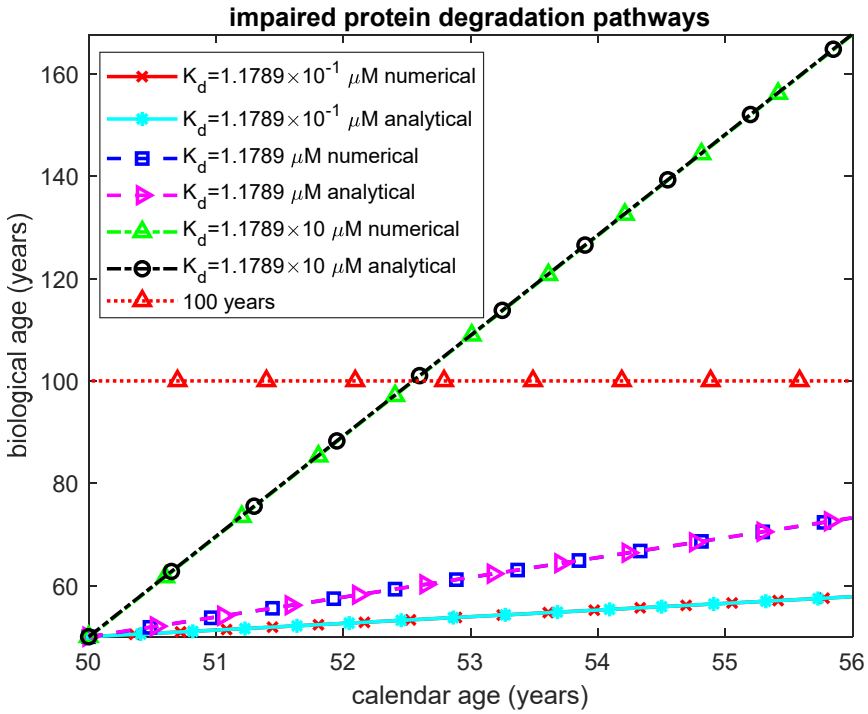

Fig. S19. Biological age of the kidney as a function of time. (a) Biologically relevant half-lives $T_{1/2,A}$, $T_{1/2,B}$, $T_{1/2,I}$, and $T_{1/2,S}$, representing functional protein degradation machinery. (b) Infinite half-lives $T_{1/2,A}$

, $T_{1/2,B}$, $T_{1/2,I}$, and $T_{1/2,S}$, representing complete impairment of protein degradation. Each panel shows results for three values of the equilibrium dissociation constant characterizing the affinity of SAA to HDL. Baseline parameters: $k_1 = 10^{-4}$ s^{-1}, $k_2 = 10^{-4}$ μM^{-1} s^{-1}, $k_{cl} = 9.65\times10^{-5}$ s^{-1}, $h_S = 5.55\times10^{-7}$ m s^{-1}, $H_{tot} = 30$ μM, $S_{tot} = 8$ μM, and $\theta_{1/2,B} = 8.64\times10^{4}$ s.; remaining parameters as listed in Table 2.

(a)

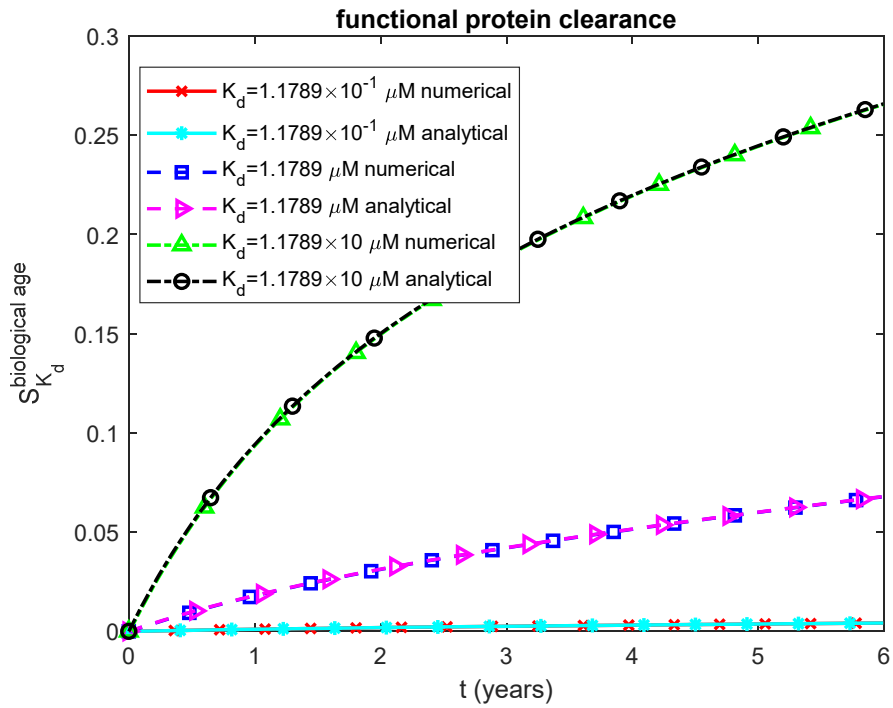

(b)

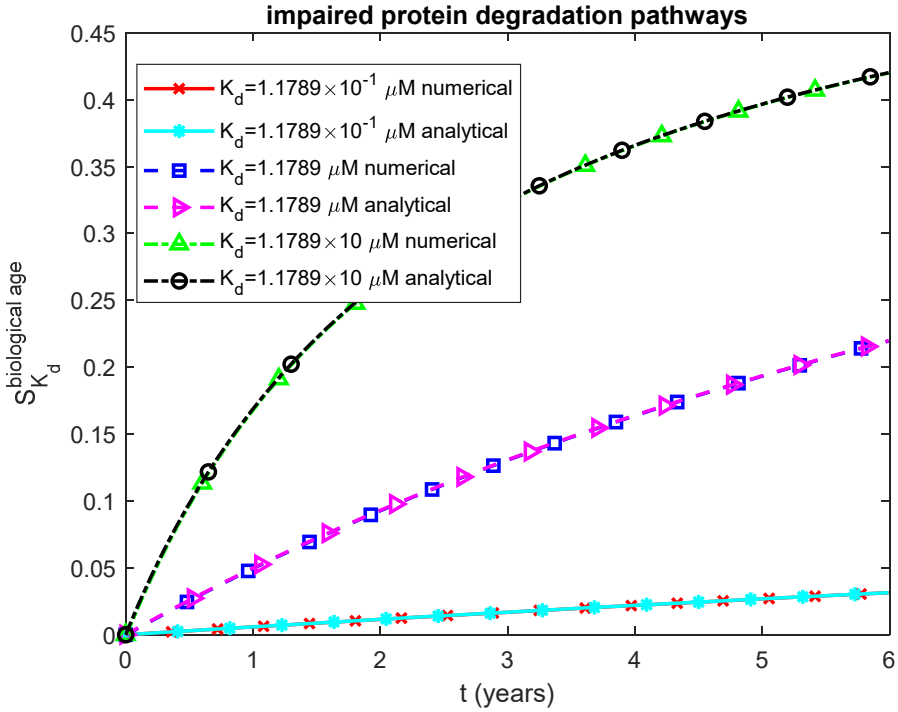

Fig. S20. Dimensionless sensitivity of renal biological age to the equilibrium dissociation constant characterizing the affinity of SAA to HDL, as a function of time. (a) Biologically relevant half-lives $T_{1/2,A}$, $T_{1/2,B}$, $T_{1/2,I}$, and $T_{1/2,S}$, representing functional protein degradation machinery. (b) Infinite half-lives $T_{1/2,A}$, $T_{1/2,B}$, $T_{1/2,I}$, and $T_{1/2,S}$, representing complete impairment of protein degradation. Each panel shows results for three values of the equilibrium dissociation constant characterizing the affinity of SAA to HDL. Baseline parameters: $k_1 = 10^{-4}$ s^{-1}, $k_2 = 10^{-4}$ μM^{-1} s^{-1}, $k_{cl} = 9.65\times10^{-5}$ s^{-1}, $h_S = 5.55\times10^{-7}$ m s^{-1}, $H_{tot} = 30$ μM, $S_{tot} = 8$ μM, and $\theta_{1/2,B} = 8.64\times10^{4}$ s; remaining parameters as listed in Table 2.

(a)

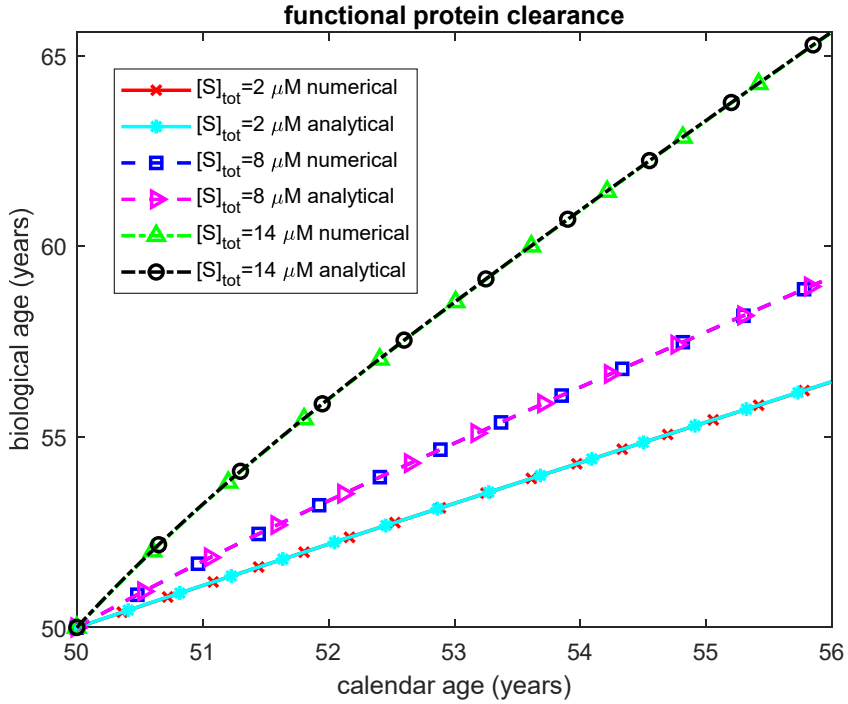

(b)

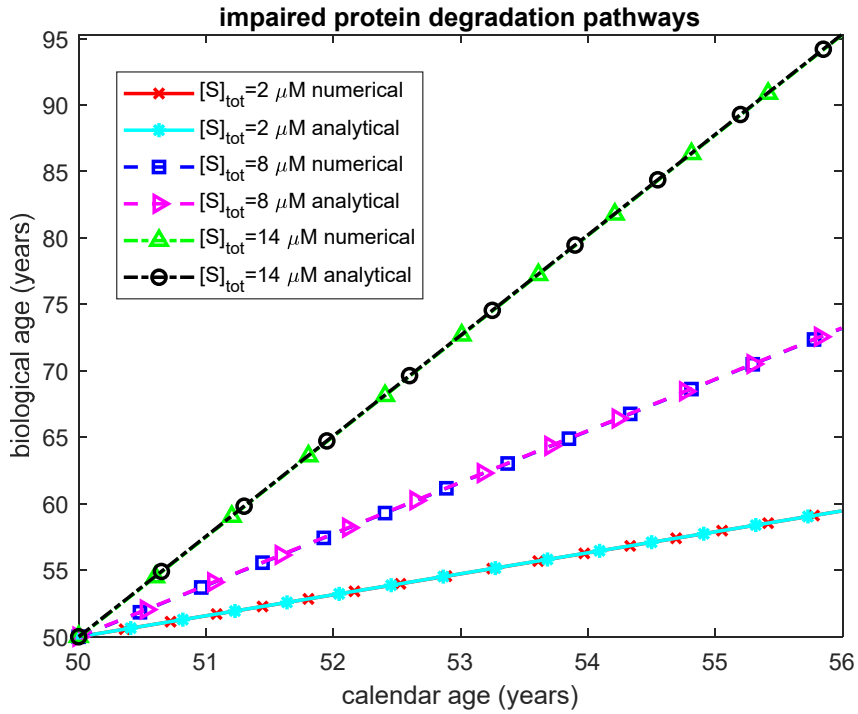

Fig. S21. Biological age of the kidney as a function of time. (a) Biologically relevant half-lives $T_{1/2,A}$, $T_{1/2,B}$, $T_{1/2,I}$, and $T_{1/2,S}$, representing functional protein degradation machinery. (b) Infinite half-lives $T_{1/2,A}$

, $T_{1/2,B}$, $T_{1/2,I}$, and $T_{1/2,S}$, representing complete impairment of protein degradation. Each panel shows results for three values of the molar concentration of total (HDL-bound and free) SAA under chronic inflammation. Baseline parameters: $k_1 = 10^{-4}$ s^{-1}, $k_2 = 10^{-4}$ μM^{-1} s^{-1}, $k_{cl} = 9.65\times10^{-5}$ s^{-1}, $K_d = 1.1789$ μM, $h_S = 5.55\times10^{-7}$ m s^{-1}, $H_{tot} = 30$ μM, and $\theta_{1/2,B} = 8.64\times10^{4}$ s; remaining parameters as listed in Table 2.

(a)

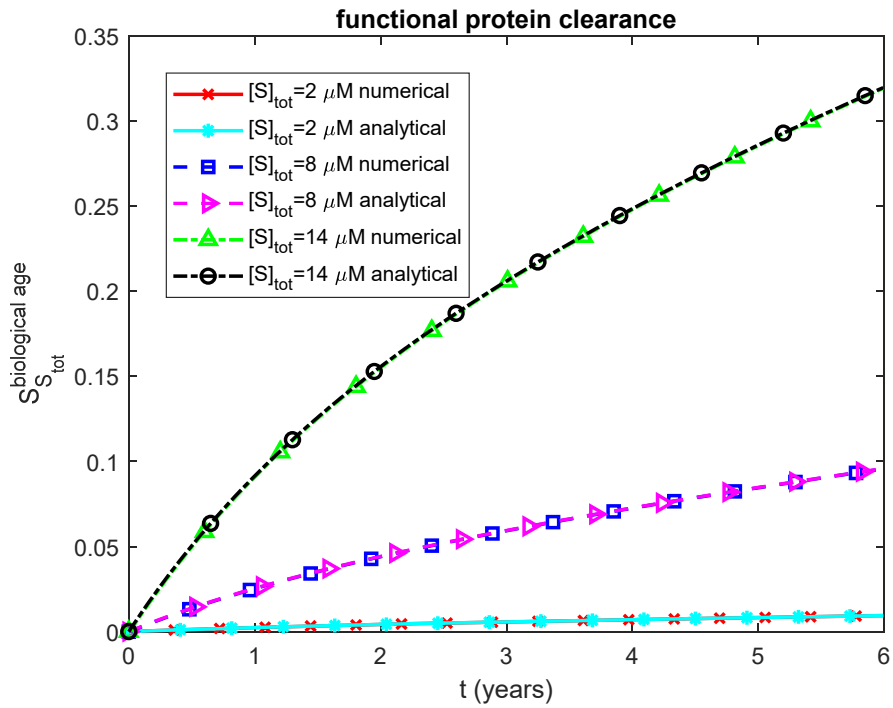

(b)

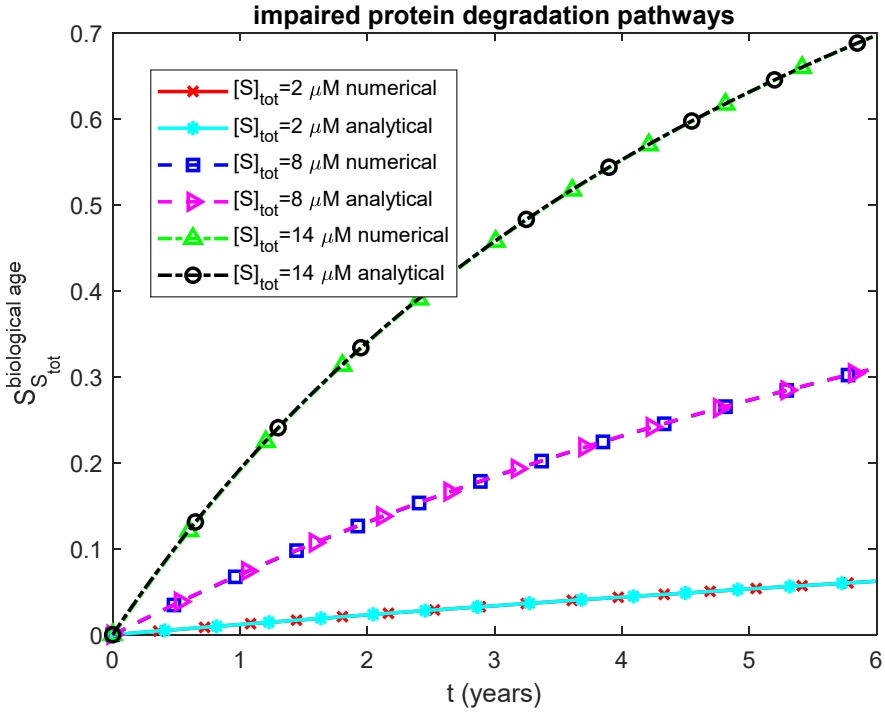

Fig. S22. Dimensionless sensitivity of renal biological age to the molar concentration of total (HDL-bound and free) SAA under chronic inflammation, as a function of time. (a) Biologically relevant half-lives $T_{1/2,A}$, $T_{1/2,B}$, $T_{1/2,I}$, and $T_{1/2,S}$, representing functional protein degradation machinery. (b) Infinite half-lives $T_{1/2,A}$, $T_{1/2,B}$, $T_{1/2,I}$, and $T_{1/2,S}$, representing complete impairment of protein degradation. Each panel shows results for three values of the molar concentration of total (HDL-bound and free) SAA under chronic inflammation. Baseline parameters: $k_1 = 10^{-4}$ s^{-1}, $k_2 = 10^{-4}$ μM^{-1} s^{-1}, $k_{cl} = 9.65\times10^{-5}$ s^{-1}, $K_d = 1.1789$ μM, $h_S = 5.55\times10^{-7}$ m s^{-1}, $H_{tot} = 30$ μM, and $\theta_{1/2,B} = 8.64\times10^{4}$ s; remaining parameters as listed in Table 2.

(a)

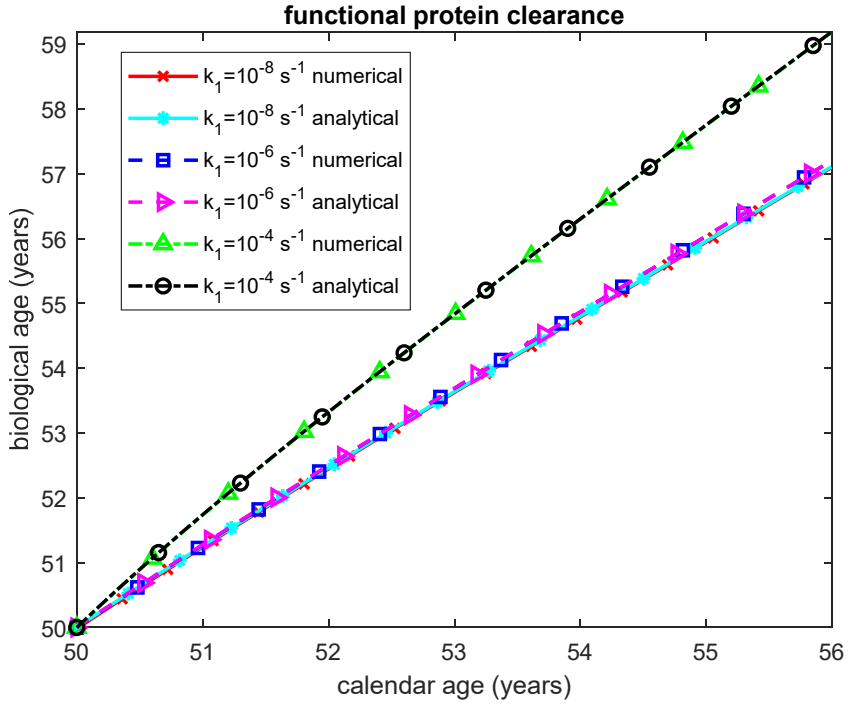

(b)

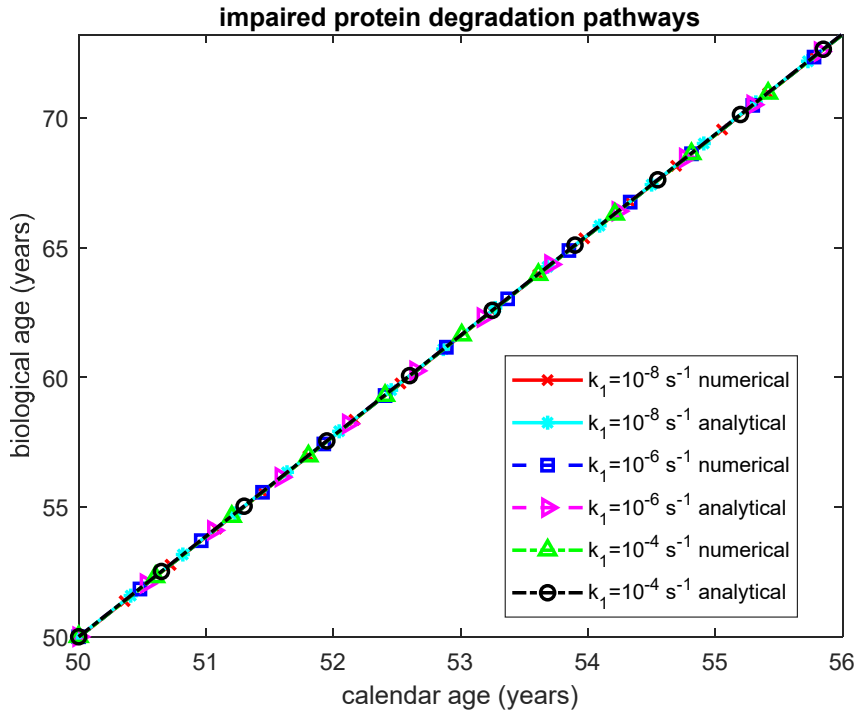

Fig. S23. Biological age of the kidney as a function of time. (a) Biologically relevant half-lives $T_{1/2,A}$, $T_{1/2,B}$, $T_{1/2,I}$, and $T_{1/2,S}$, representing functional protein degradation machinery. (b) Infinite half-lives $T_{1/2,A}$

, $T_{1/2,B}$, $T_{1/2,I}$, and $T_{1/2,S}$, representing complete impairment of protein degradation. Each panel shows results for three values of the rate constant describing the first pseudoelementary (nucleation) step in the F-W model of AA oligomer formation. Baseline parameters: $k_2 = 10^{-4}$ μM^{-1} s^{-1}, $k_{cl} = 9.65\times10^{-5}$ s^{-1}, $K_d = 1.1789$ μM, $h_S = 5.55\times10^{-7}$ m s^{-1}, $H_{tot} = 30$ μM, $S_{tot} = 8$ μM, and $\theta_{1/2,B} = 8.64\times10^{4}$ s; remaining parameters as listed in Table 2.

(a)

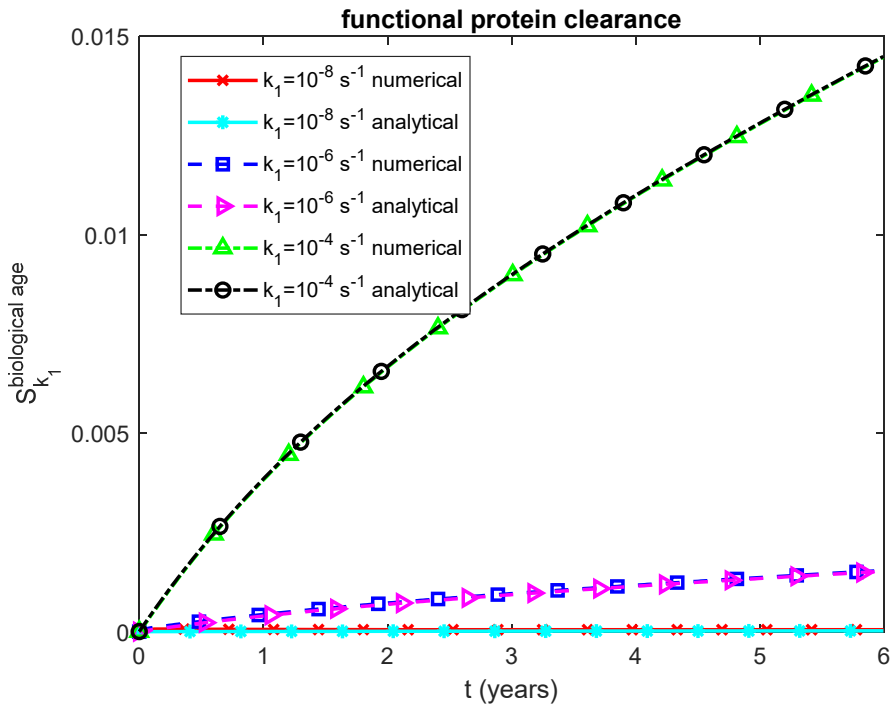

(b)

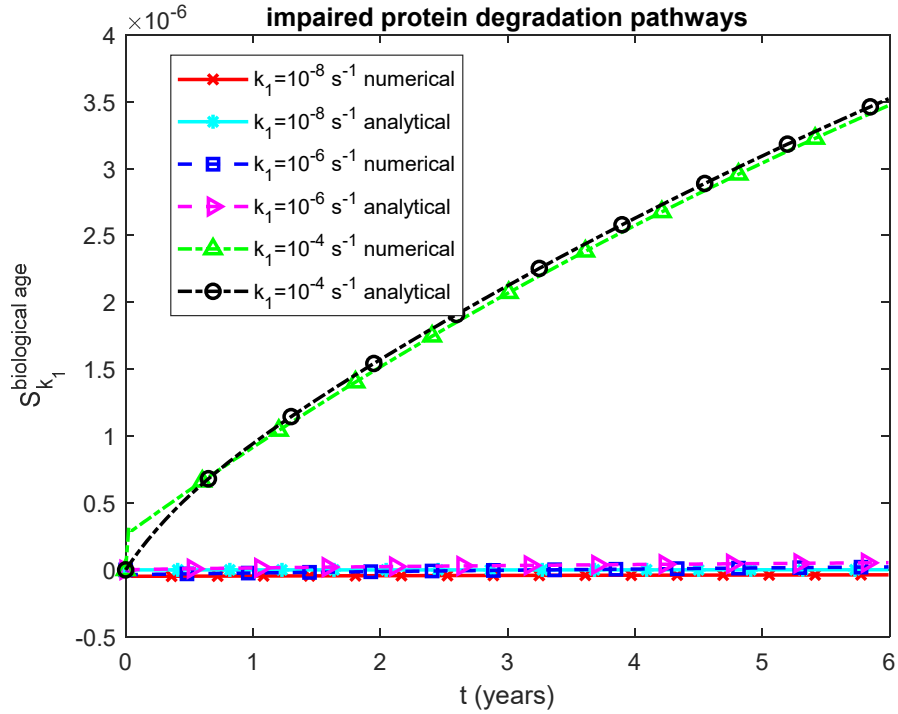

Fig. S24. Dimensionless sensitivity of renal biological age to the rate constant describing the first pseudoelementary (nucleation) step in the F-W model of AA oligomer formation, as a function of time. (a) Biologically relevant half-lives $T_{1/2,A}$, $T_{1/2,B}$, $T_{1/2,I}$, and $T_{1/2,S}$, representing functional protein degradation machinery. (b) Infinite half-lives $T_{1/2,A}$, $T_{1/2,B}$, $T_{1/2,I}$, and $T_{1/2,S}$, representing complete impairment of protein degradation. Each panel shows results for three values of the rate constant describing the first pseudoelementary (nucleation) step in the F-W model of AA oligomer formation. Baseline parameters: $k_2 = 10^{-4}$ μM^{-1} s^{-1}, $k_{cl} = 9.65\times10^{-5}$ s^{-1}, $K_d = 1.1789$ μM, $h_S = 5.55\times10^{-7}$ m s^{-1}, $H_{tot} = 30$ μM, $S_{tot} = 8$ μM, and $\theta_{1/2,B} = 8.64\times10^4$ s; remaining parameters as listed in Table 2.

(a)

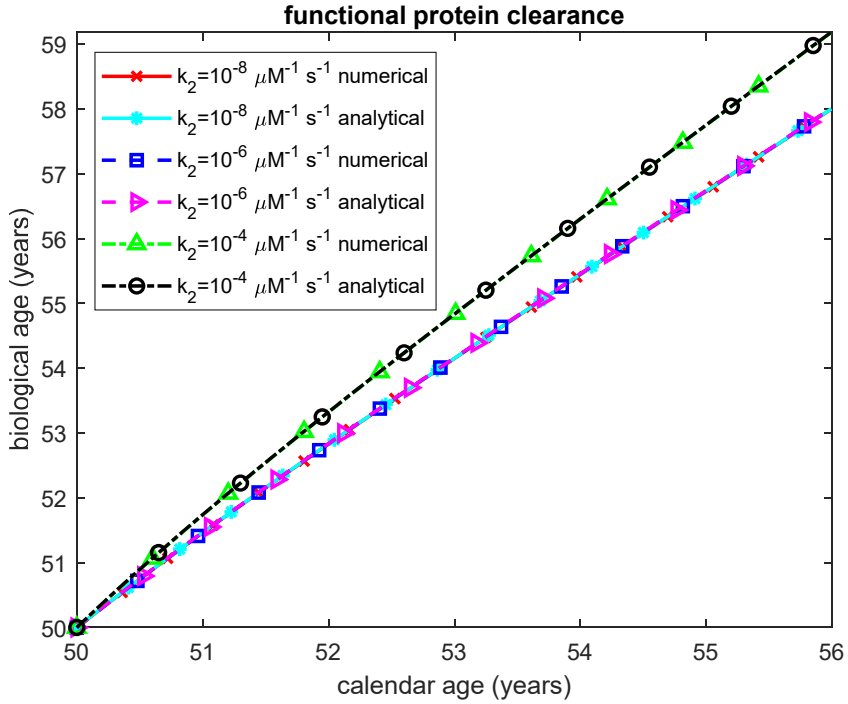

(b)

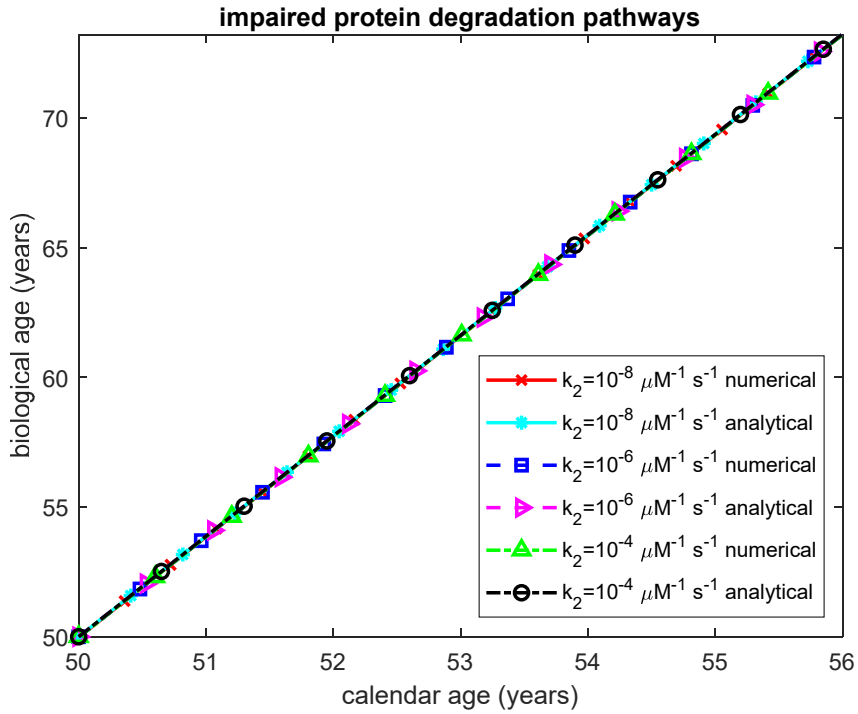

Fig. S25. Biological age of the kidney as a function of time. (a) Biologically relevant half-lives $T_{1/2,A}$, $T_{1/2,B}$, $T_{1/2,I}$, and $T_{1/2,S}$, representing functional protein degradation machinery. (b) Infinite half-lives $T_{1/2,A}$

, $T_{1/2,B}$, $T_{1/2,I}$, and $T_{1/2,S}$, representing complete impairment of protein degradation. Each panel shows results for three values of the rate constant describing the second pseudoelementary (autocatalytic growth) step in the F-W model of AA oligomer formation. Baseline parameters: $k_1 = 10^{-4}$ s^{-1}, $k_{cl} = 9.65 \times 10^{-5}$ s^{-1}, $K_d = 1.1789$ μM, $h_S = 5.55 \times 10^{-7}$ m s^{-1}, $H_{tot} = 30$ μM, $S_{tot} = 8$ μM, and $\theta_{1/2,B} = 8.64 \times 10^4$ s, and $\theta_{1/2,B} = 8.64 \times 10^4$ s; remaining parameters as listed in Table 2.

(a)

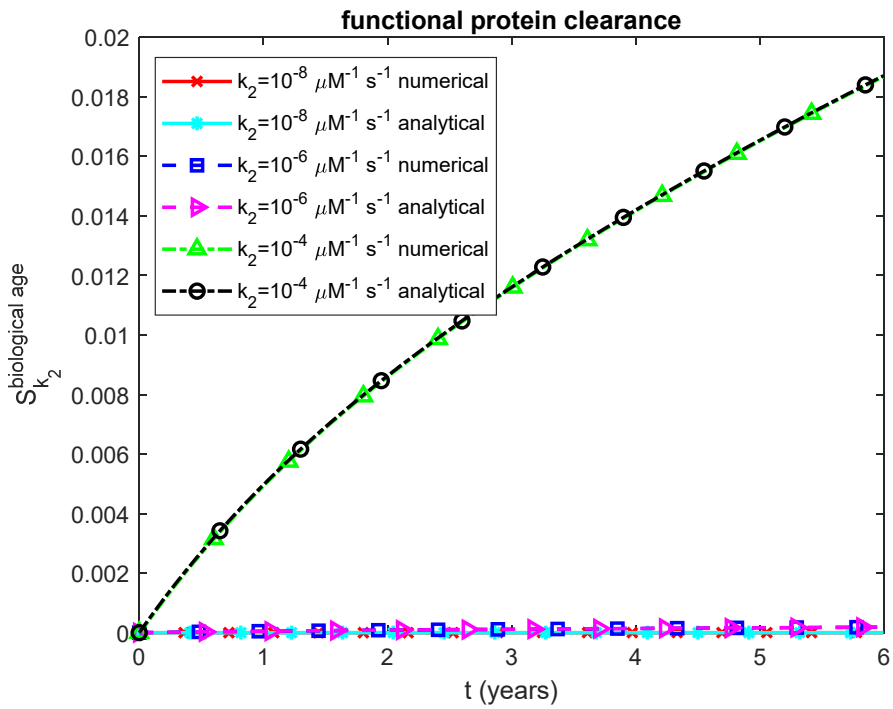

(b)

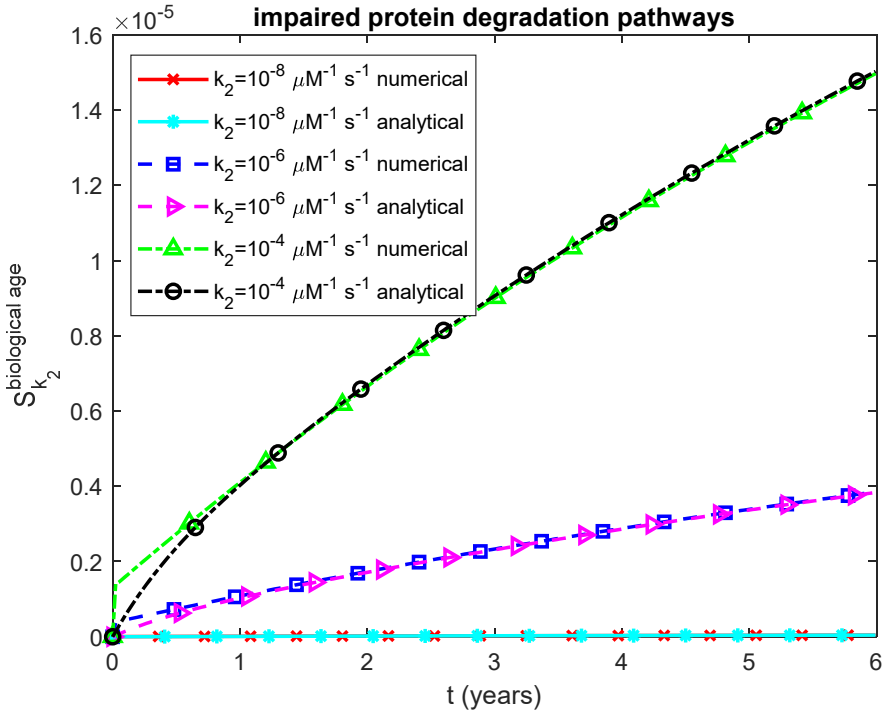

Fig. S26. Dimensionless sensitivity of renal biological age to the rate constant describing the second pseudoelementary (autocatalytic growth) step in the F-W model of AA oligomer formation. (a) Biologically relevant half-lives $T_{1/2,A}$, $T_{1/2,B}$, $T_{1/2,I}$, and $T_{1/2,S}$, representing functional protein degradation machinery. (b) Infinite half-lives $T_{1/2,A}$, $T_{1/2,B}$, $T_{1/2,I}$, and $T_{1/2,S}$, representing complete impairment of protein degradation. Each panel shows results for three values of the rate constant describing the second pseudoelementary (autocatalytic growth) step in the F-W model of AA oligomer formation. Baseline parameters: $k_1 = 10^{-4}$ s^{-1}, $k_{cl} = 9.65 \times 10^{-5}$ s^{-1}, $K_d = 1.1789$ μM, $h_S = 5.55 \times 10^{-7}$ m s^{-1}, $H_{tot} = 30$ μM, $S_{tot} = 8$ μM, and $\theta_{1/2,B} = 8.64 \times 10^4$ s, and $\theta_{1/2,B} = 8.64 \times 10^4$ s; remaining parameters as listed in Table 2.